Civil and Infrastructure Engineering

8 papers

Seismic Response of Long Continuous Prestressed Bridge Subjected to Multiple Support Excitations

Harendra Chaudhary [1]

[1]Structural Engineer
[1]Civil Department, Institute of Engineering, Pulchowk Campus, TU

ABSTRACT

In this research, multi-point excitation of prestressed bridge is determined by using Time History Analysis (Modal Time History and Direct Integration).In the prestressed bridge, the earthquake wave passage effect is considered as the time lag between two supports of the bridge. The soil-structure interactions and incoherence effects are discarded but the standard Shear Wave Velocity is used for soft soil. One of conclusion of research is, if the velocity of travelling wave is increased then the differential displacement of pier comparing with uniform excitations is in decreasing order. Finally, if the wave velocity becomes infinity then the lag between supports becomes negligible and the response of structure does not change as compared to uniform excitation.

KEYWORDS: Continuous rigid-framed bridge, multi-support excitations, seismic response analysis

I.NTRODUCTION

Bridge is life line of road network, both in urban and rural areas. A bridge is a structure provided in railway, highway, and footway and service way over intersection of roads, rivers, streams, lakes etc for smooth crossing of trains, vehicles, people and utility services. With rapid technology growth the conventional bridge has been replaced by innovative cost effective structural system. One of these solution present prestressed I Girder Bridge. Prestressed concrete is ideally suited for the construction of medium and long span bridges. Ever since the development of prestressed concrete by Freyssinet in the early 1930s, the material has found extensive application in the construction of long-span bridges, gradually replacing steel which needs costly maintenance due to the inherent disadvantage of corrosion under aggressive environment conditions. One of the most commonly used forms of superstructure in concrete bridges is precast girders with cast-in-situ slab. In calculation of the dynamic response about these long-span bridges, the assumptions of uniform ground excitation cannot be considered valid. For large-span bridges, many of the researchers have studied multi-support and travelling seismic wave effects. For the bridges spanning up to 105m multi-point excitation does not give significant results. If the span length is greater than 105m then multi-point excitation should be done in order to determine the exact response of the bridge. The bridges structures are also susceptible to damage from lateral loading caused by large magnitude of earthquake.

2. DESCRIPTION OF THE BRIDGE MODELS

The bridge used in this study is Maraha Khola Bridge, located at Mahottari district. It is a prestressed concrete, two lane bridge with carriageway width 7.50 m with 1.50m footpath on both sides. It consists of five spans continuous supported over pier cap. The superstructure consists of four longitudinal I-girders of cross section with dimension 500mm x 1800mm at spanning over each of five spans. The cross section of cross girders is 200mm x 1250mm. Deck

slab of thickness 250mm at supports are constructed monolithically with the longitudinal girders and cross girders.

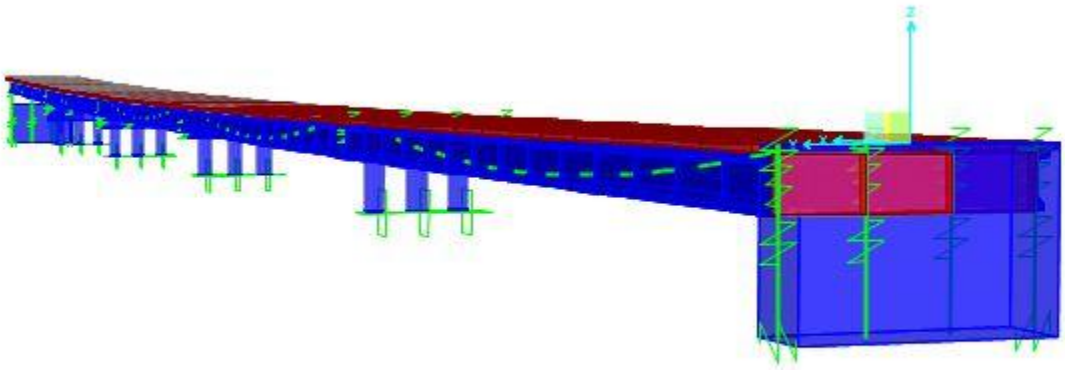


Figure 1: 3D view of Continuous Prestressed Bridge Model by CSI Bridge 2016

3. ANALYSIS METHOD OF MULTIPLE EXCITATIONS

Time-history analysis is a step-by-step analysis of the dynamical response of a structure to a specified loading that may vary with time (CSI, 2005).The time-history analysis is used to determine the dynamic response of a structure to arbitrary loading. All real physical structures behave dynamically when subjected to load or displacement (Wilson, 2002). If the loads or displacements are applied very slowly, the inertia forces can be neglected, and static load analysis can be justified and otherwise dynamic analysis of structure is needed. In elastic time history dynamic analyses are used to find the seismic response of the bridge due to earthquake ground motions. The wave passage effect in the time history analysis is considered as the time lag of the arrival time of the wave from one support to another support. The time history records used for this analysis are in the acceleration values at even time intervals of 0.05sec.Preliminarily the time history analysis of the structure is done using both sine and cosine function which have π/2 phase shift. Time history analysis is done for peak ground acceleration upto 1.5g.

The dynamic equilibrium equation is second order differential equation as given by

(1)

For seismic loading, the external basic seismic motions are the three components of free field ground accelerations that are known at the surface where foundation laid.

(2)

Numerical evaluation of the dynamic response of systems responding beyond their linearly elastic range is computationally demanding (Chopra, 2007).The only generally applicable procedure for analysis of an arbitrary set of nonlinear response equation is by step-by-step numerical integration (Clough and Penzien, 1991). The most general approach to solving the dynamic response of structural systems is the direct numerical integration of dynamic equilibrium equation (Wilson, 2002). Direct numerical integration aims to calculate the value of X and its derivatives at discrete intervals of time, Δt. Time history analysis is a step by step analysis of the dynamic response of a structure to a specified loading that may vary with time.

The Hilber, Hughes, and Taylor α method that uses the single parameter α and may take the value 0 to -1/3 (Wilson, 2002) is used for solving the equation of motion.

(3)

Time history dynamic analyses are used to find the seismic response of bridge pier due to earthquake ground motions. These time history ground motions are in the form of acceleration values at equal time interval of 0.05sec.

5. SEISMIC RESPONSES ANALYSIS OF BRIDGE

The dynamic response of long continuous rigid-framed bridge is calculated. There are comparison of uniform seismic excitation and multiple support excitations analysis.

5.1 Traveling Wave Effect

The seismic input considering travelling wave effect is applied in time history analysis. The time lag between different support points when the seismic wave arrives is determined by pseudo wave velocity and the angle θ between the seismic wave propagation direction and the structure longitudinal axis. In the analysis, θ is assumed as zero.

For multiple support excitations, time lags between different supports are to be calculated. The following procedure to estimate the time lag is proposed.

Velocity of P wave, Vp =

Where, λ=

E=

For silty sand: υ=0.3, E=20,000 KN/m^2

Substituting the values in equation, we get,

λ= = 11538.46 KN/m^2

= 7692.3 KN/m^2

Vp = =

Vp = 38.67 m/s

Time lag estimated between two consecutive supports of model is 1.034 sec for that velocity .For different velocity ranges from 100m/s to 200m/s, time lag is calculated and thus generated new time history function are applied in structures.

6. RESULTS AND DISCUSSION

6.1 Moving Load Analysis

The moving load analysis of continuous bridge is done both shear force and bending moment along the span of bridge. The shear force and bending moment along the span of bridge under different loadings is considered and it will be helpful to calculate the shear force and bending

moment for span of bridge. The negative moment developed in Continuos Bridge at intermediate support requires larger section than at mid span.

6.2 Time History Analysis

Time history analysis is carried out as methodology described in this chapter .The seismic input is in the form of ground motion time history at the surface of earth. Time history consists of peak 0.5g and duration of 29.75sec, entire time history record shown in figure. Time history is rescaled from 0.1g to 1.5g in an increment of 0.1g, generating 15 numbers of time histories with varying peak ground acceleration for uniform excitation. Rescaled time histories are considered independent of each other; provide weak to strong level of shaking simulation of ground motion of different return period at bridge location. Different time history records are prepared for different pier considering phase lag that is applied as time shift. The top displacement of pier and member forces in the pier is of prime importance of such bridge model. All these generated time histories are applied in longitudinal direction of the bridge axis. The pier top displacements are recorded for uniform excitation and multiple excitations (wave passage effect).Preliminarily the Time history analysis considering the phase shift sine and cosine function and the pier top displacement is observed which shows the variation of response of structure under phase lag function. The time history analysis considering traveling wave effect and uniform excitation is done using Gorkha earthquake records. The displacement under uniform excitation and multiple excitations are discussed.

6.3. Discussions

Table 0-1 MODAL Time period and frequency

Mode	Time Period(sec)	Frequency(cyc/sec)	Circular Frequency(rad/sec)
1	0.22884	4.36987	27.44275
2	0.2151	4.64900	29.19572
3	0.20602	4.85390	30.48248
4	0.19668	5.08440	31.93004
5	0.19495	5.12952	32.21339
6	0.18671	5.35590	33.63505
7	0.11277	8.86761	55.68857
8	0.09613	10.40258	65.32820
9	0.07945	12.58653	79.04342
10	0.06649	15.03986	94.45029
11	0.03802	26.30195	165.17622
12	0.01985	50.37783	316.37280

Table 0-2 Pier top displacement for PGA 0.5g using time history analysis

Case	Pier No	Displacement at pier top(mm)
Uniform Excitation	All Piers	48.943
Multiple Excitation considering traveling wave effect for velocity of 38.67 m/s	1	40.525
	2	38.065
	3	37.06
	4	35.513

Table 0-3 Pier top displacement at PGA 0.5g for velocity of 100 m/s

Point	Displacement at pier top(mm)
Pier 1	46.752
Pier 2	45.695
Pier 3	44.750

Pier 4	42.956

Table 0-4 Pier top displacement at PGA 0.5g for velocity of 200 m/s

Point	Displacement at pier top(mm)
Pier 1	46.963
Pier 2	46.360
Pier 3	45.369
Pier 4	44.820

In different wave velocities, pier top displacements are different. It is highest in first pier and decreases in slowly in the further pier which is shown in Figure 1-3. Pier top displacement increases when wave velocity increases which can be seen in Figures 1, Figure 2 and Figure 3 where wave velocity are 38.67m/s, 100 m/s and 200 m/s respectively on soft soil at PGA 0.5g. All these three graphs are combined in one which is shown in Figure 4. It this graph it is seen that changes of pier top displacement in different piers is decreases in increasing of wave velocities. Percentage change in top displacement is decreasing in increasing of wave velocity which is shown in Figure 5.

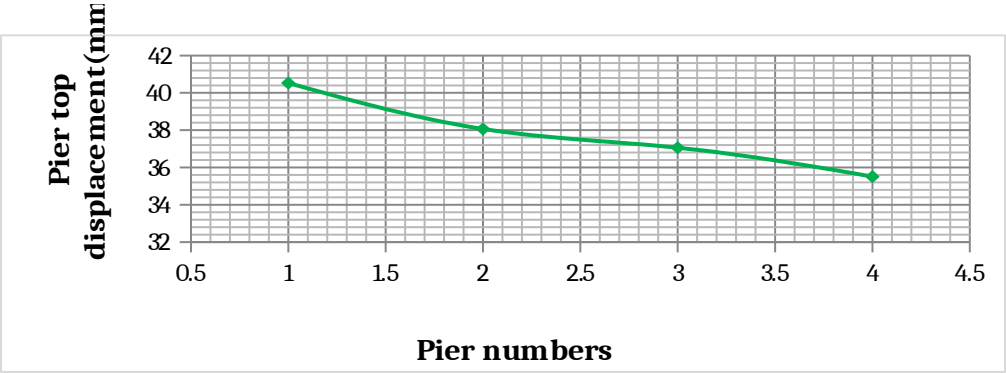


Figure 1: Pier top displacement at wave velocity 38.67m/s on soft soil at PGA 0.5g

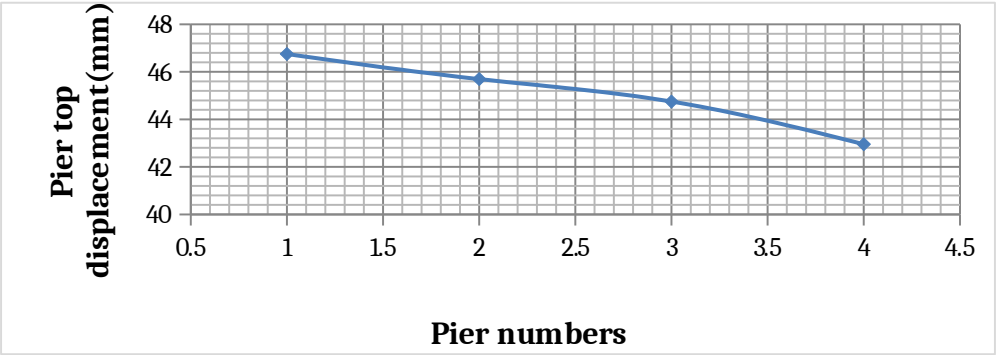


Figure 2: Pier top displacement at velocity 100 m/s on soft soil at PGA 0.5g

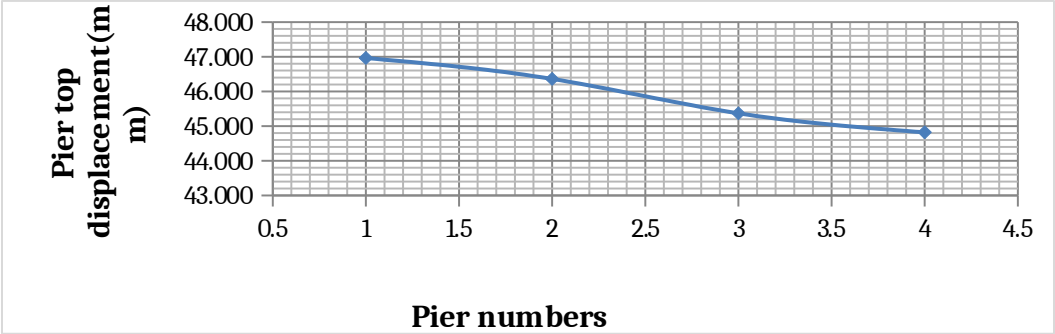


Figure 3: Pier top displacement at velocity 200 m/s on soft soil at PGA 0.5g

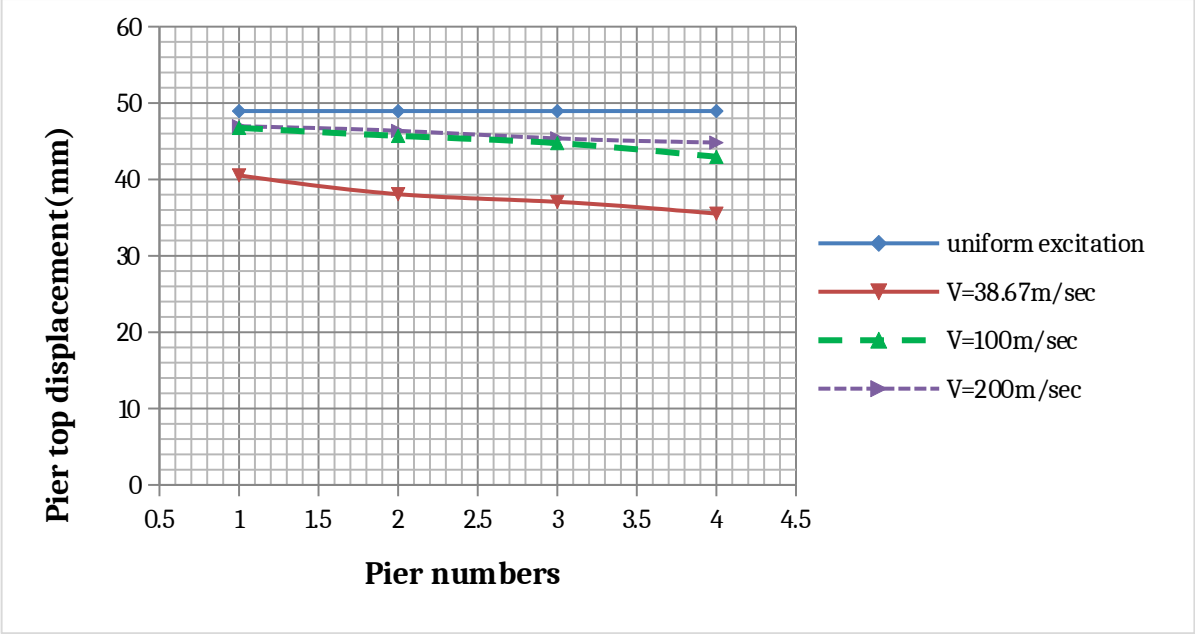


Figure 4: Pier top displacement at various wave velocities on soft soil at PGA 0.5g

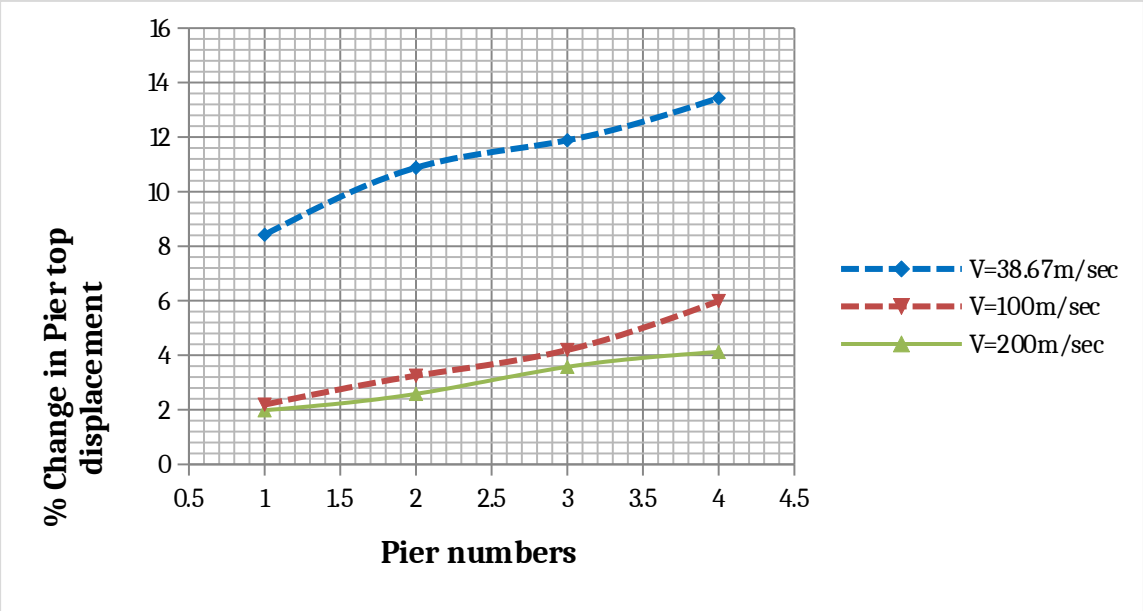


Figure 5: Percentage change in pier top displacement comparing with uniform excitation

7. CONCLUSION

For long span spatial structures, the travelling wave effect plays important role for dynamic response. The longitudinal response of structure due to wave passage effect is more significant for low velocity. It changes of response of the structure under different wave velocity for soft soil. It can be concluded that if the velocity of wave is increasing than the response of structure comparative to uniform excitation is in decreasing order and if velocity of wave becomes infinity then the structural response has no significant difference with uniform excitations.

REFERENCES

- IRC: 18 -2000 “Design criteria for prestressed concrete road bridges (post tensioned concrete)” The Indian Road Congress.
- IRC: 6-2000 “Standard Specifications and code of Practice For Road bridges” The Road Congress.
- IS: 1343- 2000 “Code of Practice for Prestressed Concrete” Indian Standard
- “Analysis of composite box girders”, Y. S. Chen & B. T. Yen.
- “Effective flange width of simply supported box girder under uniform load”, Xuxi Qin[1,2*] & Hanbing Liu[2]
- “Seismic performance of multi-span rc railway bridges”, C.T. Georgakis and X. Barrau
- CSI(2009), “Introduction to SAP2000/Bridge”, Computers and Structures Inc., Berkley, California, USA
- Clough, R. W. and Penzein, J. (1993), “Dynamics of Structure”, Second Edition, McGraw-Hill Inc.
- Chopra, A. K. (1996), Dynamics of Structure, Theory and Application to Earthquake Engineering, Eastern Economic Edition, Pentice Hall of India.

Response Reduction Factor of Steel Special Moment Resisting Frames across Building Height

Aadityananda Jha*

Department of Civil Engineering, Pulchowk Campus, Institute of Engineering, Tribhuvan University
Lalitpur, Nepal
080msste001.aadityananda@pcampus.edu.np
*Corresponding author: 080msste001.aadityananda@pcampus.edu.np

Abstract

Seismic design codes assign a response reduction factor (R) to a lateral system category irrespective of building height. This study evaluates R of Steel Special Moment Resisting Frames (SMRFs) with a single-bay (1×1, 4 × 4 m) plan and 3 to 9 storeys (9–27 m), designed for NBC 105:2025 Soil Type D. Seven models were analyzed by nonlinear static (pushover) analysis in ETABS v19 in both principal directions, using ASCE/SEI 41-13 auto hinges and a first-mode load pattern. Each capacity curve was idealized bilinearly by the FEMA 356 equal-area method, and R was decomposed following ATC-19 into ductility (R_μ), overstrength (R_s) and redundancy (R_r) factors. The applied R ranges from 3.39 to 4.53 in the X-direction and from 2.00 to 2.80 in the Y-direction, which is 56–76% and 33–47% of the NBC 105:2025-implied value of 6.0 ($R_\mu \times \Omega_u$ = 4.0×1.5). The Y-direction R is 56–62% of the X-direction value at every height, a difference traced mainly to overstrength (R_s = 3.71–4.63 in X against 2.40–3.21 in Y), while R_μ stays small (1.13–1.39) and R_r is constant (0.71). R peaks at five storeys and does not vary monotonically with height. For these frames, the code's combined ductility-and-overstrength credit is not fully mobilized, particularly in the weaker direction. The findings apply to the single-bay plan, Soil Type D and the section library used.

Keywords: response reduction factor, steel SMRF, pushover analysis, ATC-19, NBC 105:2025

Introduction

Seismic design codes permit structures to be designed for lateral forces smaller than those a linear-elastic response would demand, relying on ductile inelastic behavior and reserve strength. The reduction is expressed through a response reduction factor, R, which codes assign to each lateral system category. The Nepal National Building Code NBC 105:2025 (Department of Urban Development and Building Construction [DUDBC], 2025) assigns Steel Special Moment Resisting Frames (SMRFs) a ductility factor R_μ = 4.0 and an overstrength factor Ω_u = 1.5, so the force-reduction credit implied for the system is $R_\mu \times \Omega_u$ = 6.0, regardless of building height.

Whether this credit is actually mobilized by code-designed frames can be examined with nonlinear static (pushover) analysis, which gives the inelastic capacity curve of a structure beyond first yield (American Society of Civil Engineers [ASCE], 2014; Federal Emergency Management Agency [FEMA], 2000). ATC-19 (Applied Technology Council [ATC], 1995) splits R into ductility, overstrength and redundancy factors, so the capacity-based R of a frame, and the contribution of each component, can be compared with the value adopted in the code. Pushover-based evaluations of R have been reported for reinforced-concrete (RC) buildings in the Kathmandu Valley (Chaulagain et al., 2014) and for steel moment-resisting frames (Ferraioli

et al., 2014; Izadinia et al., 2012), and recent work on RC moment frames shows that the components of R depend on structural configuration (Suquillo et al., 2026).

Among the studies reviewed in the next section, none evaluates the full ATC-19 decomposition for a consistent series of steel SMRFs designed to NBC 105:2025 over a range of storey counts. This paper addresses that gap for the single-bay (1×1) plan. Its objectives are (i) to evaluate the ATC-19 R, and its R_μ, R_s and R_r components, of 3- to 9-storey steel SMRFs through pushover analysis; (ii) to obtain the displacement ductility of each model from the FEMA 356 equal-area bilinear idealization; (iii) to compare the computed R with the NBC 105:2025-implied value of 6.0; and (iv) to examine how building height and loading direction affect the individual components of R.

Literature Review / Related Work

ATC-19 (ATC, 1995) introduced the decomposition of R into a ductility factor, an overstrength factor and a redundancy factor, giving a rational basis for quantifying the inherent ductility, reserve strength and alternative load paths of code-designed structures. FEMA 356 (FEMA, 2000) prescribes the bilinear idealization of a pushover curve by the equal-area method, from which the effective yield point is identified, and the performance-level framework (Immediate Occupancy, Life Safety, Collapse Prevention) later codified in ASCE/SEI 41-13 (ASCE, 2014) provides acceptance criteria for plastic hinges.

Several studies have compared computed and code-prescribed R. For RC buildings in the Kathmandu Valley, Chaulagain (2010) reported that the code-assumed R did not consistently match the computed capacity, and Chaulagain et al. (2014) reported direction-dependent R for irregular RC buildings. Goud and Kumar (2014) found that overstrength and ductility contribute unequally to R depending on framing configuration, Keerthi and Philip (2017) found that the number of seismic framing lines measurably affects the redundancy component, and Patil et al. (2019) likewise reported deviations between code-specified and computed values for RC structures. Suquillo et al. (2026) showed that the components of R in RC moment frames vary with span configuration.

For steel frames, Izadinia et al. (2012) evaluated the response modification factor of steel moment-resisting frames of 3, 9 and 20 storeys with different pushover methods and obtained values of roughly 5 to 7, with an allowable-stress-type overstrength factor included in R. Ferraioli et al. (2014) found the behavior factor of code-designed steel moment-resisting frames to be sensitive to the number of storeys and bays rather than varying smoothly with height. Ushakumari Abhinand and Pandikkadavath (2025) assessed a single 4-storey special steel moment-resisting frame and reported a computed R of the same order as, but not identical to, the code value. Taken together, these studies show that a single code-prescribed R does not uniformly represent inelastic capacity across heights, configurations and detailing, which motivates the height-wise evaluation presented here.

Materials and Methods

Building models

Seven steel SMRF buildings with a single-bay (1×1) plan of 4 × 4 m and 3 to 9 storeys (total height 9–27 m, typical storey height 3 m) were modeled in ETABS v19 for a site in Kathmandu, Nepal, classified as NBC 105:2025 Soil Type D. The models differ only in the number of storeys

(Table 1). Columns are hollow rectangular (box) sections, designated ISB *d*×*b*×*t* for a section *d* mm deep, *b* mm wide and *t* mm thick, and beams are Indian Standard wide-flange I-sections (ISWB). Steel is Fe345 and the floor slab is 150 mm thick M20 concrete. Column sizes at each storey were selected so that the IS 800:2007 (Bureau of Indian Standards [BIS], 2007) axial–flexure interaction ratio fell within about 0.7–1.0, avoiding both overstressed and oversized sections; the section lists are given in Appendix A. The box columns are oriented with their strong axis resisting lateral load in the X-direction.

Design base shear

Design lateral forces follow NBC 105:2025 for Soil Type D, with zone factor Z = 0.35, importance factor I = 1.0, R_μ = 4.0, Ω_u = 1.5 and corner period T_c = 2.0 s. The fundamental period was taken as the code empirical period, $T_1 = 1.25\, k_t H^{0.75}$ with k_t = 0.085 for steel moment-resisting frames. It depends on height only, ranges from 0.552 s (3 storeys) to 1.258 s (9 storeys) and is the same in X and Y. The design base shear is

(1)

where W is the seismic weight and $C_h(T_1)$ is the spectral shape coefficient for the soil type. V_d/W equals 0.131 in every model, so V_d varies with height only through W (Table 1).

Table 1

Structural Data and Code Design Base Shear of the 1×1 Models (Soil Type D)

Storeys	Height (m)	T_1 (s)	W (kN)	Vd (kN)
3	9	0.552	327.0	42.92
4	12	0.685	440.3	57.79
5	15	0.810	561.6	73.71
6	18	0.929	693.6	91.04
7	21	1.042	817.7	107.32
8	24	1.152	921.3	120.92
9	27	1.258	1047.9	137.54

Note. T_1 = code empirical period (same in X and Y); W = seismic weight; Vd = design base shear per NBC 105:2025 for Soil Type D.

Pushover analysis

Displacement-controlled pushover analysis was run separately in the +X and +Y directions, both starting from the same nonlinear gravity case, with a lateral load pattern proportional to the first-mode shape and the roof (center of mass) as the control node. Second-order (P-Δ) effects were included in all load cases. Concentrated plastic hinges were assigned at relative distances of 0.05 and 0.95 along every beam and column using ASCE/SEI 41-13 auto hinges (Table 9-6 for beams; Table 9-7, P-M2-M3, for columns). ETABS generates the moment–rotation backbone and the Immediate Occupancy (IO), Life Safety (LS) and Collapse Prevention (CP) criteria from the member geometry, yield strength and, for columns, the axial load. Only the positive directions were analyzed because the plan and the member orientation are symmetric, so the negative directions mirror the positive ones.

Bilinear idealization and ductility

Each capacity curve (base shear against roof displacement) was replaced by an elastic–perfectly-plastic bilinear curve using the FEMA 356 equal-area rule: the initial-stiffness branch is

extended to the yield point (Δ_y, V_y), located so that the area under the bilinear curve equals the area under the pushover curve up to the ultimate displacement Δ_u. The ultimate point is the peak base shear of the analyzed curve. The displacement ductility is

(2)

ATC-19 decomposition of R

Following ATC-19 (ATC, 1995), the applied response reduction factor is the product

(3)

The ductility factor depends on the fundamental period relative to the corner period. Because $T_1 < T_c = 2.0$ s for all models, the equal-energy rule governs in both directions:

(4)

The overstrength factor is the ratio of the idealized yield strength to the code design base shear,

(5)

and the redundancy factor R_r follows ATC-19 Table 4.3 from the number of vertical seismic framing lines. Each direction of the 1×1 plan has two frame lines, giving $R_r = 0.71$ in both X and Y. The applied R is compared with the NBC 105:2025-implied value $R_\mu \times \Omega_u = 6.0$.

The significance of P-Δ effects was checked through the global stability coefficient $\theta = W\Delta_{roof}/(VH)$, where Δ_{roof} is the roof displacement, V the base shear and H the total height. FEMA 356 regards static P-Δ effects as insignificant where θ is below 0.1 in all storeys (FEMA, 2000).

Results

Capacity curves and ductility

Figure 1 shows the capacity curves and bilinear idealisations of the 9-storey model, and Table 2 lists the idealized properties of all seven models. The yield strength V_y rises with height from 159 to 578 kN in X and from 103 to 383 kN in Y, while the yield displacement Δ_y increases from 148 to 522 mm in X and from 191 to 662 mm in Y. The curves are close to linear up to yield and the post-yield strength gain is small: V_u exceeds V_y by only 5–10% in X and 2–4% in Y. Displacement ductility is therefore low, 1.33–1.47 in X and 1.14–1.26 in Y, at ultimate roof drifts of 2.2–3.4% of the building height. The Y-direction curve of the 9-storey model (Figure 1b) shows a single-step drop in base shear near the yield point, followed by recovery.

Table 2

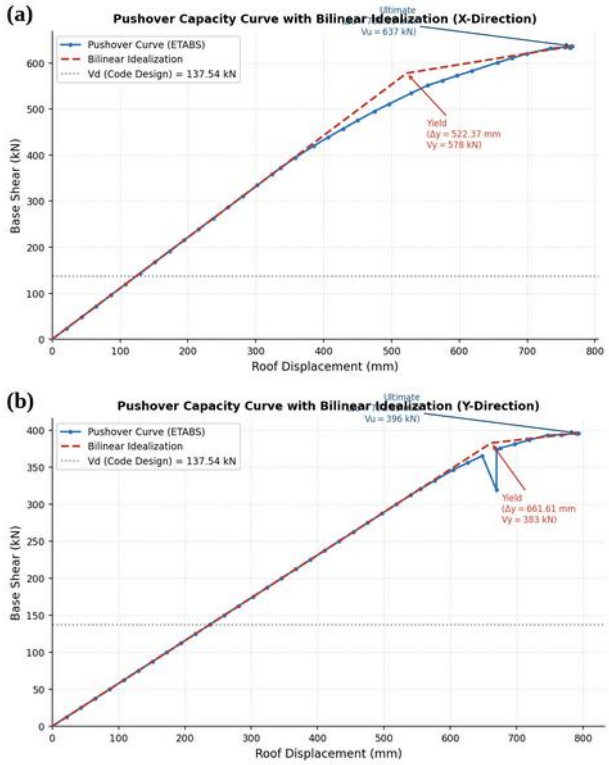
Bilinear Idealization and Displacement Ductility of the 1×1 Models

Storeys	X-direction					Y-direction				
	Δy (mm)	Vy (kN)	Δu (mm)	Vu (kN)	μ	Δy (mm)	Vy (kN)	Δu (mm)	Vu (kN)	μ
3	147.7	159.1	196.1	167.3	1.328	191.3	102.9	227.4	105.0	1.188
4	257.9	250.9	364.0	265.3	1.411	307.3	164.7	367.0	169.4	1.194
5	347.9	341.0	505.4	364.2	1.453	390.6	236.6	490.4	244.7	1.255
6	391.1	392.0	522.1	423.8	1.335	396.5	263.0	450.7	270.1	1.137
7	453.3	449.4	608.9	485.4	1.343	492.1	312.4	566.5	319.4	1.151
8	457.2	527.9	645.5	571.0	1.412	580.2	349.5	691.8	357.9	1.192
9	522.4	577.9	766.4	636.7	1.467	661.6	382.5	791.9	395.8	1.197

Note. Δy, Vy = yield displacement and base shear; Δu, Vu = ultimate displacement and base shear (peak of the analyzed curve), both at roof level; μ = Δu/Δy.

Figure 1

Pushover Capacity Curves with FEMA 356 Bilinear Idealization, 9-Storey 1×1 Model



Note. The code design base shear V_d = 137.54 kN is shown as a dotted line. ETABS output.

ATC-19 R-factor components

Table 3 gives the components of R for every model and direction. The ductility factor is small, 1.29–1.39 in X and 1.13–1.23 in Y, reflecting the low displacement ductility. The overstrength factor is the largest component: R_s = 3.71–4.63 in X and 2.40–3.21 in Y. With R_r = 0.71, the applied R is 3.39–4.53 in X and 2.00–2.80 in Y, which is 56–76% and 33–47% of the NBC 105:2025-implied value of 6.0, respectively. No model reaches the code value in either direction.

Table 3

ATC-19 Response Reduction Factor Components of the 1×1 Models

Storeys	Rr	X-direction				Y-direction			
		Rμ	Rs	Applied R	R/6.0 (%)	Rμ	Rs	Applied R	R/6.0 (%)
3	0.71	1.287	3.707	3.386	56	1.173	2.397	1.997	33
4	0.71	1.350	4.342	4.162	69	1.179	2.850	2.385	40
5	0.71	1.380	4.627	4.534	76	1.229	3.209	2.801	47
6	0.71	1.292	4.306	3.950	66	1.129	2.889	2.314	39
7	0.71	1.299	4.188	3.861	64	1.141	2.911	2.359	39
8	0.71	1.351	4.366	4.186	70	1.177	2.890	2.415	40
9	0.71	1.391	4.202	4.149	69	1.181	2.781	2.331	39

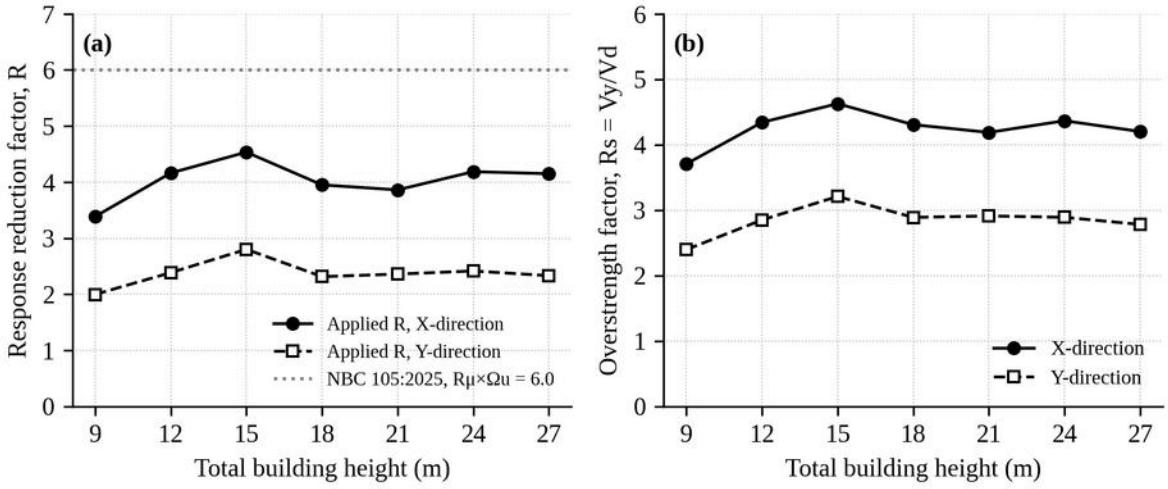
Note. Rμ = √(2μ − 1) (equal-energy rule, T_1 < Tc); Rs = Vy/Vd; Rr from ATC-19 Table 4.3 (same in X and Y); applied R = Rμ·Rs·Rr; code value = Rμ×Ωu = 4.0×1.5 = 6.0.

Variation of R with height

Figure 2a shows the applied R against building height, and Figure 2b shows the overstrength factor, which peaks at the same height. R does not vary monotonically: it rises from 3 to 5 storeys, peaks at five storeys (4.53 in X, 2.80 in Y) and then settles at a lower level for 6 to 9 storeys (3.86–4.19 in X, 2.31–2.42 in Y). Because R_r is constant and V_d/W is constant, the height-wise variation arises from R_μ and R_s. Taking the share of the variation of ln R attributable to each component as cov(ln R_k, ln R)/var(ln R) over the seven storey counts, R_s accounts for about 72% of the variation in X and 85% in Y, and R_μ for the remainder.

Figure 2

Applied R and Overstrength Factor R_s versus Building Height, 1×1 Models



Note. The dotted line in (a) is the NBC 105:2025-implied value $R_\mu \times \Omega_u$ = 6.0.

Plastic hinge performance

At the ultimate step (peak base shear), 87.5–94.6% of the hinges in each model and direction remain within the elastic (A-to-IO) range; between 4 and 11 hinges per model have yielded beyond IO, and no hinge exceeds the Life Safety level in any model or direction.

Second-order effects

The approximate global stability coefficient at the ultimate point is 0.043–0.052 in X and 0.064–0.079 in Y. Evaluated storey by storey for the 3- and 9-storey models, the governing coefficient at the ultimate point is 0.062 (X) and 0.117 (Y) for 3 storeys and 0.076 (X) and 0.142 (Y) for 9 storeys, so the Y-direction values exceed the FEMA 356 limit of 0.1. For the 9-storey model, switching P-Δ off leaves Δ_u and V_u essentially unchanged but raises the idealized ductility (1.47 to 1.57 in X; 1.20 to 1.45 in Y) and the applied R by about 2% (X) and 4% (Y), so ignoring P-Δ would overestimate R, more so where θ is larger.

Discussion

Directional asymmetry

The applied R in the Y-direction is 56–62% of the X-direction value at every storey count (mean 59%). Because the code design base shear is identical in the two directions, $R_{s,Y}/R_{s,X}$ equals the ratio of the yield strengths, 0.65–0.70, and the lower ductility in Y adds a smaller further reduction ($R_{\mu,Y}/R_{\mu,X}$ = 0.85–0.91). R_r is the same in both directions and does not contribute. The weaker Y-direction response is consistent with the orientation of the box columns, whose strong axis resists lateral load in X; this explanation was not tested by rotating the columns and should be confirmed. The result shows that a symmetric square plan does not by itself give equal reserve capacity in the two directions when the member orientation is not symmetric, and that a single code base shear applied to both directions leaves unequal margins. Unequal contributions of overstrength and ductility were also reported by Goud and Kumar (2014), and direction-dependent R by Chaulagain et al. (2014) for irregular RC buildings.

Dependence on height

The non-monotonic variation is mainly a variation of R_s. Since V_d/W is constant at 0.131, R_s reflects the yield strength coefficient V_y/W, which ranges from 0.49 to 0.61 in X and from 0.32 to 0.42 in Y and depends on the sections selected at each height. The column set changes over the range where R drops (ISB 200×100×25 first appears at 6 storeys), but the coincidence is not consistent: this section is absent from the 7-storey model, where R remains low, and ISB 200×100×20 is already used at 5 storeys, where R peaks. Beam sizes and the ductility component also differ between these models, so the cause of the dip was not isolated. A non-monotonic sensitivity of the behavior factor of steel moment-resisting frames to storey count is not unique to these models (Ferraioli et al., 2014), but this is consistent with, rather than proof of, a genuine capacity effect as opposed to an effect of discrete section selection.

Comparison with the code value and prior studies

The shortfall relative to 6.0 comes mainly from the limited ductility: the computed R_μ (at most 1.39) is far below the 4.0 assumed in the code, whereas the overstrength relative to V_d is large (R_s = 2.40–4.63) and only partly compensates, with R_r = 0.71 reducing the product further. The X-direction range of 3.39–4.53 is of the same order as, but below, the roughly 5 to 7 reported by Izadinia et al. (2012), whose R includes an allowable-stress-type factor, and a computed R of the same order as but below the code value was also reported for a 4-storey steel SMRF (Ushakumari Abhinand & Pandikkadavath, 2025). The clearer shortfall in the Y-direction is consistent with the wider finding, for RC frames as well (Chaulagain, 2010; Patil et al., 2019), that a single code-prescribed R does not uniformly represent computed capacity. For the frames studied here, the force reduction implied by R = 6.0 is therefore not supported by their computed capacity, and a direction-aware treatment of R merits consideration, subject to the limitations below.

Limitations

The results apply to a single-bay 4 × 4 m plan, which is an idealized configuration and not a complete building, to NBC 105:2025 Soil Type D only, and to the Fe345 section library used; other soil types and plans may give different results. Plastic hinges are standardized ASCE/SEI 41-13 auto hinges, not member-specific hinges, and the first-mode load pattern cannot capture higher-mode or torsional effects; R is derived from static analysis alone and has not been

validated against nonlinear time-history analysis. The ultimate point is the peak base shear of the analyzed curve, and in some models (for example Figure 1a) the curve is still rising at the last analyzed step with no hinge beyond Life Safety, so the reported ductility and R should be read as conservative estimates tied to this definition and not as collapse capacity. The single-step base-shear drop seen near yield in some curves is attributed to a hinge state-transition and solver reconvergence artifact, but this has not been confirmed against the ETABS hinge status log. The dip of R at 6–7 storeys is unexplained, and at the ultimate point the storey-level P-Δ coefficient exceeds 0.1 in the Y-direction.

Conclusion

Seven 3- to 9-storey steel SMRFs with a single-bay plan, designed to NBC 105:2025 for Soil Type D, were analyzed by pushover analysis and their ATC-19 response reduction factors were evaluated. The main findings are as follows. First, the applied R is 3.39–4.53 in the X-direction and 2.00–2.80 in the Y-direction, which is 56–76% and at most 47% of the NBC 105:2025-implied value of 6.0 and remains below it in every model and direction. Second, the displacement ductility is low (1.14–1.47), so R_μ is only 1.13–1.39, while R_s is the dominant and most variable component (2.40–4.63). Third, the Y-direction R is 56–62% of the X-direction value at every height, mainly because of overstrength, and a symmetric plan does not remove this difference. Fourth, R does not vary monotonically with height, peaking at five storeys, with R_s accounting for most of the variation; the dip at 6–7 storeys could not be linked consistently to column-section changes.

Further work should extend the study to multi-bay plans, other soil types and reinforced-concrete frames, confirm the solver artifact and the column-orientation effect, test the sensitivity of R to the adopted ultimate point, and validate the pushover-based R against nonlinear time-history analysis before any revision of code values is considered.

Acknowledgments

The author thanks Bharat Mandal for his supervision and guidance, and the Department of Civil Engineering, Pulchowk Campus, Institute of Engineering, Tribhuvan University, for the academic environment and resources that made this study possible.

Funding

The author received no financial support for the research, authorship, or publication of this paper.

Conflict of Interest

The author declares no conflict of interest.

Author Contributions

Aadityananda Jha: conceptualization, methodology, modeling and analysis, visualization, writing – original draft, writing – review and editing.

Data Availability

The ETABS models and analysis outputs supporting the findings of this study are available from the corresponding author upon reasonable request.

References

American Society of Civil Engineers. (2014). *Seismic evaluation and retrofit of existing buildings* (ASCE/SEI 41-13).

Applied Technology Council. (1995). *Structural response modification factors* (ATC-19).

Bureau of Indian Standards. (2007). *General construction in steel — Code of practice* (IS 800:2007).

Chaulagain, H. C. (2010). *Assessment of response reduction factor of RC buildings in Kathmandu Valley using non-linear pushover analysis* [Unpublished master's dissertation]. Khwopa Engineering College, Purbanchal University.

Chaulagain, H., Rodrigues, H., Spacone, E., Guragain, R., Mallik, R., & Varum, H. (2014). Response reduction factor of irregular RC buildings in Kathmandu valley. *Earthquake Engineering and Engineering Vibration, 13*(3), 455–470. https://doi.org/10.1007/s11803-014-0255-8

Department of Urban Development and Building Construction. (2025). *Nepal National Building Code NBC 105:2025: Seismic design of buildings in Nepal*. Government of Nepal.

Federal Emergency Management Agency. (2000). *Prestandard and commentary for the seismic rehabilitation of buildings* (FEMA 356).

Ferraioli, M., Lavino, A., & Mandara, A. (2014). Behaviour factor of code-designed steel moment-resisting frames. *International Journal of Steel Structures, 14*(2), 243–254. https://doi.org/10.1007/s13296-014-2005-1

Goud, S. S., & Kumar, R. P. (2014). Rationalizing response reduction factor (R) for better performance of reinforced concrete framed buildings. In *Proceedings of the two day national conference on recent research advances in civil engineering (RRACE–2014)* (pp. 1–6). IIIT-Hyderabad.

Izadinia, M., Rahgozar, M. A., & Mohammadrezaei, O. (2012). Response modification factor for steel moment-resisting frames by different pushover analysis methods. *Journal of Constructional Steel Research, 79*, 83–90. https://doi.org/10.1016/j.jcsr.2012.07.010

Keerthi, S., & Philip, V. (2017). Evaluation of response reduction factor based on redundancy for high rise buildings. *International Research Journal of Engineering and Technology, 4*(5), 3161–3165.

Patil, U., Kabra, N., Hiwase, P. D., & Siddh, S. P. (2019). Analytical study of response reduction factor of RCC structures. *Helix, 9*(6), 5768–5770. https://doi.org/10.29042/2019-5768-5770

Suquillo, B., Villavicencio, S., Medina, C. D., & Cagua, B. (2026). Configuration-sensitive decomposition of the response modification factor in reinforced concrete moment frames. *Buildings, 16*(14), Article 2752. https://doi.org/10.3390/buildings16142752

Ushakumari Abhinand, P., & Pandikkadavath, M. S. (2025). Seismic response reduction factor assessment of a 4-storey special steel moment resisting frame. *Procedia Structural Integrity, 70*, 129–136. https://doi.org/10.1016/j.prostr.2025.07.035

Appendix A

Table A1

Column and Beam Sections Used in the 1×1 Models

Storeys	Column sections (ISB d×b×t, mm)	Beam sections
3	172×92×6.5, 172×92×3.5	ISWB125, ISWB150
4	172×92×12, 172×92×6.5, 172×92×8, 172×92×3.5	ISWB125, ISWB150
5	200×100×10, 200×100×15, 200×100×20, 172×92×5.4	ISWB125, ISWB150
6	200×100×10, 200×100×15, 200×100×25, 172×92×5.4	ISWB125, ISWB150, ISB 200×100×20
7	200×100×5, 200×100×10, 200×100×12, 200×100×15, 200×100×20	ISWB125, ISWB150
8	200×100×5, 200×100×10, 200×100×12, 200×100×15, 200×100×20, 200×100×22, 200×100×25, 172×92×5	ISWB150, ISWB175, ISWB200, ISWB250
9	200×100×5, 200×100×7.5, 200×100×10, 200×100×12, 200×100×15, 200×100×20, 200×100×25, 200×100×32.5, 200×100×35	ISWB150, ISWB200, ISWB250

Note. Section designations as defined in the ETABS models; the box columns have their strong axis along the X-direction.

Basin-Modified Response Spectra for Seismic Design in Kathmandu Valley

Happy Yadav[1], Assoc. Prof. Hari Ram Parajuli[2], Asst. Prof. Sunita Ghimire[3]

[1]Department of Civil Engineering, Pulchowk Campus, Institute of Engineering, TU
Lalitpur, Nepal
MSc in Structural Engineering, PUL080MSStE009; 080msste009.happy@pcampus.edu.np
[2]hariparajuli@ioe.edu.np; [3]ghimiresunitag@gmail.com

Abstract

The Kathmandu Basin lies in a high-seismically active region and is underlain by a deep sedimentary basin that amplifies and prolongs earthquake ground motion. However, the design code has not provided proper guidelines for the development of basin sensitive site-specific response spectra. This study provides an approach to develop site-specific, basin-modified response spectra by comparing international code spectra, constructing data-driven 5%-damped spectra from 2015 Gorkha earthquake records (M > 6) at the KTP, TVU, PTN and THM stations, and performing two-dimensional non-linear site response analysis in FLAC2D. Results show strong site-to-site variation: fundamental periods increase from 0.625 s at the rock site KTP to 2.5 s at TVU, 3.3 s at PTN and about 5 s at THM, with amplification factors of 2.6, 3.1 and 3.5 respectively. The simulated response spectra rank the sites in the same order, with short-period spectral acceleration at THM about 1.6 times that at TVU, but they do not reproduce the long-period maxima of the recorded-motion spectra. A single uniform spectrum therefore cannot represent seismic demand across the Basin, and basin effects should be incorporated into the design. Future work should use all three ground-motion components, more records and stations, and three-dimensional models, with validation against independent records.

Keywords: Amplification, Basin Effect, Peak Ground Acceleration, Site-Specific Response Spectrum, Site Response Analysis, Spectral Shape

Introduction

Nepal lies on the collision boundary between the Indian and Eurasian plates and is among the most earthquake-prone countries in the world. The capital, Kathmandu Valley, is home to more than 850,000 people and many culturally important structures, and sits in a bowl-shaped, trapezoidal tectonic basin of about 665 km² that was once a lake. The basin is filled with up to roughly 600 m of semi-consolidated Plio-Pleistocene fluvial and lacustrine sediments overlying hard metamorphic bedrock (Bijukchhen, 2018; Koketsu, 2024).

When seismic waves enter such a basin they slow down in the soft sediments and are trapped, reflected and focused by the basin edges, which increases shaking intensity, lengthens its duration and shifts energy towards long periods. Basin effects of this kind have shaped damage in earlier events such as Mexico City in 1985 and were clearly observed in Kathmandu during the 2015 Mw 7.8 Gorkha earthquake, where low-frequency reverberating pulses and depleted high-frequency content were recorded inside the basin (Asimaki et al., 2019; Ayoubi et al., 2018; Takai et al., 2016). Because the sediment thickness varies strongly across the valley, the response differs from one location to another.

The response spectrum, which gives the peak response of a single-degree-of-freedom (SDOF) oscillator as a function of period and damping, is the basic tool for defining seismic demand in design codes (Gupta, 1990). NBC 105:2025 and the other codes considered here treat local soil

through site classes and soil-dependent spectra, but they do not explicitly represent two- or three-dimensional basin effects. Studies have shown that one-dimensional analysis has limits in basins and that two-dimensional models reproduce basin-edge and wave-trapping effects better (Ayoubi et al., 2020). A localized, data-driven spectrum that integrates recorded motions and basin-specific amplification is therefore missing for the valley.

The objectives of this paper are (a) To develop Data-driven response spectra using mainshocks and aftershocks of 2015 Gorkha earthquake; (b) To obtain static and dynamic displacement, shear stress, site amplification factor and Surface acceleration time history at three sites (TVU, PTN and THM) of Kathmandu basin.; and (c) To derive Site-Specific Response Spectra for three sites (TVU, PTN and THM) of Kathmandu Basin.

Literature Review / Related Work

Sreejaya et al. (2025) used a two-dimensional spectral element method to compare foreland, rectangular, parabolic and trapezoidal basins. Foreland basins produced the strongest long-period amplification, rectangular basins less, and parabolic basins the least, while greater basin depth and epicentral distance increased amplification through resonance and surface-wave dominance. Chiou et al. (2008) found for the Taipei Basin that spectral accelerations at medium and long periods decay more slowly for large events ($M \geq 6.5$), and that the spectral shape depends on both basin effects and source characteristics, with some sites requiring reclassification within the existing micro-zonation.

For Kathmandu, Wei et al. (2017) combined finite-fault source modelling with 3D simulations and showed that the long-period and prolonged shaking of the Gorkha sequence resulted from rupture directivity, asperity distribution and basin amplification near 0.2 Hz. Hernández-Aguirre and Rupakhety (2024) reproduced aftershock records with 3D physics-based simulations and found strong amplification below 0.9 Hz and higher peak velocities in the western basin, but their linear viscoelastic model could not represent soil non-linearity. Ayoubi et al. (2018) compared 1D non-linear and 2D numerical models with Gorkha records: the 1D model agreed better over a wider frequency range except near basin edges, whereas the 2D model reproduced the low-frequency basin response but struggled at high frequencies. Pagliaroli et al. (2018) also assessed site effects in the valley with 1D and 2D modelling. Poudyal et al. (2024) mapped a seismic vulnerability index from dominant frequency and amplification factor.

Asimaki et al. (2019) showed for Mexico City that deep basin heterogeneity, basin-edge interaction with shallow clay and changes in groundwater conditions control site response, so that different earthquake types affect different building classes. Bijukchhen (2018) constructed a 3D velocity structure model of the Kathmandu Basin from geological information and ground-motion records and showed that velocity contrasts and basin geometry strongly amplify waves and lengthen shaking. Together, these studies indicate that basin geometry, depth, soil non-linearity and source characteristics all control the spectral shape, yet a site-specific spectrum for individual Kathmandu stations has not been proposed for code use.

Materials and Methods

Research design

A descriptive and causal-comparative design was adopted. The workflow (Figure 1) combines a review of international code spectra, construction of data-driven response spectra from recorded

earthquakes, numerical simulation of site response, and a post-seismic comparison of the two spectra as the basis for a site-specific spectrum. Finally, the basin sensitive site-specific response spectra will be developed for the give three sites (TVU, PTN and THM) of the Kathmandu basin.

Figure 1

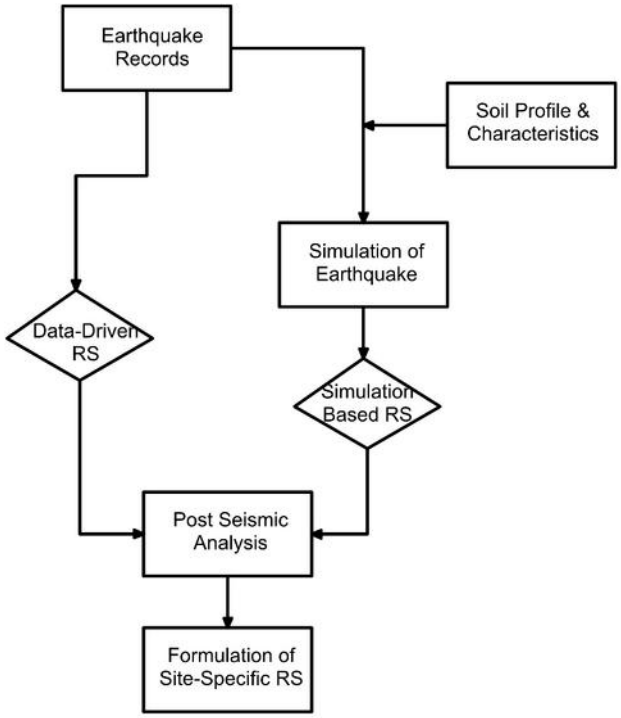


Figure 1: *Research methodology adopted in the study*

Study area, stations and ground motions

Ground motions were taken from four permanent strong-motion stations in the basin (Figure 2): KTP, on a bedrock outcrop of meta-sandstone and phyllite with Vs of about 720 m/s, and TVU, PTN and THM, on thick soft basin sediments with Vs of about 200 m/s near the surface. TVU and PTN lie on the Kalimati Formation and THM on the Gokarna Formation. Records of the 2015 Gorkha mainshock and the four aftershocks of magnitude above 6.0 listed in Table 1 were used. The KTP motion was treated as the rock-outcrop input for the other sites, and a 10 m thick bedrock layer with KTP properties was assumed beneath each profile.

Figure 2

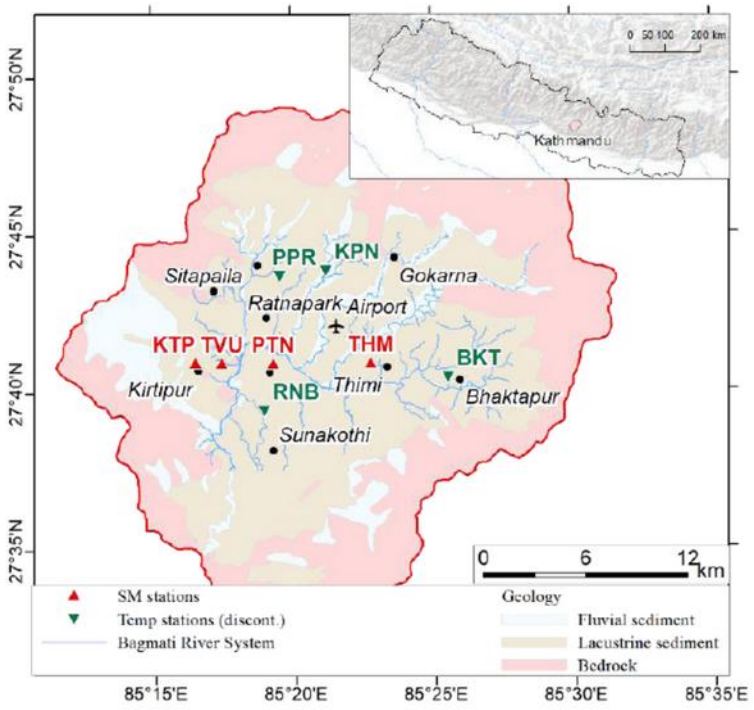


Figure 2: *Kathmandu Basin and the strong-motion stations used in the study*
Note: Adopted from General geology after Shrestha et al. (DMG, 1998) in the thesis.

Table 1

Strong ground motions considered in the study

No.	Date (2015)	Location	Lat.	Long.	Depth (km)	Mw
1	25 April, 11:56	Barpak, Gorkha	28.230°N	84.731°E	8.2	7.8
2	25 April, 06:45:21	Gorkha	28.224°N	84.822°E	10	6.6
3	26 April, 07:09:11	Sindhupalchowk	27.771°N	86.017°E	22.9	6.7
4	12 May, 07:05:20	Dolakha	27.809°N	86.065°E	15	7.3
5	12 May, 07:36:54	Dolakha	27.625°N	86.162°E	15	6.3

Note. Event times are as listed in the source thesis.

Response spectrum and design-code comparison

For a linear SDOF system with natural frequency ω, damping ratio ξ and ground acceleration, the equation of motion is given by Equation 1, and the response spectrum is the plot of the peak response of many such oscillators against period (Gupta, 1990). The spectral shape factors for very soft soil in NBC 105:2025, IS 1893:2025, NZS 1170.5:2004, Eurocode 8 and ASCE 7-22 were compared with respect to soil classification, spectral shape and basin-effect treatment.

(1)

Data-driven response spectra

For every NS and EW accelerogram, a 5%-damped elastic response spectrum was computed with SeismoSignal and processed in Excel. The spectra of the five events at each station were compared to identify amplification, spectral shape and long-period content, with the mainshock providing the governing demand.

Geotechnical characterization

Shear-wave velocity and layer depths for TVU, PTN and THM were taken from Bijukchhen (2018), Koketsu (2024) and the SAFER geodatabase, supported by borehole logs. Missing properties were obtained from the empirical relations of Brocher (2005) in Equations 2 to 5, (Vs in m/s and density in g/cm³). The resulting layer properties are given in Table 2.

(2)

(3)

(4)

(5)

Two-dimensional site response analysis

One-dimensional analysis did not give satisfactory results and basin effects were not prominent in it, so two-dimensional models of TVU, PTN and THM were built in FLAC2D, an explicit finite-difference code that solves the equations of motion in time steps. The 800 m wide models extend to bedrock and were built as uniform and non-uniform layered columns (Figure 3). The TVU profile is 325 m deep (weathered rock 20 m, boulder 120 m, gravel 30 m, sand 75 m, clay 60 m, fill 20 m), the PTN profile 350 m (weathered rock 20 m, boulder 150 m, gravel 30 m, clay 130 m, fill 20 m) and the THM profile 460 m (weathered rock 20 m, boulder 180 m, gravel 30 m, clay 210 m, fill 20 m). Zone size followed Equation 6, and non-linear behaviour was represented with the Mohr-Coulomb model, with Rayleigh damping calibrated to the fundamental frequency of each site.

(6)

The models were first brought to static equilibrium under gravity. The base motion was the KTP EW record of the Gorkha mainshock, converted to a shear-stress history by Equation 7 and applied at the base of the bedrock layer, with free-field boundaries at the sides. Free-vibration analysis of a linear elastic 1D column gave the fundamental frequency from the dominant FFT peak. Acceleration histories were recorded at the bottom (0.5 m above bedrock), middle and top of each profile.

(7)

Five-percent-damped acceleration (Sa), velocity (Sv) and displacement (Sd) response spectra were also computed for periods up to 4 s from the simulated surface motion at each of the three sites, and their characteristic ordinates were compared between the sites (Figures 7 to 9, Table 6).

Table 2

Soil properties used in the FLAC2D simulations

Layer	V_s (m/s)	V_p (m/s)	μ	ρ (kg/m³)	G (MPa)	K (MPa)	c (kPa)	φ (°)
Fill	200	500	0.30	1651.08	66.04	143.09	20	28
Clay	300	750	0.30	1836.13	165.25	358.04	30	30
Sand	350	875	0.30	1911.80	234.20	507.42	0	34
Gravel	400	1000	0.25	1979.87	316.78	527.97	10	34
Boulder	500	1250	0.25	2099.07	524.77	874.61	5	38
Weathered rock	700	1750	0.25	2292.52	1123.33	1872.22	–	–
Bedrock	3200	8000	0.25	2612.36	26750.6	26341.3	–	–

Note. Dilation and tension were set to zero for the soil layers. Properties follow Bijukchhen (2018) and Brocher (2005).

Figure 3

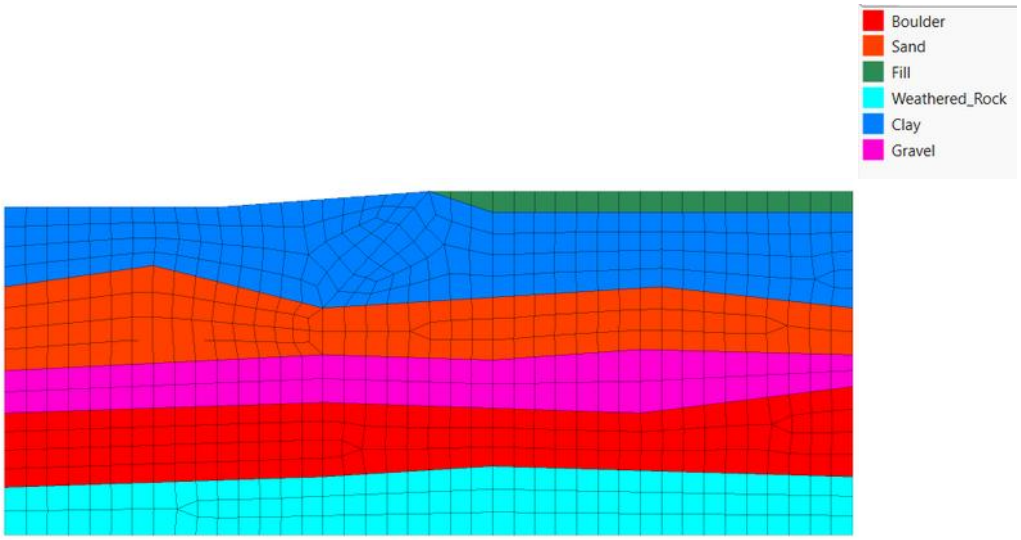


Figure 3: *Non-uniform two-dimensional FLAC2D model of the TVU site*
Note. Colours denote the soil layers; the uniform model has horizontal layer boundaries.

Results

Comparison of international design spectra

Table 3 summarizes how the five codes treat soil and basin effects. All of them classify sites by soil class, typically using Vs,30, SPT N-value or undrained shear strength, and apply soil-dependent amplification, but none represents the 2D or 3D behaviour of a deep basin in its standard spectrum. Basin effects are addressed mainly through site-specific response analysis (ASCE 7-22, NZS 1170.5, IS 1893) or site subcategories (Eurocode 8), while NBC 105:2025 recognizes the need to include them in future editions. The New Zealand standard has since been revised as TS 1170.5:2025 (Elwood et al., 2025). The NBC 105:2025 spectrum has a constant plateau of 2.5 for classes A to C and 2.25 for class D, with corner periods of 0.5 to 2.0 s and a range up to 6 s.

Table 3

Selected provisions of the design codes compared

Code	Soil classification	Spectral shape	Basin-effect approach
NBC 105:2025 (Nepal)	Vs,30, N-value and Cu; classes A to D	Plateau 2.5 (A–C), 2.25 (D); corner periods 0.5–2.0 s; to 6 s	Limited; to be included in future editions
IS 1893:2025 (India)	Vsi from SPT N; classes A to D, provision for E	Plateau 2.5; corner periods 0.4–0.8 s; extended to 10 s	Limited; site-specific analysis encouraged
NZS 1170.5:2004 (New Zealand)	Five classes A to E	Shape factors from probabilistic hazard; near-fault effects	Through site response studies
Eurocode 8 (Europe)	Five categories A to E and special sites	Standardized parametric shapes with soil factors	Via site subcategories and ground-motion models

Code	Soil classification	Spectral shape	Basin-effect approach
ASCE 7-22 (USA)	Six classes A to F (Vs,30, N, Cu)	Mapped SDS and SD1 with soil amplification	Explicit; site-specific analysis encouraged

Note. Summarized from the code comparison in the source thesis.

Data-driven response spectra

Figure 4 compares the 5%-damped spectra of the Mw 7.8 mainshock at the four stations, and Table 4 lists the peak values. At the rock site KTP, the demand is concentrated at short periods (about 0.2 to 0.4 s) and decays quickly beyond 1 s; the EW component reaches about 1.0g, nearly twice the NS value. At TVU the spectra are broad with multiple peaks between 0.2 and 3 s, and the EW component sustains a high plateau at 1 to 3 s, indicating combined soil resonance and basin amplification. At PTN the spectral accelerations remain high over a broad band from about 1 to 4 s, with an EW peak near 1.5 s and a secondary hump near 3.5 s. At THM the mainshock peak shifts to very long periods, about 3.9 s (NS) and 4 to 5 s (EW), which is characteristic of trapped energy in the deep soft sediments; the Dolakha Mw 7.3 aftershock produced a sharp EW peak near 1 s at the same site.

Figure 4

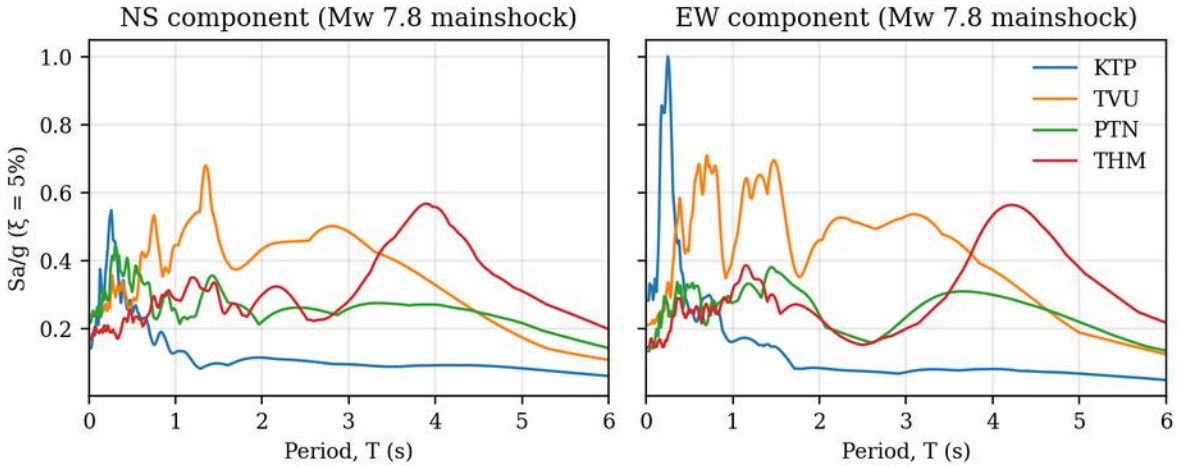


Figure 4: *Data-driven response spectra (ξ = 5%) of the Gorkha Mw 7.8 mainshock at the four stations*

Table 4

Peak spectral acceleration of the Gorkha Mw 7.8 mainshock (ξ = 5%)

Station	NS Sa/g	Period (s)	EW Sa/g	Period (s)
KTP	0.55	0.26	1.00	0.25
TVU	0.68	1.35	0.71	0.70
PTN	0.44	0.30	0.38	1.45
THM	0.57	3.90	0.56	4.22

Note. Values are the maximum ordinates of the computed spectra; periods are those at which the maximum occurs.

Free vibration and simulated site response

The FFT of the free-vibration response (Figure 5) gives fundamental frequencies of 0.4 Hz at TVU, 0.3 Hz at PTN and 0.2 Hz at THM, against 1.6 Hz at KTP. The corresponding periods are about 2.5, 3.3 and 5 s, so resonance moves to longer periods as the sediments get thicker (THM < PTN < TVU in frequency).

Figure 5

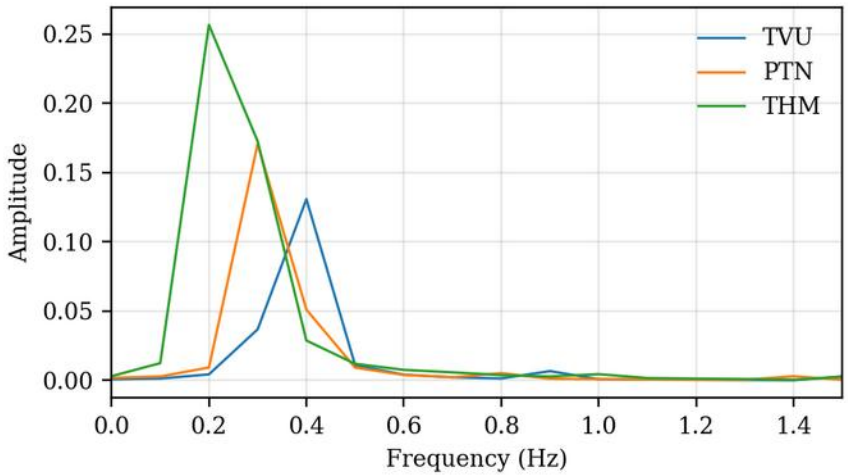


Figure 5: *FFT spectra from free-vibration analysis of the TVU, PTN and THM models*

Static analysis established the initial stress state, and the dynamic analysis then produced strong, continuous reversal and redistribution of shear stress with concentrations at layer boundaries and at the irregular geometry of the non-uniform models; the X-displacement changed from weak mixed-sign values to large negative displacements. The simulated acceleration histories (Figure 6) show strong modification of the input motion. The surface peak acceleration is 3.6 m/s² at TVU against 1.4 m/s² at the base (ratio about 2.6), 5.48 m/s² against 1.76 m/s² at PTN (about 3.1), and 5.30 m/s² against 1.51 m/s² at THM (about 3.5). The results are summarized in Table 5.

Figure 6

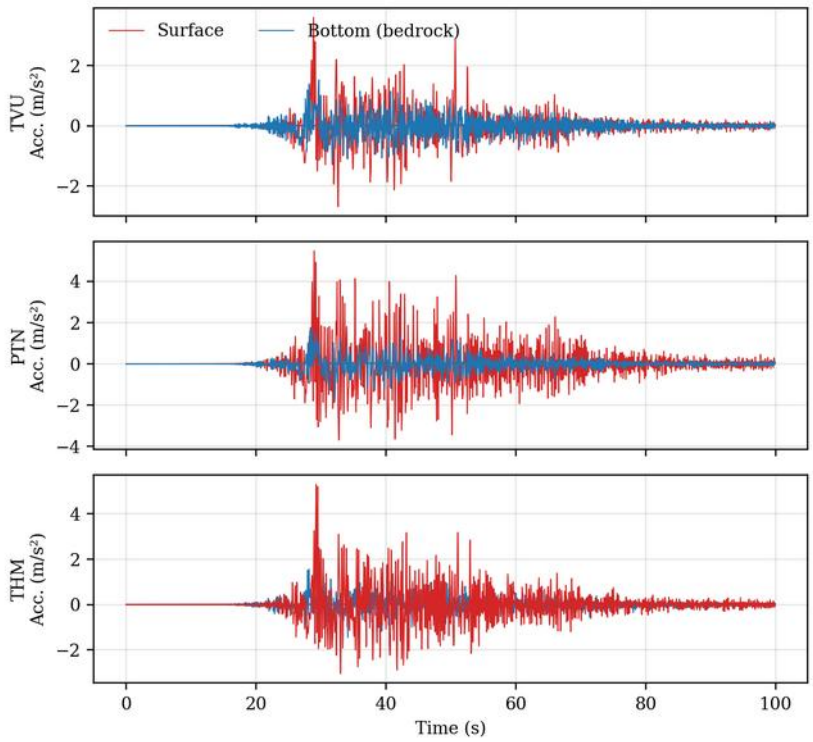


Figure 6: *Simulated acceleration histories at the bottom and surface of the TVU, PTN and THM profiles*

Table 5

Summary of site response results

Site	Soil depth (m)	f_1 (Hz)	T_1 (s)	Base PGA (m/s²)	Surface PGA (m/s²)	Ratio
KTP (rock)	–	1.6	0.63	–	–	–
TVU	325	0.4	2.5	1.4	3.6	2.6
PTN	350	0.3	3.3	1.76	5.48	3.1
THM	460	0.2	5.0	1.51	5.30	3.5

Note. f_1 and T_1 are the fundamental frequency and period; ratio is surface to base peak acceleration.

The hysteresis loops at the three sites are closed, confirming that part of the input energy is dissipated in the soil, and the loops broaden with increasing strain as the effective shear stiffness degrades. The loop steepness, and hence shear stiffness, follows TVU > PTN ≈ THM, whereas the loop area, and hence energy dissipation, follows PTN > TVU > THM.

Simulation-based response spectra

Figures 7 to 9 show the 5%-damped acceleration (Sa), velocity (Sv) and displacement (Sd) spectra of the simulated site response at TVU, PTN and THM, and Table 6 lists their characteristic ordinates. At all three sites Sa is largest at the shortest period plotted (0.1 s), where it reaches 2.43 m/s² at TVU, 2.70 m/s² at PTN and 3.88 m/s² at THM, and it then decays rapidly: at 0.2 s it is only 31 to 37% of the 0.1 s value, and at 0.5 s it is below 0.15 m/s² at every site. The

ordinates beyond about 1 s are negligible, so no spectral peak appears at the fundamental periods of 2.5, 3.3 and 5 s obtained from the free-vibration analysis.

Figure 7

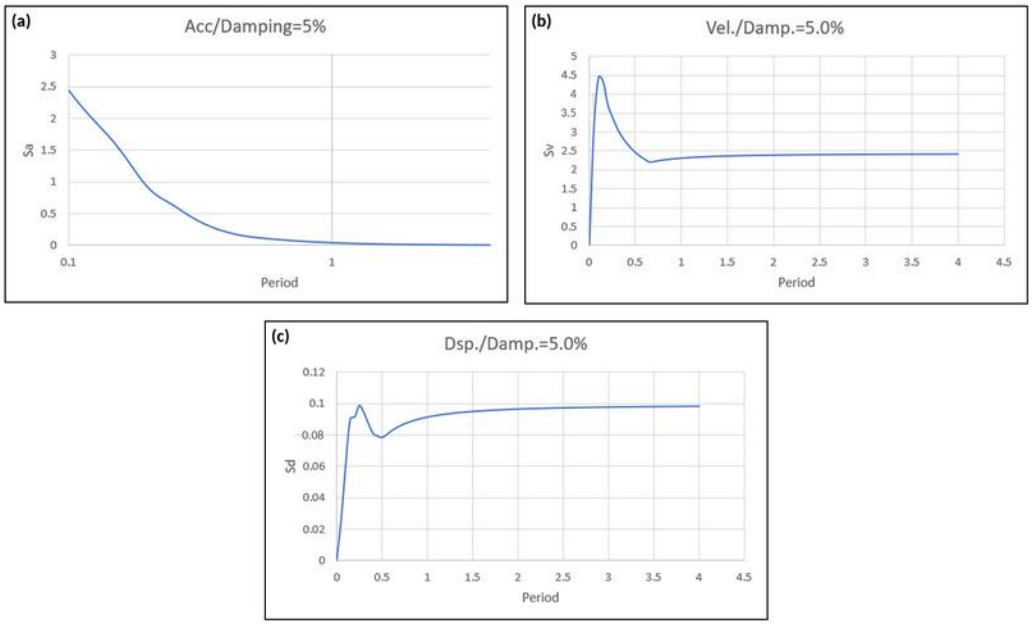


Figure 7: *Simulation-based 5%-damped response spectra at the TVU site: (a) acceleration, (b) velocity and (c) displacement*

Figure 8

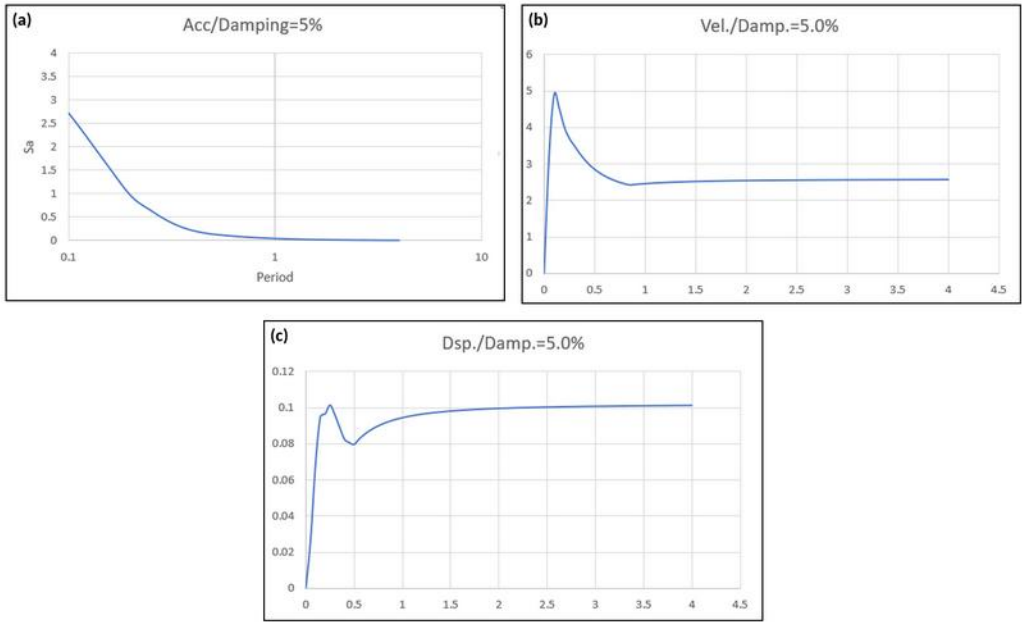


Figure 8: *Simulation-based 5%-damped response spectra at the PTN site: (a) acceleration, (b) velocity and (c) displacement*

Figure 9

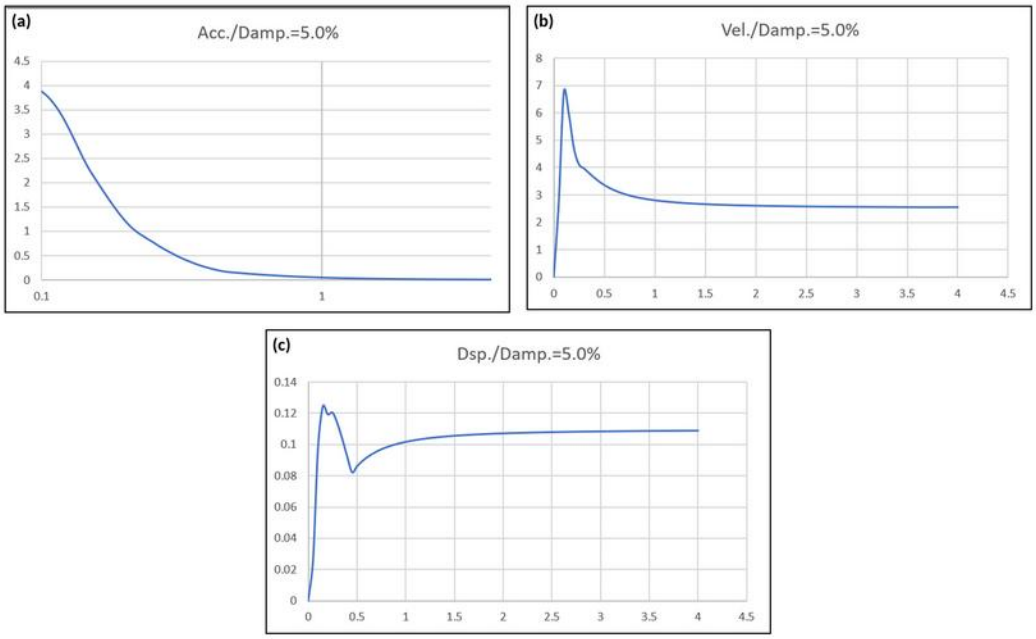


Figure 9: *Simulation-based 5%-damped response spectra at the THM site: (a) acceleration, (b) velocity and (c) displacement*

Note. Horizontal axes show period (s); Sa is in m/s², Sv in cm/s and Sd in cm. Figures 8 and 9 use the same axes.

Table 6

Characteristic ordinates of the simulation-based response spectra (ξ = 5%)

Site	Sa at 0.1 s (m/s²)	Peak Sv (cm/s)	T at peak Sv (s)	Peak Sd (cm)	T at peak Sd (s)	Sd at 4 s (cm)	Sa ratio to TVU
TVU	2.43	4.46	0.11	0.099	0.25	0.098	1.00
PTN	2.70	4.93	0.10	0.101	0.25	0.101	1.11
THM	3.88	6.79	0.10	0.125	0.16	0.109	1.60

Note. Values were read from the plotted curves in Figures 7 to 9 and are approximate. Sa, Sv and Sd are spectral acceleration, velocity and displacement; T is the period at which the peak occurs. Sd at 4 s is the long-period plateau value; the ratio is Sa at 0.1 s relative to TVU.

The velocity spectra rise steeply to a sharp peak at about 0.10 to 0.11 s, of 4.46 cm/s at TVU, 4.93 cm/s at PTN and 6.79 cm/s at THM, and then decrease. At TVU and PTN they pass through a shallow minimum (2.20 cm/s at 0.65 s and 2.43 cm/s at 0.84 s) and level off at about 2.4 and 2.6 cm/s, whereas at THM they decay steadily towards about 2.6 cm/s. The displacement spectra increase rapidly to a first peak between 0.15 and 0.25 s, fall to a local minimum of 0.078 to 0.082 cm near 0.45 to 0.5 s, and then recover gradually to long-period plateaus of 0.098 cm (TVU), 0.101 cm (PTN) and 0.109 cm (THM). The largest displacement peak, 0.125 cm at 0.16 s, occurs at THM, against 0.099 cm at TVU and 0.101 cm at PTN.

Discussion

The data-driven and simulated results agree in how they rank the sites, although not in spectral shape (discussed below). The rock station KTP shows a short-period peak and little long-period

demand, whereas the basin stations show broad or long-period amplification that grows with sediment depth. The amplification ratio increases in the order TVU < PTN < THM, matching the increase in soil depth from 325 m to 350 m and 460 m and the fall in fundamental frequency from 0.4 Hz to 0.2 Hz. This agrees with earlier findings that thick basin sediments trap energy and lengthen shaking at low frequencies (Hernández-Aguirre & Rupakhety, 2024; Wei et al., 2017) and with the observation of Chiou et al. (2008) that long-period spectral ordinates decay more slowly in basins.

The simulation-based spectra (Figures 7 to 9, Table 6) give the same ranking of the three basin sites. Relative to TVU, the short-period acceleration ordinate Sa at 0.1 s is about 1.1 times larger at PTN and 1.6 times larger at THM, the peak velocity is about 1.1 and 1.5 times larger, and the peak displacement about 1.0 and 1.3 times larger. The increase is concentrated at THM, the site with the deepest sediments (460 m) and the thickest clay layer (210 m, against 130 m at PTN and 60 m at TVU). The order TVU < PTN < THM also appears in the surface-to-base amplification ratios (2.6, 3.1 and 3.5), although the spectral ratios are not proportional to them, which suggests that layer thickness alone does not control the spectral level and that stiffness contrasts and the layer sequence also matter. At long periods the Sv and Sd plateaus, which approach the ground velocity and displacement of the motion, differ by only about 7% and 3 to 11% between the sites, much less than the short-period differences, so in the simulations the basin mainly intensifies the short-period motion.

The two sets of spectra differ clearly in shape. The simulated Sa falls below 0.15 m/s² (about 0.015 g) by 0.5 s at every site and shows no peak at the fundamental periods from the free-vibration analysis, whereas the recorded-motion spectra at the same stations have peak ordinates of 0.38 to 0.71 g, at periods from about 0.3 s to 4.2 s that tend to increase towards the basin centre (Table 4). The present two-dimensional model therefore reproduces the ordering of the sites and the amplification of the surface motion, but not the long-period resonance seen in the recorded data. This also differs from the low-frequency basin response reproduced by the two-dimensional models of Ayoubi et al. (2018). Possible reasons are that the model is an 800 m wide layered column with a base-applied shear-stress input and free-field side boundaries, so that basin-edge and wave-trapping effects are not generated; that the Mohr-Coulomb model with Rayleigh damping calibrated at the fundamental frequency represents damping in a simplified way; that a single rock-site record (KTP, EW component) was used as input; and that the fundamental periods came from a linear elastic free-vibration analysis, which is not directly comparable with the non-linear dynamic response. The simulated spectra should therefore be read as a measure of relative site-dependent amplification and not as a direct estimate of design demand at long periods.

Two practical implications follow. First, the periods of peak demand differ greatly between sites, from about 0.25 s at KTP to about 4 s at THM, so a single soft-soil spectrum cannot represent all valley sites; a generic plateau and decay shape for one soil class may underestimate demand for mid-rise to tall structures and bridges at PTN and THM while overestimating it elsewhere. Second, the EW and NS components differ at the same station (for example at KTP and TVU), so a single averaged spectrum can hide direction-dependent demand. The code comparison shows that no standard spectrum considered here includes explicit basin amplification, which supports adding basin-specific provisions, or site-specific analysis, to NBC 105.

Taken together, the data-driven spectra (Figure 4) and the simulation-based spectra (Figures 7 to 9) give the site-specific response spectra obtained in this study for TVU, PTN and THM, with

the rock site KTP as the reference. Converting them into design spectra, for example as spectral shape factors calibrated to a common hazard level, will require the long-period part of the simulated spectra to be brought into agreement with the recorded motions, which is a priority for future three-dimensional and non-linear modelling.

Limitations

Only five earthquake records (Mw above 6.0) and four stations were used, and the numerical simulation used only the EW component of the mainshock as input. The 1D and 2D models cannot fully represent three-dimensional wave propagation in the heterogeneous basin, and the Mohr-Coulomb constitutive model with Rayleigh damping represents soil non-linearity in a simplified way. Authentic engineering properties of the soil were unavailable, so empirical relations and the data of Bijukchhen (2018) were used. The findings reflect data and codes available up to 2025 and should be updated as new records and research become available. The simulated response spectra come from a single input motion and do not reproduce the long-period maxima of the recorded-motion spectra, so they should be validated before they are used to define design spectral shapes.

Conclusion

The study shows that basin effects in the Kathmandu Valley are prominent and site-dependent and should be reflected in NBC 105. The rock site KTP has a high fundamental frequency (1.6 Hz, 0.63 s), whereas the basin sites have fundamental frequencies of 0.4 Hz (TVU), 0.3 Hz (PTN) and 0.2 Hz (THM), with surface-to-base amplification ratios of about 2.6, 3.1 and 3.5. The data-driven spectra show peak demand moving from short periods at KTP to about 4 s at THM. The simulated 5%-damped spectra rank the sites in the same order, with Sa at 0.1 s of 2.43, 2.70 and 3.88 m/s² at TVU, PTN and THM, but they are dominated by short periods and do not reproduce the long-period maxima of the recorded-motion spectra. Using one uniform response spectrum for all locations may therefore not represent actual seismic demand, and site-specific analysis that considers soil thickness, stiffness and shear-wave velocity is recommended.

Future work should include both horizontal components and the vertical component, a larger set of records from the Himalayan region, more stations, three-dimensional models, non-linear soil behaviour, validation against independent records and comparison with code spectra, and integration with probabilistic seismic hazard analysis to produce hazard-consistent basin-modified spectra.

Acknowledgments

The author thanks the project supervisor, Assoc. Prof. Dr. Hari Ram Parajuli, the co-supervisors Asst. Prof. Sunita Ghimire and Dr. Govinda Pd. Niroula, and the program coordinator Prof. Dr. Kshitiz C. Shrestha for their guidance, and the faculty and staff of the Department of Civil Engineering, Pulchowk Campus, for their support. This paper is based on the MSc thesis submitted to Tribhuvan University, Institute of Engineering.

Funding

The author received no financial support for the research, authorship, or publication of this paper.

Conflict of Interest

The author declares no conflict of interest.

Author Contributions

Happy Yadav: conceptualization, methodology, software, formal analysis, investigation, visualization and writing.

Data Availability

The strong-motion records and soil profiles were obtained from the sources cited in the paper (Bijukchhen, 2018; Koketsu, 2024; Takai et al., 2016). The derived spectra and model outputs are available from the author on reasonable request.

References

Asimaki, D., Mayoral Villa, J., Ayoubi, P., Franke, K., & Hutchinson, T. (2019). Mexico City basin effects: Past, present and future. In *Geo-Congress 2019: Earthquake engineering and soil dynamics* (GSP 308, pp. 422–435). American Society of Civil Engineers. https://doi.org/10.1061/9780784482100.043

Ayoubi, P., Asimaki, D., & Mohammadi, K. (2018). Basin effects in strong ground motion: A case study from the 2015 Gorkha, Nepal earthquake. In *Geotechnical Earthquake Engineering and Soil Dynamics V*. American Society of Civil Engineers. https://doi.org/10.1061/9780784481462.028

Ayoubi, P., Mohammadi, K., & Asimaki, D. (2020). A systematic analysis of basin effects on surface ground motion. *Soil Dynamics and Earthquake Engineering*. https://doi.org/10.1016/j.soildyn.2020.106490

Bijukchhen, S. M. (2018). *Construction of 3-D velocity structure model of Kathmandu Basin, Nepal, based on geological information and earthquake ground motion records* [Doctoral dissertation, Hokkaido University]. https://doi.org/10.14943/doctoral.k13350

Brocher, T. M. (2005). Empirical relations between elastic wavespeeds and density in the Earth's crust. *Bulletin of the Seismological Society of America, 95*(6), 2081–2092. https://doi.org/10.1785/0120050077

Chiou, S. B., Chang, Y. W., Jean, W. Y., & Chai, J. F. (2008). A study on the spectrum shape for performance based design of Taipei Basin. In *Proceedings of the 14th World Conference on Earthquake Engineering*. Beijing, China.

Elwood, K. J., Gerstenberger, M. C., Horspool, N., Hulsey, A., Jury, R., Wentz, R., Cubrinovski, M., Hare, J., Hooper, J. D., Philpott, A., & Sullivan, T. J. (2025). Overview of TS 1170.5:2025 and changes from NZS 1170.5:2004. *Bulletin of the New Zealand Society for Earthquake Engineering, 58*, 73–82. https://doi.org/10.5459/bnzsee.1695

Gupta, A. K. (1990). *Response spectrum method in seismic analysis and design of structures*. Blackwell Scientific Publications.

Hernández-Aguirre, V. M., & Rupakhety, R. (2024). Seismic response of the Kathmandu basin from 3D physics-based numerical simulations. In *Proceedings of the XVIII European Conference on Soil Mechanics and Geotechnical Engineering* (pp. 1655–1658).

Koketsu, K. (2024). *Velocity structures in and around Kathmandu Valley (2020–2024)*.

Pagliaroli, A., Aprile, V., Chamlagain, D., Lanzo, G., & Poovarodom, N. (2018). Assessment of site effects in the Kathmandu valley, Nepal, during the 2015 Mw 7.8 Gorkha earthquake sequence using 1D and 2D numerical modelling. *Engineering Geology, 239*, 50–62. https://doi.org/10.1016/j.enggeo.2018.03.011

Poudyal, D., Nordin, N., Roslan, S. N. A., & Dahal, B. K. (2024). Spatial mapping of the seismic vulnerability index in Kathmandu Valley: Insight from dominant frequency and amplification factor. *Journal of Geophysics and Engineering, 21*, 1272–1285. https://doi.org/10.1093/jge/gxae069

Sreejaya, K. P., Behera, S. N., & Raghukanth, S. T. G. (2025). Effect of basin geometry in seismic wave amplification. *Journal of Earth System Science, 134*, 166. https://doi.org/10.1007/s12040-025-02616-z

Takai, N., Shigefuji, M., Rajaure, S., Bijukchhen, S., Ichiyanagi, M., Dhital, M. R., & Sasatani, T. (2016). Strong ground motion in the Kathmandu Valley during the 2015 Gorkha, Nepal, earthquake. *Earth, Planets and Space, 68*. https://doi.org/10.1186/s40623-016-0383-7

Wei, S., Chen, M., Wang, X., Graves, R., Lindsey, E., Wang, T., Karakaş, Ç., & Helmberger, D. (2017). The 2015 Gorkha (Nepal) earthquake sequence: I. Source modeling and deterministic 3D ground shaking. *Tectonophysics*, *722*, 447–461. https://doi.org/10.1016/j.tecto.2017.11.024

MACHINE LEARNING BASED PREDICTION OF SUSPENDED SEDIMENT CONCENTRATION IN THE SETI GANDAKI RIVER, NEPAL WITH FEATURE ENGINEERING

Sameer Khatri[1], Ram Krishna Regmi[2*]

[1]Department of Civil Engineering, IOE, Pulchowk Campus, Tribhuvan University
Lalitpur, Nepal
080mshpe018.sameer@pcampus.edu.np
[*]Corresponding author: rkregmi@pcampus.edu.np

Abstract

The estimation of suspended sediment concentration (SSC) is crucial for evaluating reservoir sedimentation and managing catchment erosion, particularly in monsoon-dominated Himalayan rivers. This study investigates multiple machine learning models for predicting daily SSC in the Seti-Gandaki River at DHM Station 130.5, Tanahun, central-western Nepal. The 1,400 km² catchment lies within the Lesser and Middle Himalayan regions and has a mean annual discharge of 89.52 m³/s. Daily rainfall, discharge, and SSC records from 2004 to 2014 comprised 4,018 days; however, SSC observations were available for only 28.2% of the period, with 71.8% missing data. Recorded SSC ranged from 22 to 11,510 mg/L, exhibiting substantial variability and positive skewness. The traditional sediment rating curve ($SSC = 6.72 \times Q^{0.98}$) performed poorly, achieving an NSE of 0.205. In contrast, XGBoost delivered the best results, with validation and testing NSE values of 0.902 and 0.8791, respectively. LightGBM, Gradient Boosting, Random Forest, and Support Vector Regression performed less effectively. Feature importance and SHAP analyses highlighted discharge anomalies and rainfall-discharge interactions as influential predictors of SSC.

Keywords: Box-Cox transformation, Feature engineering, Machine learning algorithms, SHAP explainability, Suspended sediment concentration

1 Introduction

Nepal possesses substantial hydropower potential due to its Himalayan glaciers, monsoon rainfall, and steep topography. However, high suspended sediment concentrations (SSC) in Himalayan rivers cause reservoir sedimentation and turbine erosion, threatening hydropower infrastructure (Thapa et al., 2012). Continuous SSC monitoring is challenging because of remote catchments, high sampling costs, and dangerous monsoon flood conditions (Walling, 2006). Consequently, sediment datasets are often sparse, incomplete, and highly skewed, limiting reliable prediction.

Traditional sediment rating curves (SRCs), which relate discharge to SSC through a power-law relationship, are widely used but often perform poorly in Himalayan rivers because of nonlinear sediment dynamics and hysteresis (Gabet et al., 2008). Recent advances in machine learning (ML), particularly Random Forest, XGBoost, LightGBM, Gradient Boosting, and Support Vector Regression (SVR), offer promising alternatives for modelling complex hydrological relationships (Breiman, 2001; Chen & Guestrin, 2016). Explainable artificial intelligence techniques, such as SHAP, further improve model interpretability by identifying influential predictors. Which are the research questions may objectives of study can answer.

Nevertheless, SSC prediction under data-scarce conditions remains challenging due to temporal data leakage, inadequate feature engineering, and underprediction of extreme sediment events. Therefore, the specific objectives of the study are.

- To analyze seasonal SSC variability, evaluate traditional rating-curve performance, develop physically meaningful rainfall and discharge features.
- Compare five ML models using strict temporal splitting and multiple performance metrics.

and feature importance explained using SHAP analysis.

The findings may support more reliable sediment forecasting and sustainable hydropower management in Nepal.

2 Literature Review / Related Work

Collecting quality sediment data in Nepal is severely challenging because of remoteness, difficult mountain topography, inability of samplers to reach river depth during high currents, and systematic under-sampling of peak flood events (Durga Prasad Sangroula, 2009). Studies in Himalayan basins have shown that sediment rating curves often perform poorly due to strong hysteresis effects and rapidly changing sediment availability (Gabet et al., 2008). Studies have shown that including lagged discharge and rainfall significantly improves prediction accuracy (Kisi & Parmar, 2016). Unlike general machine learning applications, hydrological data exhibit strong temporal dependencies. Therefore, random data splitting can introduce data leakage, where future information is inadvertently used during model training (Bergmeir et al., 2018). Default parameters are rarely optimal, especially for complex environmental datasets. Techniques such as Grid Search and Randomized Search are commonly used for this purpose (Bergmeir et al., 2018; Bischl et al., 2023). Based on an extensive literature review of above 180 peer-reviewed papers, (Zounemat-Kermani & Kheimi, 2026) found out that SHAP is now the most widely used XAI technique in hydrology due to its methodological robustness and user-friendliness. Metrics Such as NSE, KGE, RMSE provide a comprehensive assessment of model accuracy, bias, and variability (Moriasi et al., 2007).

3 Materials and Methods

The data required and methodological workflow used in the study of the suspended sediment prediction is as follows.

3.1 Study Area

The study area is the Seti Gandaki Basin, which lies within Tanahun and Kaski Districts of Gandaki Province, Nepal. The basin spans approximately 1400 km², with elevations ranging from 340 masl in the Terai region to over 7700 masl in the Annapurna Himalaya area shown in Figure 1. The basin's climate is dominated by the South Asian summer monsoon, which runs from June to October and brings over 80% of the basin's total annual precipitation. The station operated by Nepal's Department of Hydrology and Meteorology, located in Damauli, has geographic coordinates of 84.265°E, 27.974°N. The basin records an average annual discharge of 89.52 m³/s, and a Thiessen polygon-weighted average annual rainfall of 2348 mm.

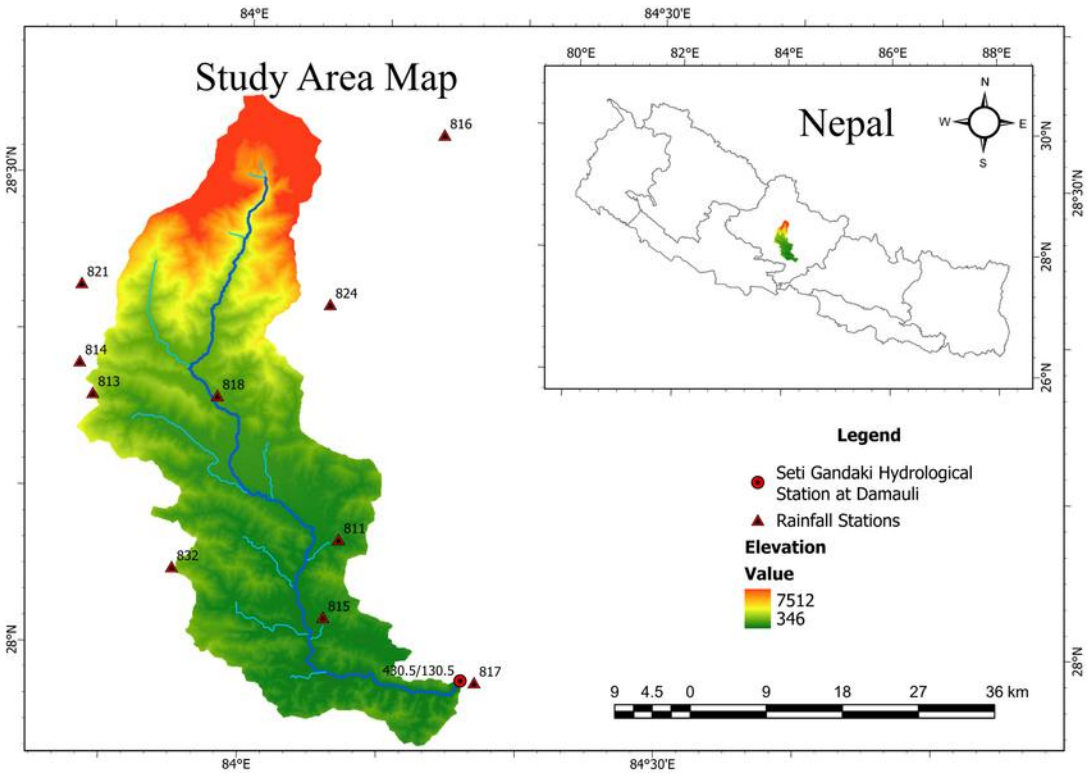


Figure 1: Study area map of Seti Gandaki at Damauli, hydrological station, Tanahun, Nepal

3.2 Data Collection

Daily hydrometeorological data for 2004 to 2014 was collected from DHM. Rainfall (mm/day) data was used of 10 sites inside and around the basin and if the data was missing a Normal Ratio Method was used to fill the gaps. River discharge (m^3/s) derived from a continuous series of stage data from Damauli station by DHM index no 430.5 listed in Table 1 and 2. Suspended sediment concentration (mg/l) obtained from Damauli sediment station from depths integrated manual samples from Damauli by DHM index no 130.5 listed in Table 3 was used. Areal rainfall was calculated using the Thiessen Polygon method. Basin delineation and catchment area was established using a 30m SRTM Digital Elevation Model utilizing ArcGIS version 10.3.

Table 1: Rainfall Stations of DHM used for rainfall data (Source DHM)

Index No	Station Name	District	Longitude	Latitude
811	Malepatan	Kaski	83.9742	28.21849
813	Bhadaure	Kaski	83.82212	28.265561
814	Lumle	Kaski	83.81791	28.29654
815	Kairinitar	Tanahun	84.0866	28.02696
816	Chane	Manang	84.23333	28.55
817	Damauli	Tanahun	84.26509	27.97368
818	Lamachaur	Kaski	83.96873	28.26168
821	Ghandruk	Kaski	83.8	28.38333
824	Siklesh	Kaski	84.10518	28.35806
832	Dandaswara	Syangja	83.92201	28.08492

Table 2: Discharge Station of DHM used for discharge data (Source DHM)

Index No	Station Name	District	Longitude	Latitude
430.5	Damauli	Tanahun	84.26509	27.97368

Table 3: Sediment measurement Station of DHM used for sediment data (Source DHM)

Index No	Station Name	District	Longitude	Latitude
130.5	Damauli	Tanahun	84.26509	27.97368

Figure 2 shows the overall Methodological workflow of the study to incorporate the objectives of study.

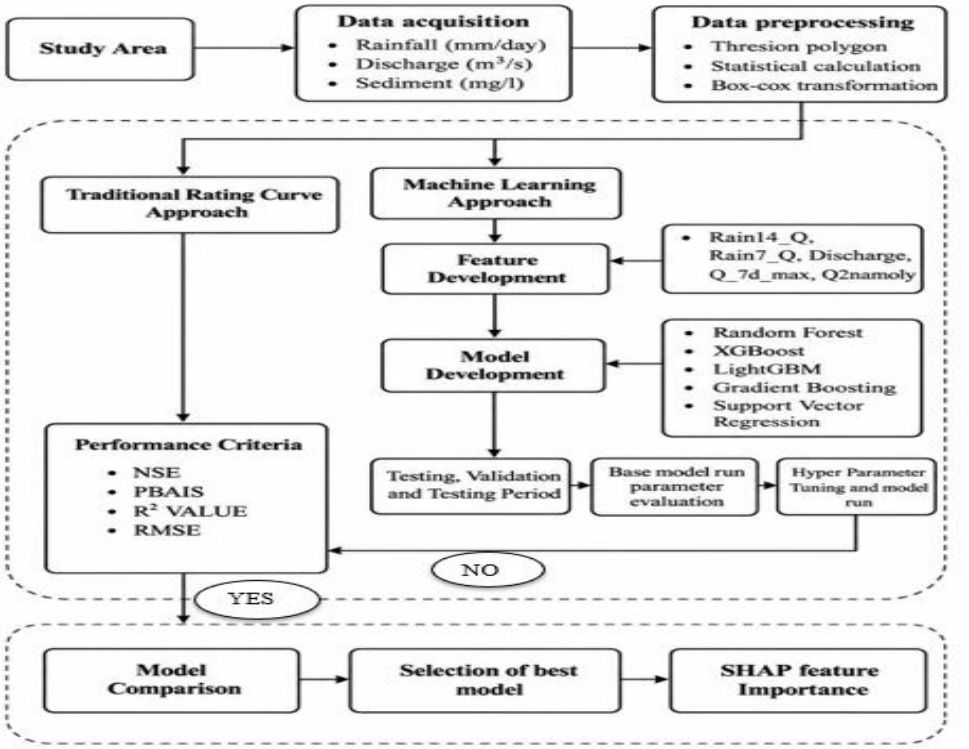


Figure 2: Methodological Framework for the Study

3.3 Sediment Rating Curve Baseline

A traditional power-law sediment rating curve ($SSC = aQ^b$) was fitted using ordinary least-squares regression in log-transformed space and evaluated on the validation set as a baseline.

3.4 Feature Engineering

From daily precipitation, discharge and SSC records, six physically informed feature groups were developed: (i) 1–7-day rainfall and discharge lags; (ii) 2–60-day cumulative rainfall and mean/maximum discharge statistics; (iii) rainfall–discharge interactions (e.g., 14-day rainfall × current discharge); (iv) daily and 3-day discharge changes to represent rising/falling-limb hysteresis; (v) flood (Q > Q75), extreme-flow (Q > Q90) and monsoon indicators; and (vi) log-transformed variables and a 30-day discharge anomaly. Calendar variables were excluded to reduce temporal leakage. Features with |Spearman's $\rho| \geq 0.10$ were retained, and SHAP values were used to interpret feature importance.

3.5 Transformation and Temporal Data Split

Because SSC was highly skewed, a Box–Cox transformation was applied, with $\lambda = 0.0032$ estimated using training data only; skewness decreased from 2.49 to 0.01. Data were split

chronologically into training (2004–2009; 527 observations, 46%), validation (2010–2011; 337, 30%) and independent testing (2012–2014; 270, 24%). The test set was reserved for final evaluation.

3.6 Machine-Learning Models and Tuning

Five regression algorithms were compared: Random Forest (500 trees), XGBoost (regularized gradient boosting), LightGBM (leaf-wise, histogram-based boosting), Gradient Boosting, and Support Vector Regression (SVR). Random Forest was tuned using GridSearchCV; the remaining models used RandomizedSearchCV. Five-fold TimeSeriesSplit cross-validation was applied to limit temporal leakage.

3.7 Performance Metrics

Performance was assessed using Nash–Sutcliffe Efficiency (NSE), coefficient of determination (R^2), root mean square error (RMSE), mean absolute error (MAE), and percentage bias (PBIAS). Following (Moriasi et al., 2007), NSE > 0.75 was classified as very good; 0.65–0.75 as good; 0.50–0.65 as satisfactory; and ≤ 0.50 as unsatisfactory

4 Results and Discussion

The results obtained to fulfill the objectives of the study are discussed hereunder.

4.1 Data Characteristics and Rating-Curve Performance

The dataset contained 4,018 daily records of rainfall, discharge, and suspended sediment concentration (SSC). Rainfall and discharge were complete, whereas SSC was available for 1,134 days (28.2%); the remaining 71.8% were unobserved which is shown in Figure 3. Observed SSC ranged from 22 to 11,510 mg/L, with a mean of 1,295 mg/L and a median of 536 mg/L can be seen in Table 4, indicating a strongly right-skewed distribution. Mean monsoon SSC (1,852 mg/L) was approximately 5.7 times the dry-season mean (324 mg/L), reflecting increased sediment mobilisation during high-flow periods. Discharge had a strong positive Spearman correlation with SSC ($\rho = 0.717$), while rainfall had a moderate correlation ($\rho = 0.459$). This suggests that discharge is the more immediate control on sediment transport, while rainfall contributes to sediment availability (Asselman, 2000) . Description also shows the need of study of SSC especially in Himalayan catchment need to be taken more seriously.

Table 4: Statistics of the observed datasets

Statistics	Rainfall (mm)	Discharge (m^3/s)	SSC (mg/l)
Mean	6.43	89.52	1295.01
Meadian	0	35.4	536
Std	15.39	107.77	1826.89
Min	0	11.7	22
max	182.36	1030	11510

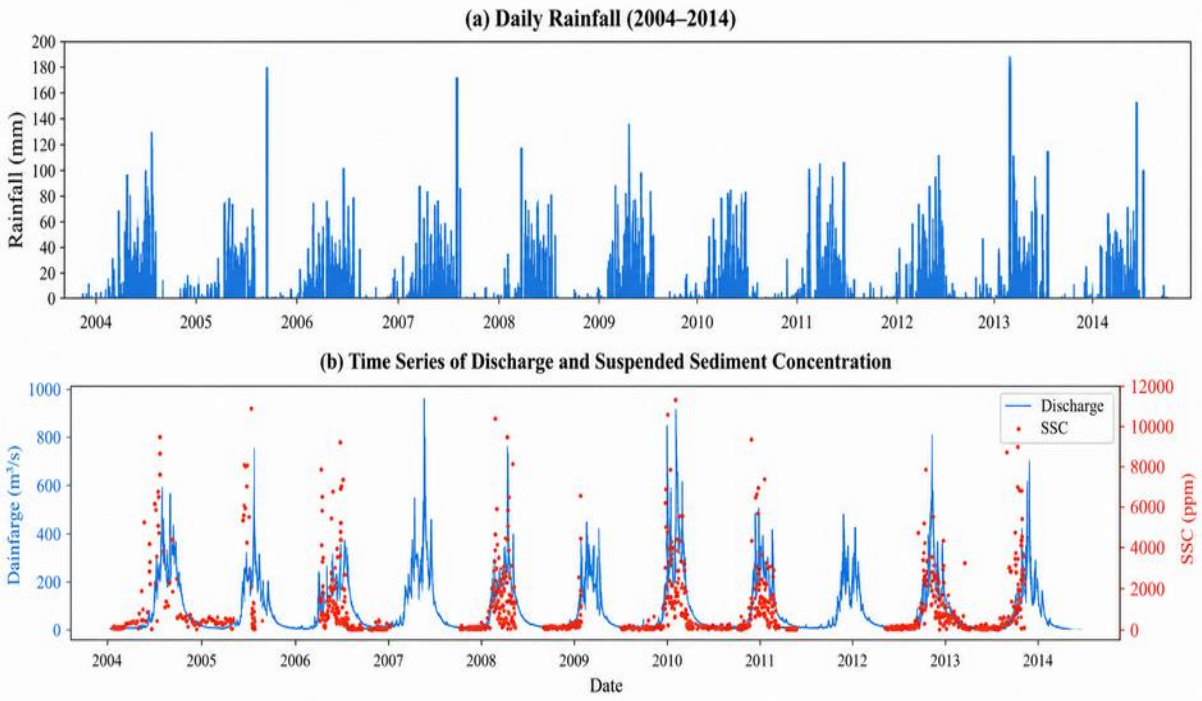


Figure 3: Time series plot of rainfall, discharge and SSC data obtained from DHM

The conventional sediment rating curve, SSC = 6.72 × Q^0.98, achieved an NSE of only 0.205. visualized in Figure 4. Its limited performance indicates that a single discharge–sediment relationship does not adequately represent variability caused by antecedent conditions, sediment supply, and hysteresis. The rating curve was therefore retained as a baseline against which the machine-learning models were compared.

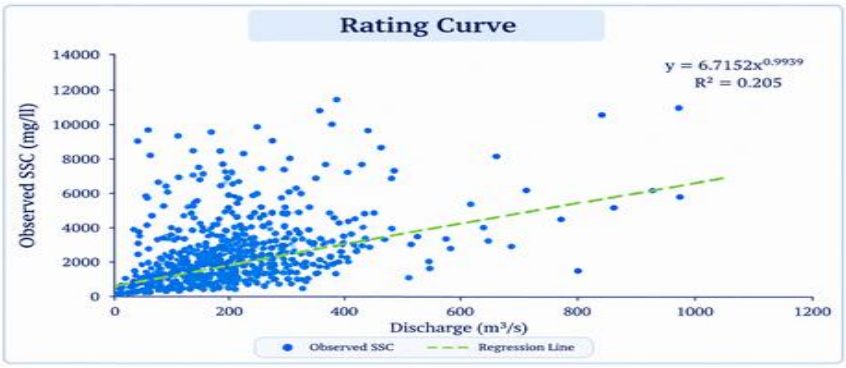


Figure 4: Rating curve obtained from observed DHM data

4.2 Feature Engineering and Data Preparation

A set of 52 hydrologically meaningful predictors was developed from rainfall and discharge. These included 1–7-day lag values, rolling rainfall accumulations and discharge statistics over multiple windows, rainfall–discharge interaction terms, discharge change rates, flood and monsoon indicators, and anomaly and logarithmic features. Calendar variables were excluded to reduce the risk of temporal leakage. The strongest initial correlations included 14-day rainfall accumulation multiplied by discharge (rain14_Q; |ρ| = 0.755) and the corresponding 7-day interaction (rain7_Q; |ρ| = 0.747) shown in Figure 5.



Figure 5: The categorization of Features and top spearman features

Observed SSC was positively skewed (skewness = 2.49). A Box–Cox transformation with λ = 0.0032, approximately equivalent to a logarithmic transformation, reduced skewness to −0.01. The transformation parameter was estimated from the training data and then applied to the later periods. A chronological split was used: 2004–2009 for training (527 SSC observations), 2010–2011 for validation (337), and 2012–2014 for independent testing (270). This time-ordered design helped limit information leakage between model development and evaluation.

4.3 Model Performance During Training Phase Tuning Phase and Testing Phase

Five algorithms were evaluated: Random Forest (RF), XGBoost (XGB), LightGBM (LGB), Gradient Boosting (GB), and Support Vector Regression (SVR). Before tuning, LightGBM performed best (NSE = 0.413), followed by XGBoost (0.326) and Random Forest (0.324). SVR performed poorly (NSE = −0.257), while the rating curve achieved NSE = 0.205. The weak discharge-only baselines also indicated that discharge alone was insufficient to explain SSC variability.

Hyperparameter optimisation using time-series cross-validation improved the tree-based models parameters listed in Table 5. XGBoost showed the strongest improvement, increasing from NSE = 0.326 to 0.902; LightGBM increased from 0.413 to 0.817, Gradient Boosting from 0.245 to 0.703, and Random Forest from 0.324 to 0.634. SVR improved to NSE = 0.159 but remained the weakest model. On the validation set, the tuned XGBoost model had NSE = 0.9019, RMSE = 543.7 mg/L, and PBIAS = 9.09%, indicating strong agreement overall with a modest tendency to underpredict SSC.

Table 5: Hyperparameters tuning parameters used in the study

Model	Tuning Method	Hyperparameter Grid	Iterations
RF	GridSearchCV	n_estimators:[300,600]; max_depth:[8,None]; min_samples_leaf:[1,3]; max_features: [sqrt]	16
XGB	RandomizedSearchCV	n_estimators:[300,500]; learning_rate: [0.03,0.05,0.1]; max_depth: [4, 6]; subsample: [0.7, 0.9]; colsample_bytree: [0.7, 0.9]; reg_alpha: [0, 0.1]; reg_lambda: [1, 2]	20
LGB	RandomizedSearchCV	n_estimators:[300,500]; learning_rate: [0.03,0.05,0.1]; max_depth: [4, 6, −1]; num_leaves: [31, 63]; subsample: [0.7, 0.9]; colsample_bytree:[0.7,0.9]; reg_alpha:[0,0.1];	20

Model	Tuning Method	Hyperparameter Grid	Iterations
		min_child_samples: [10, 20]	
GB	RandomizedSearchCV	n_estimators:[200,400]; learning_rate: [0.05,0.1]; max_depth: [3, 5]; subsample: [0.7, 0.9]; min_samples_leaf: [1, 3]	15
SVR	RandomizedSearchCV	C: [10, 100, 500]; gamma: [scale, 0.01, 0.1]; epsilon: [0.05, 0.1, 0.2]	15

On the held-out 2012–2014 test period, XGBoost achieved NSE = 0.8791, only 0.023 lower than its validation NSE, suggesting that its performance transferred well to unseen observations. LightGBM also generalised reasonably well (test NSE = 0.746), followed by Gradient Boosting (0.571). SVR showed a substantial train–test performance gap (training NSE = 0.941; test NSE = 0.116), indicating likely overfitting and weak generalization which can be seen in Figure 6. Overall, XGBoost provided the best balance of accuracy and stability among the evaluated models and improved markedly on the conventional rating curve shown in Figure 7.

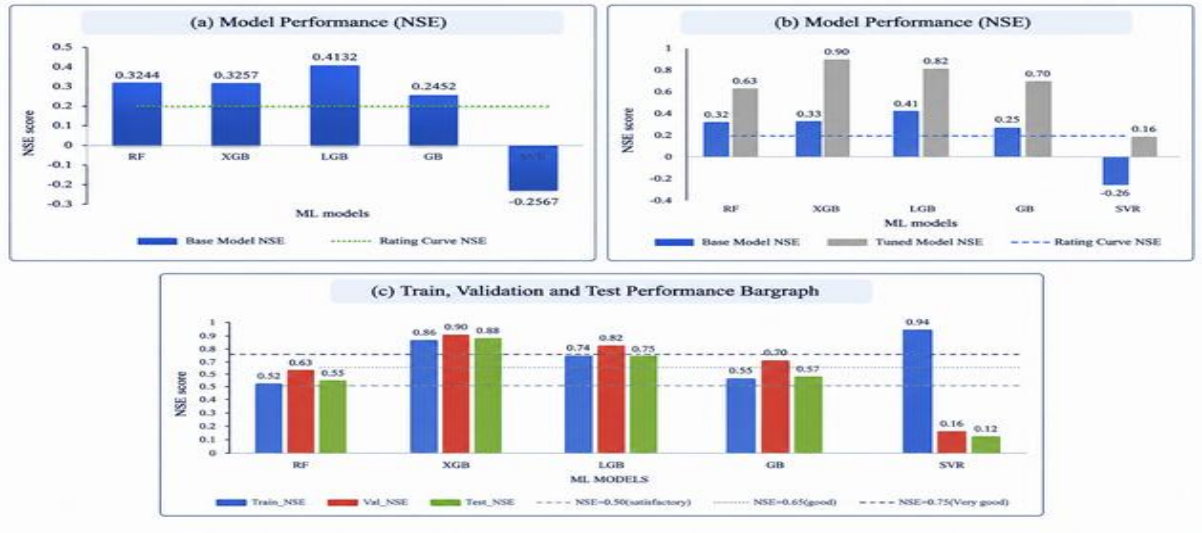


Figure 6: The performance of the ml algorithms in base case, tuned case and comparative bar graph showing training, validation and testing phase.



Figure 7: Comparison of plot during training/validation phase and testing phase by best model

4.4 Feature Importance and Hydrological Interpretation

Feature-importance methods supported the role of antecedent rainfall and changing flow conditions. Gini importance ranked discharge anomaly (Q_anomaly) highest, whereas

permutation importance ranked rain14_Q first. SHAP analysis identified rain14_Q (mean |SHAP| = 0.151), rain7_Q (0.108), and the antecedent precipitation index (API; 0.091) as the leading predictors. For a high-SSC flood observation (10,806 mg/L), Q_anomaly, rain14_Q, and rain7_Q made the largest positive contributions to the prediction shown in graphical picture in Figure 8. These results suggest that sediment concentration depends not only on current discharge but also on antecedent rainfall accumulation and departures from typical flow conditions.

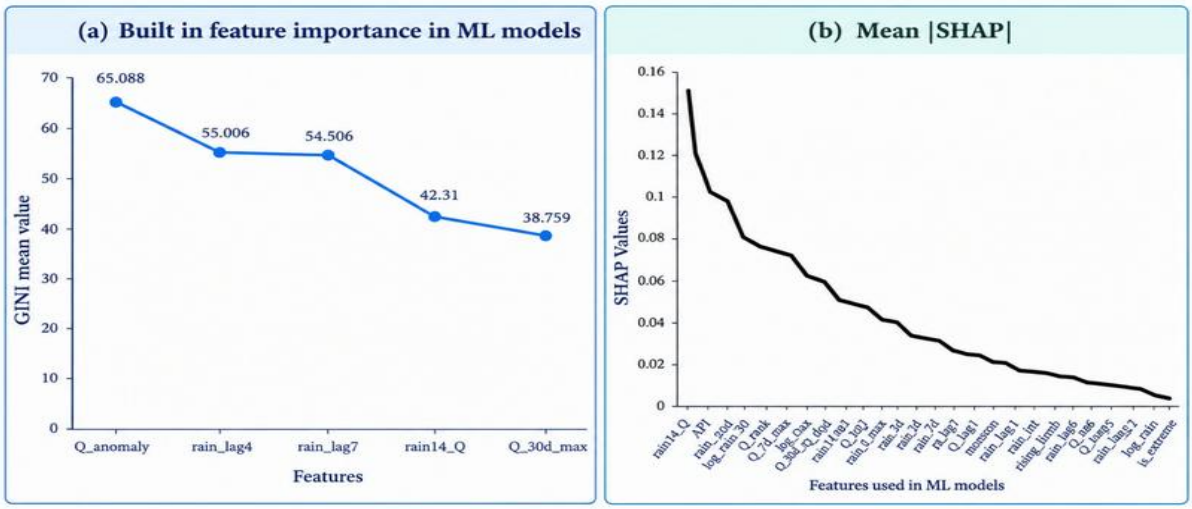


Figure 8: Feature which drives the SSC in the catchment explained by built in and SHAP.

Taken together, the results identify tuned XGBoost as the most promising model for estimating SSC and predicted and observed time series is obtained in Figure 9 from the available rainfall and discharge records. Its test performance and physically interpretable predictors support its use for sediment estimation where SSC observations are sparse. However, the large proportion of missing SSC measurements and the limited period used for independent testing should be considered when applying the model to other periods or locations. Further validation with additional sediment observations would strengthen confidence in its operational use.

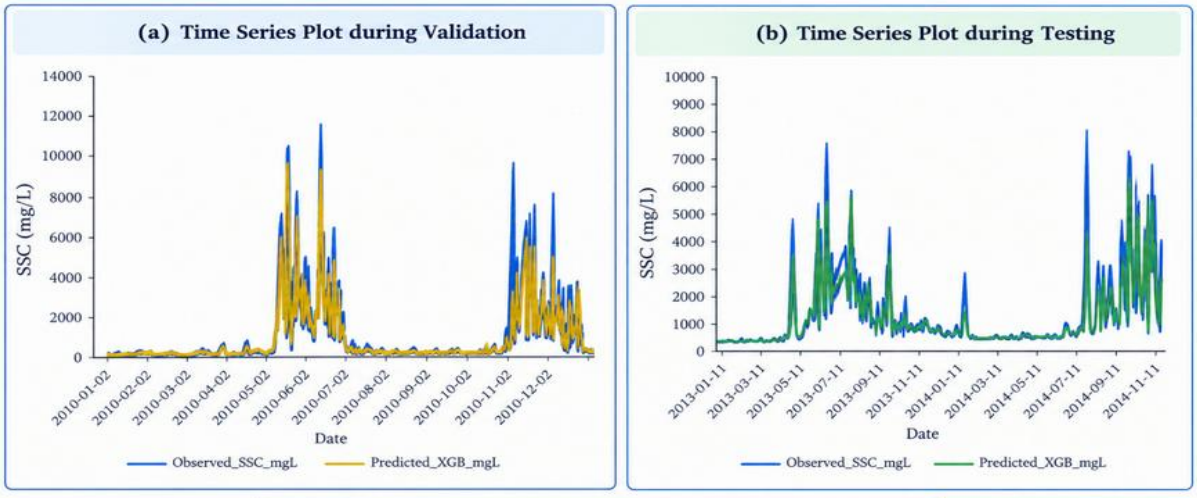


Figure 9: Time series plot of observed vs predicted during validation period and testing period.

5 Limitations

- The model uses only point-scale rainfall and discharge observations as inputs.
- Important spatial drivers of SSC variability including land use change, forest cover and agricultural practices on hillslopes across the catchment are not represented.
- Physically-based sediment transport modelling, deep learning approaches (LSTM, CNN) are not used due to lack of large datasets.

6 Conclusion

- The traditional sediment rating curve (NSE = 0.205) is inadequate for SSC prediction in the Seti-Gandaki River, confirming the need for advanced data-driven approaches that can capture nonlinear dynamics, and antecedent moisture effects.
- Physically informed feature engineering involves features in six classes, exclusion of calendar variables and outperforms the simple regression baselines, with performance, on truly never seen datasets.
- The strict three-way temporal split, and use of TimeSeriesSplit cross-validation is integral in the assessment of unbiased performance in the hydrological time series. The modest drop (0.023 NSE for XGBoost performance from validation to test, provide best generalization.
- It brings the physical interpretation of the top three predictor rain14_Q, antecedent precipitation index, and Q_anomaly, which is indicated by SHAP analysis.

7 Acknowledgments

The author sincerely thanks Asst. Prof. Dr. Ram Krishna Regmi (Head, Department of Civil Engineering, Pulchowk Campus) for invaluable guidance, encouragement, and supervision throughout this work. The Department of Hydrology and Meteorology (DHM), Nepal, is acknowledged for providing the hydrometeorological data used in this study.

8 Funding

The author(s) received no financial support for the research, authorship, or publication of this paper.

9 Conflict of Interest

The author(s) declare no conflict of interest.

10 Author Contributions

Conceptualization, S.K. and R.K.R.; methodology, S.K.; validation, R.K.R, resources, R.K.R; writing: original draft preparation, S.K.; writing: review and editing, S.K. and R.K.R; supervision, R.K.R.

11 Data Availability

Data in research is used which can be obtained from DHM upon request and code of the research can be obtained under Author permission.

12 References

Asselman, N. E. M. (2000). Fitting and interpretation of sediment rating curves. *Journal of Hydrology*, *234*(3), 228–248. https://doi.org/https://doi.org/10.1016/S0022-1694(00)00253-5

Bergmeir, C., Hyndman, R. J., & Koo, B. (2018). A note on the validity of cross-validation for evaluating autoregressive time series prediction. *Computational Statistics & Data Analysis*, *120*, 70–83. https://doi.org/https://doi.org/10.1016/j.csda.2017.11.003

Bischl, B., Binder, M., Lang, M., Pielok, T., Richter, J., Coors, S., Thomas, J., Ullmann, T., Becker, M., Boulesteix, A. L., Deng, D., & Lindauer, M. (2023). Hyperparameter optimization: Foundations, algorithms, best practices, and open challenges. In *Wiley Interdisciplinary Reviews: Data Mining and Knowledge Discovery* (Vol. 13, Number 2). John Wiley and Sons Inc. https://doi.org/10.1002/widm.1484

Breiman, L. (2001). Random forests. *Machine Learning*, *45*(1), 5–32. https://doi.org/10.1023/A:1010933404324/METRICS

Chen, T., & Guestrin, C. (2016). XGBoost: A scalable tree boosting system. *Proceedings of the ACM SIGKDD International Conference on Knowledge Discovery and Data Mining*, *13-17-August-2016*, 785–794. https://doi.org/10.1145/2939672.2939785

Durga Prasad Sangroula. (2009). Hydropower Development and Its Sustainability with Respect to Sedimentation in Nepal. *Journal of the Institute of Engineering*, *7*(1), 56–64. https://doi.org/10.3126/JIE.V7I1.2063

Gabet, E. J., Burbank, D. W., Pratt-Sitaula, B., Putkonen, J., & Bookhagen, B. (2008). Modern erosion rates in the High Himalayas of Nepal. *Earth and Planetary Science Letters*, *267*(3–4), 482–494. https://doi.org/10.1016/J.EPSL.2007.11.059

Kisi, O., & Parmar, K. S. (2016). Application of least square support vector machine and multivariate adaptive regression spline models in long term prediction of river water pollution. *Journal of Hydrology*, *534*, 104–112. https://doi.org/https://doi.org/10.1016/j.jhydrol.2015.12.014

Moriasi, D. N., Arnold, J. G., Liew, M. W. Van, Bingner, R. L., Harmel, R. D., & Veith, T. L. (2007). Model Evaluation Guidelines for Systematic Quantification of Accuracy in Watershed Simulations. *Transactions of the ASABE*, *50*(3), 885–900. https://doi.org/10.13031/2013.23153

Thapa, B., Shrestha, R., Dhakal, P., & Singh Thapa, B. (2012). *Sediment in Nepalese hydropower projects*.

Walling, D. E. (2006). Human impact on land-ocean sediment transfer by the world's rivers. *Geomorphology*, *79*(3–4), 192–216. https://doi.org/10.1016/j.geomorph.2006.06.019

Zounemat-Kermani, M., & Kheimi, M. (2026). Explainable Artificial Intelligence in Hydrology: A Review. *Water Resources Management 2026 40:3*, *40*(3), 106-. https://doi.org/10.1007/S11269-025-04435-9

Simulation of Concrete Arch Dam-Breach Floods and Downstream Flood Propagation Using Integrated HEC-HMS and HEC-RAS Modelling: The Budhi Gandaki Case Study

Prabin Karn[1], Prinesh Maharjan[2]

[1]Department of Civil Engineering, Pulchowk Campus, Institute of Engineering, Tribhuvan University, Lalitpur, Nepal

[2]Department of Civil Engineering, Khwopa Engineering College, Purbanchal University, Bhaktapur, Nepal

080mshpe012.prabin@pcampus.edu.np

Corresponding author: Prabin Karn, 080mshpe012.prabin@pcampus.edu.np

Abstract

Large storage dams are designed against the probable maximum flood (PMF), but the flood released by a failure can be far larger than any inflow. This study links a HEC-HMS rainfall-runoff model with a two-dimensional HEC-RAS model to estimate the PMF and to simulate hypothetical overtopping breaches of the proposed Budhi Gandaki concrete arch dam in Nepal. The semi-distributed HEC-HMS model of the 4,996 km² catchment was calibrated (1995-2010) and validated (2011-2019) against daily discharge at Arughat, giving Nash-Sutcliffe efficiencies (NSE) of 0.711 and 0.557. Forced with probable maximum precipitation (PMP) from the Hershfield method, the model gave a PMF peak of 11,590.8 m³/s at the dam site, about 18% above the design flood of 9,809 m³/s. Two breach scenarios, a Base Case and a Worst Case, produced peak outflows of 360,456 and 468,631 m³/s, which are 31 and 40 times the PMF. At Meghauli, 100 km downstream, the peaks fell to 84,889 and 114,590 m³/s, about 76% below the breach peaks, and arrived about 9.5 hours after breach initiation. Because the breach outflow exceeded the PMF inflow by more than an order of magnitude, the size of the flood was set by reservoir storage and breach geometry and not by the inflow. The breach parameters are prescribed and not derived from structural analysis, so the results are conditional scenario estimates.

Keywords: probable maximum flood, dam-breach modelling, HEC-HMS, HEC-RAS, concrete arch dam

Introduction

Large dams supply hydropower, water storage, irrigation and flood control, but the water they hold becomes a hazard to downstream communities if the structure fails. A breach can empty a reservoir in minutes to hours and send a flood wave through the valley below. The resulting hazard depends on the stored volume, the initial water level, the size and formation time of the breach, and the geometry and roughness of the downstream channel (Costa, 1985).

Dam-break analysis is therefore a standard part of dam-safety assessment and emergency planning. A numerical model estimates the outflow hydrograph through an assumed breach and routes it downstream, giving discharge, water level, depth, velocity and arrival time. These quantities show which reaches are most exposed and how much time is available for warning.

Concrete arch dams are harder to treat than embankment dams. An arch passes most of the water load to its abutments, so its response depends on arch geometry, foundation and abutment conditions, and rock-mass quality. Breach relationships fitted to embankment failures cannot

simply be carried over to arch dams (Fang et al., 2017; Altarejos-García et al., 2015). Where no structural failure analysis exists, hypothetical breach scenarios can still show the hydraulic consequences of a stated assumption, provided they are read as scenarios and not as predictions.

The proposed Budhi Gandaki Hydroelectric Project in central Nepal includes a double-curvature concrete arch dam about 263 m high, with a full supply level (FSL) of 540 m above sea level (masl) and a gross storage of about 4,467 million m³ (BGHPP Development Committee, 2015). A reservoir of this size makes it important to understand how extreme catchment inflow, reservoir condition and breach outflow are related. The catchment extends from high mountain terrain, partly in Tibet, to the valleys of central Nepal. Monsoon rainfall is the main source of runoff, snow and ice melt contribute in the upper basin, and the sparse rainfall network makes the spatial pattern of storms difficult to define.

The safety of large dams is commonly checked against the probable maximum flood (PMF), the flood that follows from the most severe combination of meteorological and hydrological conditions considered reasonably possible. The PMF is derived from probable maximum precipitation (PMP), the upper limit of rainfall for a given area and duration (Hershfield, 1965). It has no return period, so it is not directly comparable with floods obtained from frequency analysis.

Two earlier studies bear directly on this dam. Khatri et al. (2018) simulated streamflow in the Budhi Gandaki catchment with HEC-HMS and a snowmelt runoff model, and Awal et al. (2024) simulated breach floods for the dam with HEC-RAS 2D for scenarios with and without a PMF, together with a sensitivity analysis of the breach parameters. In the present study the PMF is derived from a HEC-HMS model that is calibrated and validated against observed discharge. This matters because a model that reproduces ordinary flows is not automatically reliable under PMP-level rainfall: calibration and validation support its performance within the observed range, whereas extrapolation to extreme rainfall remains uncertain.

The study estimates the PMF of the Budhi Gandaki catchment and examines the downstream consequences of a hypothetical failure of the proposed arch dam. The specific objectives are (1) to build and validate a HEC-HMS rainfall-runoff model and use it to estimate the PMF, and (2) to simulate breach outflow and flood propagation with a two-dimensional HEC-RAS model. The study evaluates model performance, estimates the probable maximum flood (PMF) under probable maximum precipitation (PMP), compares dam-breach scenarios with the PMF and design flood, and examines flood characteristics along the downstream river reach.

Literature Review

The PMF is usually obtained by deriving a PMP storm and converting it to runoff with a rainfall-runoff model. Hershfield (1965) estimated PMP statistically from the mean and standard deviation of annual-maximum rainfall multiplied by an enveloping frequency factor. The result is sensitive to record length, the rainfall duration analyzed, the observation interval and the adjustments applied to the largest observed event, as described in the World Meteorological Organization manual (WMO, 2009) and reviewed by Sarkar and Maity (2020). HEC-HMS offers several methods for losses, runoff transform, baseflow and channel routing (U.S. Army Corps of Engineers, Hydrologic Engineering Center [USACE-HEC], 2024). The combination of SCS Curve Number loss, SCS unit hydrograph and Muskingum routing used here is common in catchment studies, but its performance depends on how the basin is subdivided, on data quality

and on the time step of the records. Moriasi et al. (2007) recommend judging a watershed model with several measures, including the Nash-Sutcliffe efficiency (NSE) and percent bias (PBIAS), because a single score can hide seasonal or year-to-year errors. This matters in the Budhi Gandaki basin, where both monsoon rain and snow and ice melt feed the river. Khatri et al. (2018) reported an NSE of about 0.78 for HEC-HMS in the same basin.

A dam-break study couples a breach description with a hydraulic model that routes the released water. HEC-RAS can model unsteady flow in two dimensions and returns discharge, water level, depth, velocity and arrival time, but the quality of these results depends on the terrain and channel representation, the boundary conditions, the roughness and the breach assumptions (USACE-HEC, 2021). Dam-break models are usually checked against recorded failures and laboratory tests, yet full-scale observations are scarce and laboratory cases cannot reproduce real terrain (Aureli et al., 2021). Simulated depths, velocities and arrival times are therefore only as reliable as the data and assumptions behind them.

Breach parameters are especially uncertain for concrete arch dams, for which few failures are documented. Fang et al. (2017) proposed a way of quantifying breach size for these dams, and the Federal Energy Regulatory Commission (FERC, 1993) gives guidance on dam-break studies. Empirical equations such as that of Froehlich (1995) were fitted to embankment failures and should not be applied to arch dams without checking. Overtopping is among the commonly recorded causes of dam failure (Costa, 1985; International Commission on Large Dams [ICOLD], 1995), but concrete dams more often fail through foundation or dam-foundation contact problems (Altarejos-García et al., 2015; ICOLD, 1995). Scenario analysis with prescribed breach parameters is a practical choice when a structural analysis is not available, although changing several parameters together does not show the effect of any single one.

In Nepal, hydraulic models have been applied to the 2015 Kali Gandaki landslide-dam breach (Bricker et al., 2017), to a potential breach of the Kulekhani rockfill dam (Pandey et al., 2024) and to the proposed Budhi Gandaki dam (Awal et al., 2024), who examined scenarios with and without a PMF and the sensitivity of flood magnitude to the breach parameters. Linked HEC-HMS and HEC-RAS workflows have been used elsewhere, for example by Athira et al. (2023) on the Meenachil River and by Manandhar et al. (2024) for Mahadev Khola, Bhaktapur. The present study adds a PMF derived from a rainfall-runoff model tested against observed discharge, used as reservoir inflow for two breach scenarios, with discharge, timing, depth and velocity reported along 119 km of the river. It does not claim that the prescribed breach parameters reproduce the failure of an arch dam.

Materials and Methods

Study Area and Data

The Budhi Gandaki is a transboundary river. The catchment above the proposed dam covers about 4,996 km², and part of the upper basin lies in Tibet, China. Flow follows a strong monsoon pattern, and snow and ice melt add to the discharge in the north (Khatri et al., 2018). The project is planned as a 1,200 MW storage scheme with a double-curvature concrete arch dam 263 m high, a crest 760 m long and 10 m wide at 542 masl, an FSL of 540 masl and a gross storage of about 4,467 million m³ (BGHPP Development Committee, 2015). The hydraulic study follows the Budhi Gandaki and Trishuli rivers from the dam to Meghauli, about 100 km downstream, and the model domain continues to about 119 km (Figure 1).

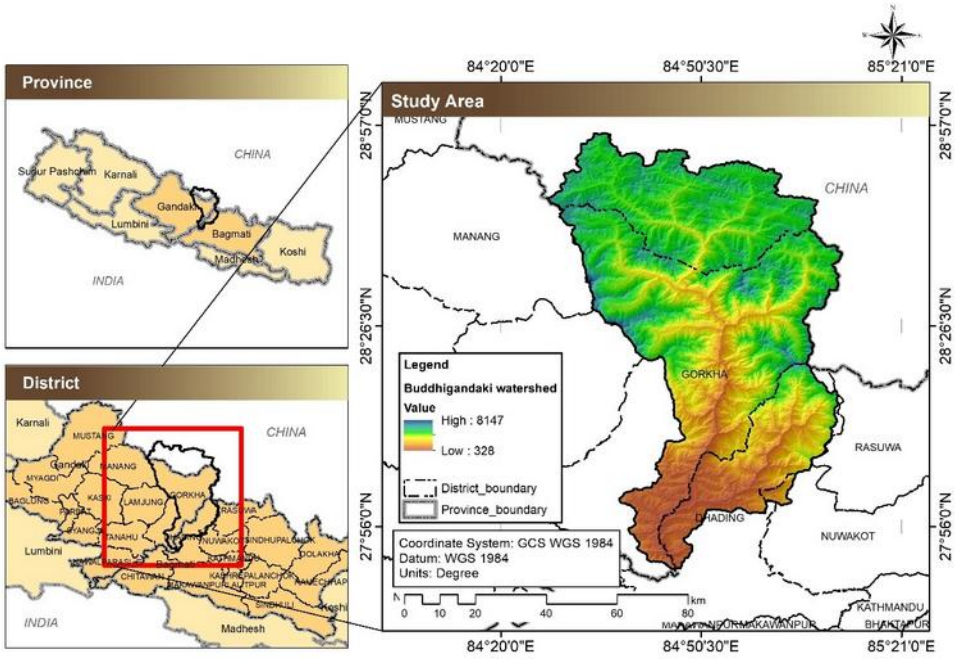


Figure 1

Location of the Budhi Gandaki dam, the catchment and the downstream study reach

Daily rainfall for 1980-2019 was obtained from six stations of the Department of Hydrology and Meteorology (DHM): Larke Samdo, Jagat/Setibas, Arughat, Gorkha, Dhading and Pansayakhola. Daily discharge for 1995-2019 at Arughat came from DHM and project records. A 30 m Shuttle Radar Topography Mission (SRTM) digital elevation model (DEM) was used for catchment delineation and as the hydraulic terrain (Earth Resources Observation and Science Center, 2019). The 2022 national land-cover dataset (Forest Research and Training Centre [FRTC], 2022) supported curve-number and roughness assignment, and dam and reservoir information were taken from the final detailed design report (BGHPP Development Committee, 2015). The data sets are summarised in Table 1.

Table 1

Data sets used in the study and their sources

Dataset	Description / period	Use in the study
Rainfall	Daily records, 1980-2019; six DHM stations	HEC-HMS forcing and PMP estimation
Discharge	Daily observed flow, 1995-2019, Arughat (DHM and project records)	Calibration and independent validation
Terrain	SRTM 1 arc-second, approximately 30 m	Catchment delineation and HEC-RAS terrain
Land cover	National land-cover dataset, 2022 (FRTC, 2022)	Curve-number and Manning's n assignment
Dam and reservoir design	Final detailed design report (BGHPP Development Committee, 2015)	Storage curve, dam geometry, design flood and spillway capacity

Note. DHM = Department of Hydrology and Meteorology; SRTM = Shuttle Radar Topography Mission; PMP = probable maximum precipitation.

Figure 2 presents the overall methodological framework, from data preparation and hydrological modelling to PMF estimation, two-dimensional dam-breach simulation, and analysis of downstream flood characteristics.

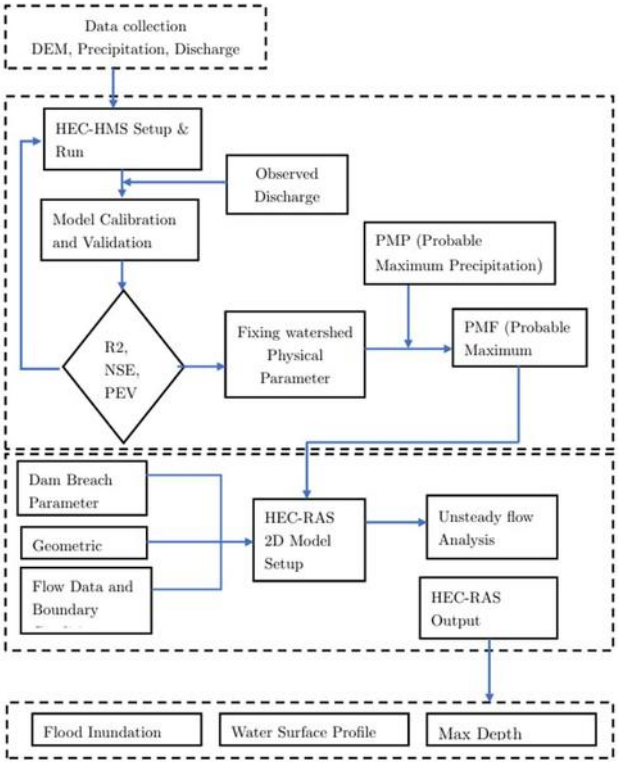


Figure 2

Methodological framework of the study

HEC-HMS Rainfall-Runoff Model

The catchment was modelled in HEC-HMS (Hydrologic Modeling System) version 4.13 (USACE-HEC, 2024). The SRTM terrain was processed in a geographic information system (sink filling, flow direction, flow accumulation and stream extraction) and transferred to HEC-HMS with HEC-GeoHMS. The basin was divided into 11 sub-basins with a combined area of 4,996.3 km², following relief, drainage junctions, the river network and rainfall-station locations. The outlet was placed at the dam site so that the computed hydrograph could be passed directly to the hydraulic model. Rainfall over each sub-basin was obtained from the six stations by Thiessen polygon weighting.

Losses were computed with the SCS Curve Number method, with curve numbers assigned from land cover and soil. Direct runoff was transformed with the SCS unit hydrograph, using basin lag as an adjustable parameter, and baseflow followed an exponential recession. Simple canopy and surface storages were included. Reach routing used the Muskingum method (Equation 1), in which S is channel storage, K the storage constant, X a weighting factor between 0 and 0.5, I inflow and O outflow. All simulations used a daily time step to match the rainfall and discharge records.

(1)

The discharge record was split into a calibration period (1995-2010) and an independent validation period (2011-2019). During calibration, loss, transform, baseflow and routing parameters were adjusted against the observed hydrograph within physically reasonable ranges, and the calibrated set was then held fixed for validation. Agreement was measured with the coefficient of determination (R^2), NSE (Equation 2) and PBIAS (Equation 3):

(2)

(3)

where $Q_{obs,i}$ and $Q_{sim,i}$ are observed and simulated discharge on day i, $\bar{Q}_{obs}$ is the mean observed discharge and n is the number of days. With this definition a negative PBIAS means that total volume is overestimated. Performance was rated with the criteria of Moriasi et al. (2007), which were proposed for monthly simulations and are used here only as an indicative guide for daily data: NSE above 0.75, 0.65-0.75 and 0.50-0.65 is rated very good, good and satisfactory, and absolute PBIAS below 10%, 10-15% and 15-25% is rated the same way.

PMP and PMF Estimation

PMP was estimated with the statistical method of Hershfield (1965), applied as described by WMO (2009) and Sarkar and Maity (2020). In its basic form the PMP depth is the mean of the annual-maximum rainfall series plus a multiple of its standard deviation (Equation 4), where $\bar{X}_n$ and S_n are the mean and standard deviation of the annual maxima and K_m is the frequency factor.

(4)

Annual-maximum 1-day and 3-day rainfall series were extracted from the 40-year record at each of the six stations. A frequency factor $K_m = 15$ was adopted as the envelope value, and the WMO adjustments for the maximum observed event, record length and fixed observation interval were applied; the last used a factor of 1.13 to convert fixed daily observations to a 24-hour depth. Station values were distributed to the 11 sub-basins by Thiessen weighting. A five-day storm was built around the three-day PMP event, wet antecedent conditions (AMC III) were assumed for the curve numbers, and the resulting hyetographs were applied to the calibrated model with no change to any calibrated parameter. The peak discharge at the dam-site outlet was taken as the PMF and used as the reservoir inflow in the HEC-RAS simulations.

HEC-RAS Dam-Break Model

The hypothetical breach and downstream flood were simulated in HEC-RAS version 7.0.1 with 2D unsteady flow in the WGS 1984 UTM Zone 45N coordinate system. The reservoir was represented as a storage area joined to the 2D flow area by a storage-area-to-2D connection that stands for the dam. The full shallow-water equations were solved, because the diffusion-wave form is not suited to a wave of this speed and size. The 2D flow area follows the Budhi Gandaki and Trishuli rivers and was meshed with 100 m × 100 m cells (579,087 cells), which is coarser than the nominal 30 m resolution of the SRTM terrain. Because the volume derived from the terrain alone was smaller than the design storage, the elevation-volume curve from the design report was entered directly, so that the reservoir holds 4,467 million m^3 at 540 masl. The dam was entered with a crest length of 760 m, a crest width of 10 m and a crest elevation of 542 masl. The gated spillway (about 7,400 m^3/s at FSL) was not modelled as a separate outlet, because its discharge is small compared with a full breach and gate-operation rules were not available.

Manning's roughness was assigned by land-cover class following Chow (1959), from 0.03 for bare soil to 0.14 for built-up areas, with 0.12 for forest and 0.08 for the riverbed. Failure was assumed to occur by overtopping with a sinusoidal breach progression. Documented failures of concrete arch dams are almost absent, so the breach parameters were chosen from guideline ranges (FERC, 1993; USACE-HEC, 2021) for two scenarios (Table 2). The Base Case uses a breach width of 608 m (0.8 of the crest length), a breach bottom at 460 masl, a formation time of 0.10 h and a weir coefficient of 3.1. The Worst Case uses the full crest length of 760 m, lowers the breach bottom to 279 masl (near the riverbed), shortens the formation time to 0.05 h and uses a weir coefficient of 3.3.

Table 2

Dam breach parameters adopted for the Base Case and the Worst Case

Parameter	Base Case	Worst Case
Failure mode	Overtopping	Overtopping
Trigger elevation	540 masl (FSL)	540 masl (FSL)
Breach width	608 m	760 m
Breach bottom elevation	460 masl	279 masl
Breach formation time	0.10 h	0.05 h
Left/right side slopes	Vertical (0)	Vertical (0)
Weir coefficient	3.1	3.3
Breach progression	Sinusoidal	Sinusoidal

Note. FSL = full supply level; masl = metres above sea level. Ranges follow FERC (1993).

Both scenarios started with the reservoir at 540 masl and used the same terrain, roughness and boundary conditions. The PMF hydrograph (peak 11,590.8 m^3/s) was applied as reservoir inflow, and a normal-depth condition based on the local bed slope was set at the downstream end of the domain. Flow from tributaries joining between the dam and the downstream boundary was not included, so the results show the effect of the breach alone. Each run began at breach initiation ($t = 0$) and lasted at least 72 hours, with the time step controlled by the Courant condition (maximum Courant number about 1). Maximum water-surface elevation, depth, velocity and arrival time were exported from RAS Mapper, and discharge hydrographs were extracted at 15 sections along the reach, including Narayangarh, Baraghare, Divyanagar and Meghauli.

Results

HEC-HMS Calibration and Validation

Table 3 summarises how well the model reproduced daily discharge at Arughat (Figure 3). In calibration (1995-2010), R^2 was 0.729, NSE 0.711 and PBIAS −12.40%; in validation (2011-2019) the values were 0.655, 0.557 and −2.10%. By the ratings of Moriasi et al. (2007), calibration NSE and PBIAS are good and validation NSE is satisfactory, while validation PBIAS is very good. Year by year, NSE was 0.55 or higher in 22 of the 25 years, ranging from 0.47 in 1995 to 0.84 in 2008. Bias was less even: in the validation years 2012 and 2015, PBIAS was +69.6% and +54.0%, so flow was clearly underestimated in those years.

Table 3

HEC-HMS performance for the calibration and validation periods

Period	R^2	NSE	PBIAS (%)
Calibration (1995-2010)	0.729	0.711	−12.40
Validation (2011-2019)	0.655	0.557	−2.10

Note. NSE = Nash-Sutcliffe efficiency; PBIAS = percent bias (negative values indicate overestimated volume).

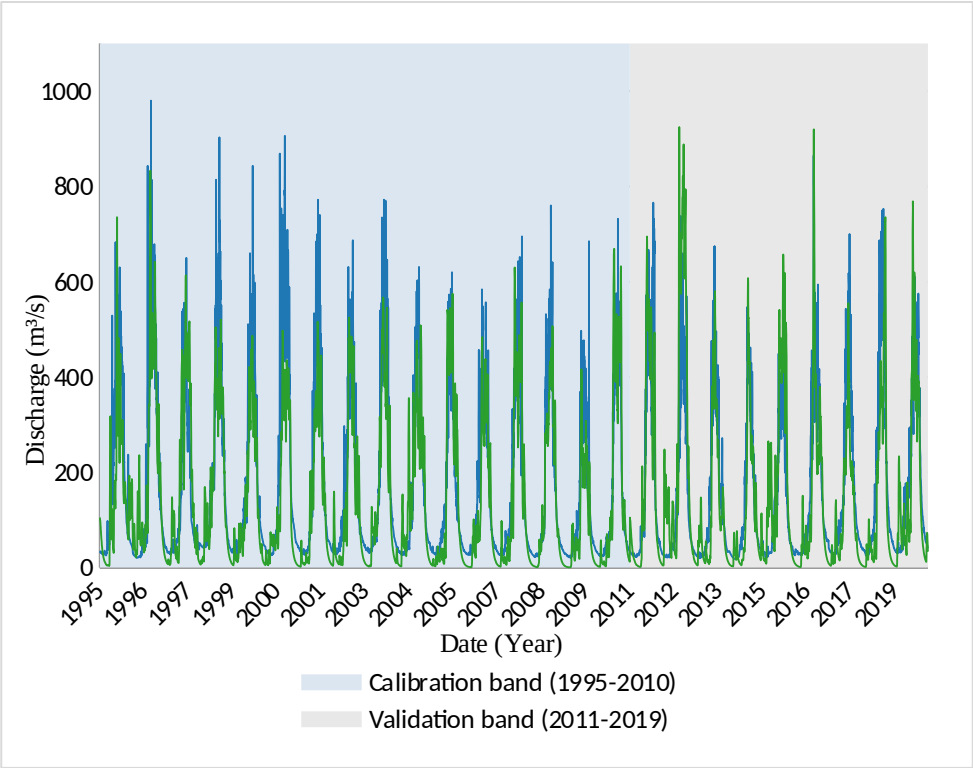


Figure 3

Observed and HEC-HMS simulated daily discharge at Arughat for the calibration (1995-2010) and validation (2011-2019) periods

Calibration NSE and R^2 were higher than the validation values, whereas the validation PBIAS was close to zero. The small validation bias partly reflects overestimates and underestimates in different years cancelling out, so the summary metrics should be read together with the hydrographs and the year-specific errors.

PMP and PMF

The basin-average PMP was 340.2 mm for 1 day and 452.9 mm for 3 days. Sub-basin values (Table A1, Appendix A) ranged from about 255 to 885 mm for 1 day and from about 363 to 1,150 mm for 3 days, with the highest depths in sub-basins 1, 8 and 10 and the lowest in sub-basin 4. Forcing the calibrated model with the 3-day PMP gave a PMF peak of 11,590.8 m³/s at the dam site (Figure 4). This is about 18% above the design flood of 9,809 m³/s and about 1.6 times the spillway capacity of 7,400 m³/s at FSL (BGHPP Development Committee, 2015).

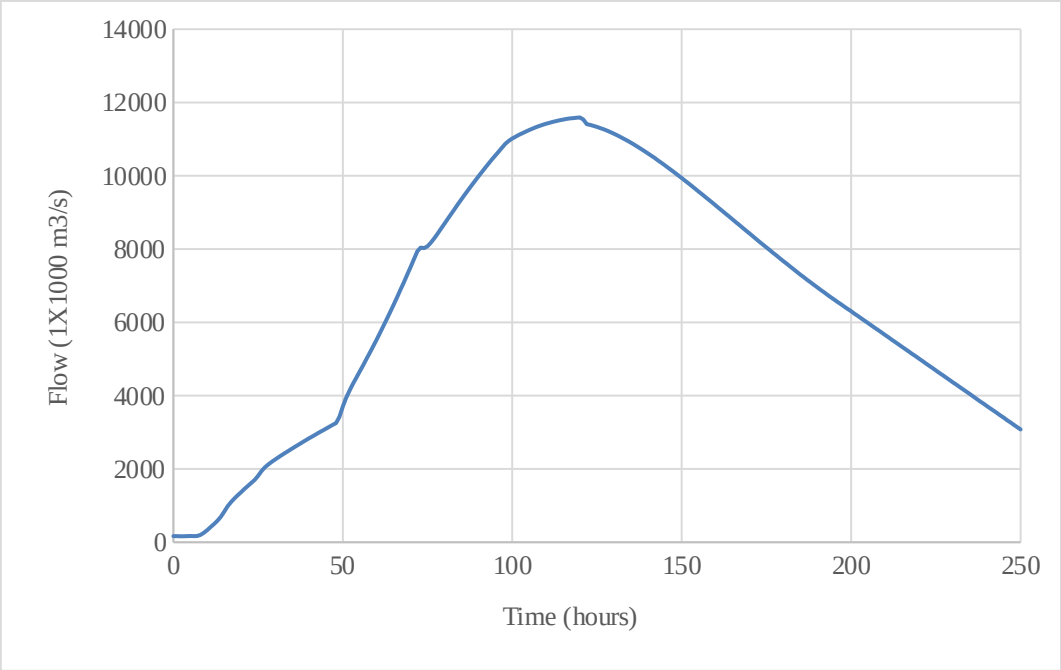


Figure 4

Probable maximum flood hydrograph at the Budhi Gandaki dam site for the 3-day PMP

Breach Outflow

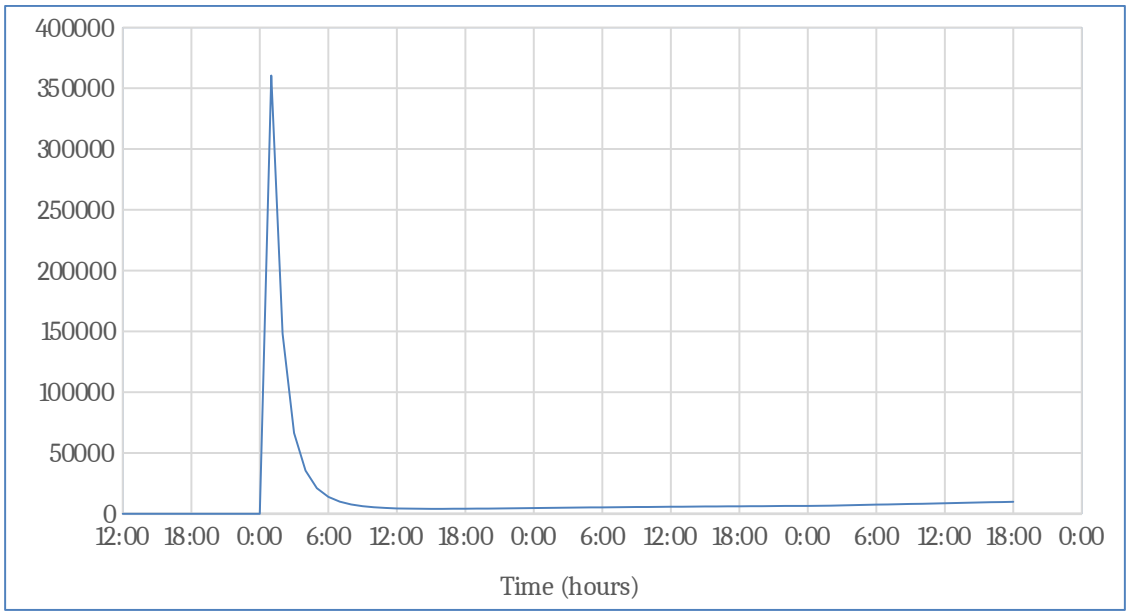
Breach outflow peaked at 360,456 m³/s in the Base Case, 16 minutes after breach initiation, and at 468,631 m³/s in the Worst Case after 12 minutes (Table 4; Figure 5). The maximum velocity through the breach was 12.59 m/s in the Base Case and 13.10 m/s in the Worst Case. The breach peaks are about 31 and 40 times the PMF inflow, and about 37 and 48 times the design flood of 9,809 m³/s.

Table 4

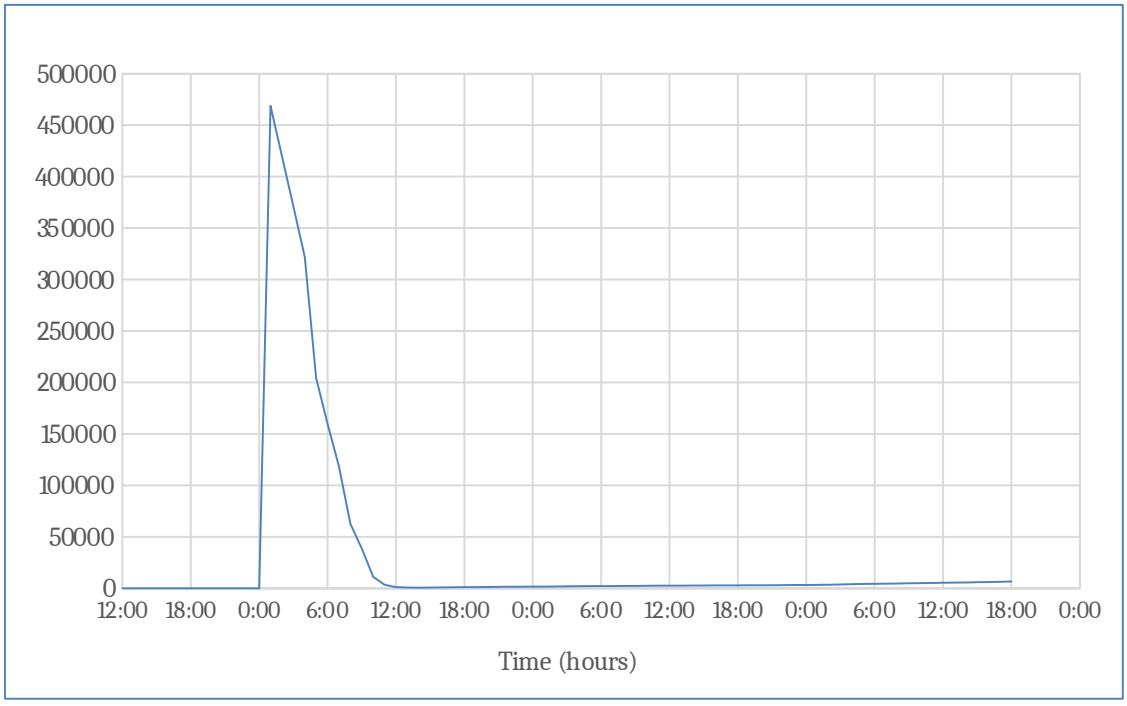
Breach outflow characteristics

Parameter	Base Case	Worst Case
Peak breach outflow (m³/s)	360,456	468,631
Time to peak (min)	16	12
Maximum breach velocity (m/s)	12.59	13.10
Ratio to PMF peak	31.1	40.4

Note. PMF = probable maximum flood (peak 11,590.8 m³/s).



(a) Base Case



(b) Worst Case

Figure 5

Breach outflow hydrographs at the dam connection for (a) the Base Case and (b) the Worst Case

Downstream Flood Propagation

Peak discharge generally decreased with distance from the dam (Table 5; Figures 6-8). In the Base Case it was 209,771 m³/s at 20 km, 118,136 m³/s at 40 km, 95,550 m³/s at Narayangarh and 84,889 m³/s at Meghauli; the matching Worst Case values were 312,918, 141,812, 122,338 and

114,590 m³/s. At the Super Trishuli HPP the simulated peaks were 198,974 and 298,364 m³/s. At Meghauli the peak was about 76% below the breach peak in both scenarios. The peak passed the 20 km section about 1.5 hours after breach initiation, reached Narayangarh after about 7 hours and Meghauli after about 9.5 hours. In the Worst Case the peak at 10 km (501,427 m³/s) is about 7% higher than the peak at the dam connection, so attenuation appears only beyond that section.

Table 5

Peak discharge and time of peak at sections along the river for the Base Case and the Worst Case

Section	Base Case (m³/s)	Worst Case (m³/s)	Time to peak (h)
10 km	290,584	501,427	0.5
20 km	209,771	312,918	1.5
Super Trishuli HPP	198,974	298,364	1.5
30 km	166,382	187,728	2.5
40 km	118,136	141,812	3.5
50 km	107,434	135,976	5.5
60 km	100,640	118,766	5.5
70 km	96,627	122,565	6.5
80 km	96,174	122,476	7.0
Narayangarh	95,550	122,338	7.0
Baraghare (90 km)	94,033	122,159	7.5
Divyanagar	91,369	121,357	8.5
Meghauli (100 km)	84,889	114,590	9.5
110 km	71,887	103,733	12.5
119 km	70,639	102,852	13.5

Note. Distances are measured downstream from the dam. Times are hours after breach initiation, to the nearest 0.5 h.

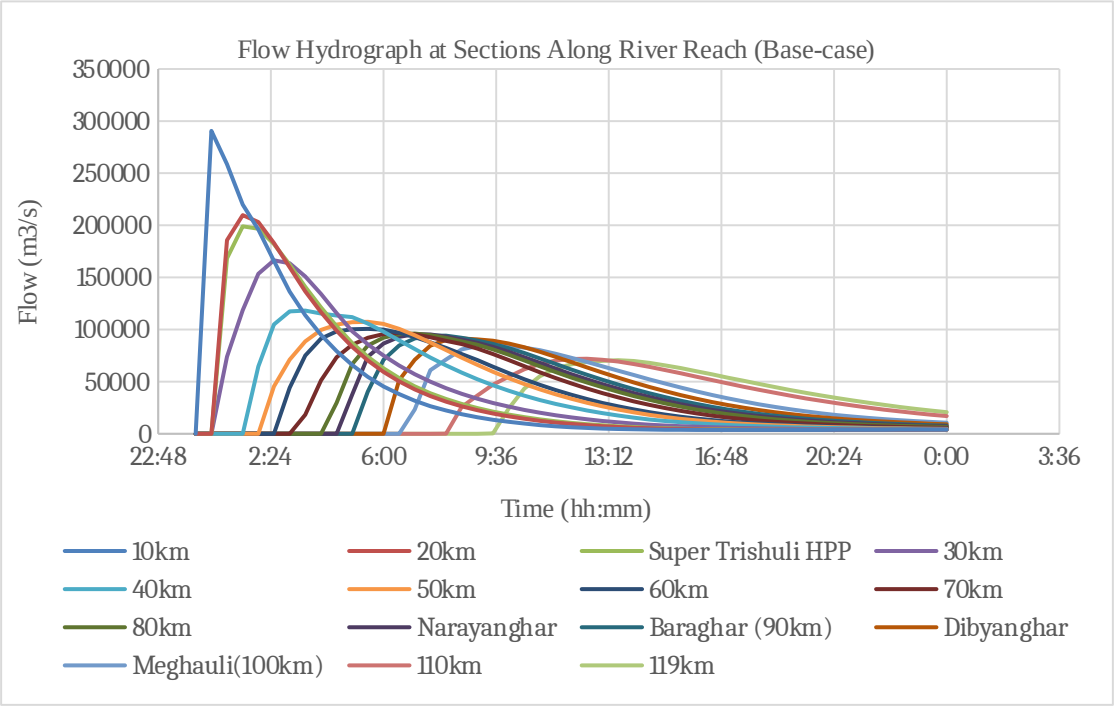


Figure 6

Flow hydrographs at selected sections along the river reach for the Base Case

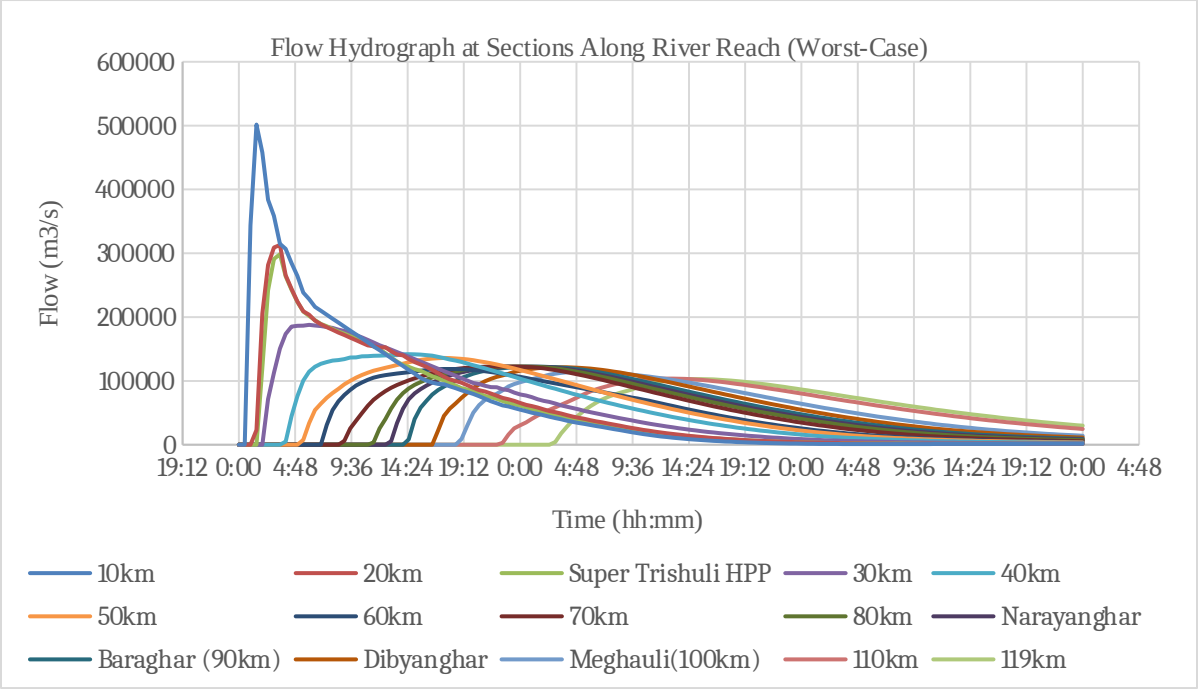


Figure 7

Flow hydrographs at selected sections along the river reach for the Worst Case

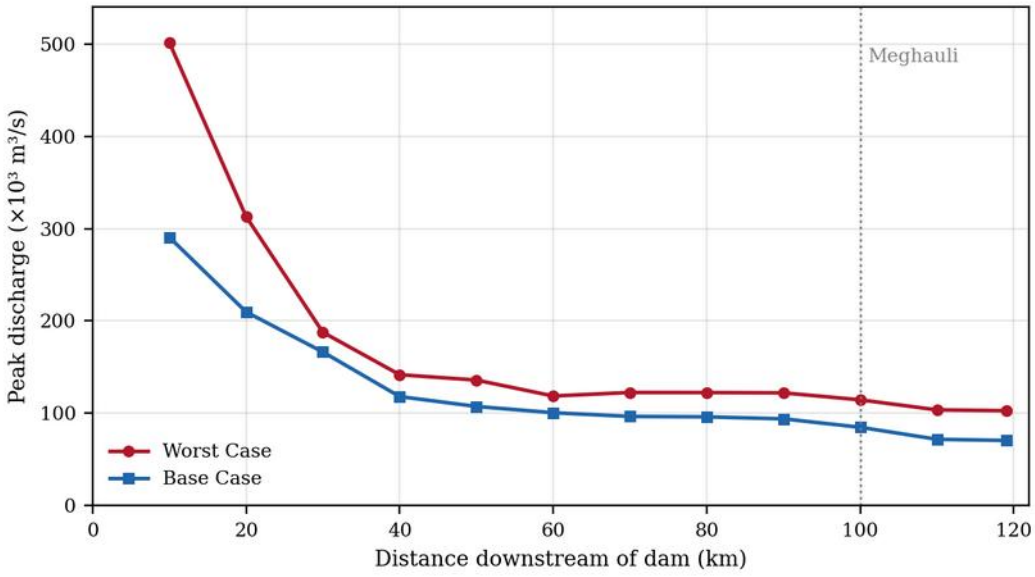


Figure 8

Simulated peak discharge along the river reach

Note. Plotted from the section values in Table 5; the Super Trishuli HPP section is omitted because its distance is not tabulated.

The highest velocities occurred within about 1 km of the dam: 23.74 m/s in the Base Case (at 0.92 km) and 32.87 m/s in the Worst Case (at 0.81 km). The greatest depth along the river profile was 77.95 m at 36.62 km in the Base Case and 187.46 m at 12.90 km in the Worst Case.

Discussion

The HEC-HMS model reproduced daily flow at Arughat well enough to support an extreme-flood estimate, but not uniformly. Calibration performance was good by the ratings of Moriasi et al. (2007), whereas the validation NSE of 0.557 was only satisfactory. The validation PBIAS of −2.1% does not mean the errors were small: overestimates and underestimates in individual years cancel, and the underestimation in 2012 and 2015 shows this. Khatri et al. (2018) reported an NSE of about 0.78 for HEC-HMS in the same basin, but the two studies differ in period and set-up, so the values are not strictly comparable. The present model has no separate snow or glacier melt component, which probably matters for dry-season flow in the upper catchment. For the rainfall-driven PMF, the PMP itself, in particular the envelope frequency factor of 15, is likely to add more uncertainty than the seasonal bias of the model, although this was not tested.

The PMF of 11,590.8 m³/s is higher than both the design flood and the spillway capacity given in the design report. It comes from one storm pattern and one parameter set, and it lies far outside the range of discharge used for calibration, so it depends on the adopted assumptions. Because the model runs on a daily time step, the value is also a daily-resolution peak, and the instantaneous peak could be higher. The PMF is best used as a check on the design basis and not as an independent replacement of it.

Once the reservoir fails, the inflow has little influence on the outflow. The breach peaks are 31 and 40 times the PMF, so the discharge is controlled mainly by the stored volume and the breach geometry. Awal et al. (2024) also found that the breach parameters, and the breach elevation in particular, drive the downstream flood magnitude for this dam. The Worst-Case peak is about 30% higher than the Base Case peak and occurs four minutes earlier. Breach width, bottom elevation, formation time and weir coefficient were changed together, so the difference cannot be assigned to any one of them. The lower breach bottom (279 instead of 460 masl) may account for much of it, given the result of Awal et al. (2024), but a one-at-a-time sensitivity analysis is needed to show this.

Along the river, the Base Case peak falls from about 210,000 m³/s at 20 km to about 85,000 m³/s at Meghauli, and the Worst-Case peak from about 313,000 to 115,000 m³/s. The loss of about three quarters of the breach peak by Meghauli probably reflects the valley opening out, flow spreading over the floodplain and channel friction, although these effects were not separated. The highest velocities occur within 1 km of the dam, where the river leaves a steep, narrow gorge, and the deepest water lies farther downstream, between about 13 and 37 km.

Awal et al. (2024) reported peaks of 286,000 to 511,000 m³/s at downstream settlements, with times to peak of 11.3 to 17 h. Their locations, breach parameters and model set-up differ from those used here, so a direct comparison is not possible. The peaks near the dam in this study (290,584 to 501,427 m³/s at 10 km) are of the same order. The peaks at Meghauli (84,889 and 114,590 m³/s) are lower than the range they report, although their settlements are not necessarily at the same distances, and a comparison at common locations would help to identify the cause. A peak that reaches 20 km within about 1.5 hours leaves very little warning time near the dam, while about 7 hours and 9.5 hours elapse before it reaches Narayangarh and Meghauli. These

times may serve as preliminary inputs for emergency action planning, but they need further validation before operational use.

Limitations

Several limitations should be considered when interpreting the results. The hydraulic model uses 30 m SRTM terrain data and a nominal 100 m computational mesh, which may not adequately represent narrow channels and engineered structures. Consequently, local flood depths and velocities in confined reaches, particularly the exceptionally large depths predicted in the gorge, remain uncertain. The reservoir volume derived from the terrain was lower than the reported design value; therefore, the reservoir storage curve was adjusted to match the design information. Tributary inflows between the dam and the downstream boundary were not included, and concurrent rainfall over these tributaries could increase downstream flood discharges. The PMF estimation is based on rainfall alone and does not explicitly account for snow and ice melt. Furthermore, the PMP estimate relies on a statistical method and a 40-year rainfall record, while the calibrated hydrological model is applied to an extreme event well beyond the range of observed conditions. The dam-breach simulations also rely on prescribed parameters selected from guideline ranges and do not represent the structural processes of cracking, deformation, or progressive failure that may occur in a concrete arch dam. Individual breach parameters were not tested through sensitivity analysis, adding uncertainty to the simulated breach hydrographs. In addition, discharge estimates extracted near the breach may be sensitive to the extraction location because of highly unsteady flow and the coarse mesh relative to the gorge geometry. Accordingly, the results should be interpreted as scenario-based estimates subject to hydrological, terrain, and breach-modelling uncertainties, rather than forecasts of an actual dam failure.

Conclusion

The coupled HEC-HMS and two-dimensional HEC-RAS models were used to estimate the probable maximum flood (PMF) and simulate the downstream consequences of a hypothetical overtopping failure of the proposed Budhi Gandaki Dam. The HEC-HMS model reproduced observed discharge at Arughat with Nash–Sutcliffe efficiency (NSE) values of 0.711 during calibration and 0.557 during validation. When driven by the Hershfield-based probable maximum precipitation (PMP), the model estimated a PMF peak discharge of 11,590.8 m^3/s at the dam site, exceeding the adopted design flood.

The simulated breach scenarios produced peak discharges of approximately 360,456 m^3/s in the Base Case and 468,631 m^3/s in the Worst Case, reached within 16 and 12 minutes of breach initiation, respectively. These peaks were approximately 31 and 40 times the PMF peak, demonstrating the strong influence of reservoir storage and breach geometry on the magnitude of the simulated outflow. Downstream, peak discharge decreased by approximately 76% by Meghauli, while the flood wave reached the 20 km section within about 1.5 hours. Despite this attenuation, the simulations indicate the potential for severe downstream flooding under the assumed conditions. The results represent hypothetical scenarios and should not be interpreted as predictions of dam failure or as a complete assessment of flood risk.

Further research should incorporate higher-resolution terrain and channel surveys, assess the sensitivity of results to individual breach parameters, and account for tributary inflows and potential snow and ice melt contributions. The effects of alternative PMP storm patterns should

also be investigated. Comparison with the findings of Awal et al. (2024) at common locations would help place the simulated results in context, while additional hydraulic validation and mesh-sensitivity testing are needed to evaluate model performance. These steps are particularly important before the predicted extreme depths and velocities are used to support inundation mapping, emergency planning, or other safety-related decisions

Acknowledgments

The authors thank the Department of Hydrology and Meteorology, Nepal, for the rainfall and discharge records, and the Department of Civil Engineering, Pulchowk Campus, Institute of Engineering, Tribhuvan University, for access to resources.

Funding

The author(s) received no financial support for the research, authorship, or publication of this paper.

Conflict of Interest

The author(s) declare no conflict of interest.

Author Contributions

Prabin Karn: conceptualization, data curation, HEC-HMS and HEC-RAS modelling, formal analysis, visualization, writing (original draft). Prinesh Maharjan: supervision, methodology, validation, writing (review and editing).

Data Availability

The SRTM terrain dataset is publicly available from the U.S. Geological Survey. Rainfall and discharge records are held by the Department of Hydrology and Meteorology, Nepal, and access is subject to its data policy. Dam and reservoir information was obtained from project design reports. The model input files and processed results are available from the corresponding author on reasonable request.

References

Altarejos-García, L., Escuder-Bueno, I., & Morales-Torres, A. (2015). Advances on the failure analysis of the dam-foundation interface of concrete dams. *Materials, 8*(12), 8255-8278. https://doi.org/10.3390/ma8125442

Athira, S., Katpatal, Y. B., & Londhe, D. S. (2023). Flood modelling and inundation mapping of Meenachil River using HEC-RAS and HEC-HMS software. In *Climate change and ocean renewable energy* (pp. 113-130). Springer. https://doi.org/10.1007/978-3-031-26967-7_9

Aureli, F., Maranzoni, A., & Petaccia, G. (2021). Review of historical dam-break events and laboratory tests on real topography for the validation of numerical models. *Water, 13*(14), Article 1968. https://doi.org/10.3390/w13141968

Awal, A., Bhattarai, U., Pandey, V. P., & Bhattarai, P. K. (2024). Downstream impacts of dam breach using HEC-RAS: A case of Budhigandaki concrete arch dam in central Nepal.

Environmental Systems Research, 13, Article 37. https://doi.org/10.1186/s40068-024-00358-3

BGHPP Development Committee. (2015). *Feasibility study and detailed design of Budhi Gandaki HPP: Phase 3, final detailed design report, Volume 1: Main report*. Tractebel Engineering SA in association with JADE Consult.

Bricker, J. D., Schwanghart, W., Adhikari, B. R., Moriguchi, S., Roeber, V., & Giri, S. (2017). Performance of models for flash flood warning and hazard assessment: The 2015 Kali Gandaki landslide dam breach in Nepal. *Mountain Research and Development, 37*(1), 5-15. https://doi.org/10.1659/MRD-JOURNAL-D-16-00043.1

Chow, V. T. (1959). *Open-channel hydraulics*. McGraw-Hill.

Costa, J. E. (1985). *Floods from dam failures* (Open-File Report 85-560). U.S. Geological Survey.

Earth Resources Observation and Science Center. (2019). *Shuttle Radar Topography Mission 1 Arc-Second Digital Terrain Elevation Data—Global—National Geospatial Data Asset (NGDA)* [Data set]. U.S. Geological Survey. https://doi.org/10.5066/F7PR7TFT

Fang, C.-H., Chen, J., Duan, Y.-H., & Xiao, K. (2017). A new method to quantify breach sizes for the flood risk management of concrete arch dams. *Journal of Flood Risk Management, 10*(4), 511-521. https://doi.org/10.1111/jfr3.12240

Federal Energy Regulatory Commission. (1993). *Engineering guidelines for the evaluation of hydropower projects: Appendix II-A—Dambreak studies*. Federal Energy Regulatory Commission.

Forest Research and Training Centre. (2022). *Land cover of Nepal* [Data set]. https://doi.org/10.26066/RDS.1972729

Froehlich, D. C. (1995). Embankment dam breach parameters revisited. In *Proceedings of the 1995 ASCE Water Resources Engineering Conference* (pp. 887-891). American Society of Civil Engineers.

Hershfield, D. M. (1965). Method for estimating probable maximum rainfall. *Journal—American Water Works Association, 57*(8), 965-972. https://doi.org/10.1002/j.1551-8833.1965.tb01486.x

International Commission on Large Dams. (1995). *Dam failures: Statistical analysis* (ICOLD Bulletin 99). International Commission on Large Dams.

Khatri, H. B., Jain, M. K., & Jain, S. K. (2018). Modelling of streamflow in snow dominated Budhigandaki catchment in Nepal. *Journal of Earth System Science, 127*(7), Article 100. https://doi.org/10.1007/s12040-018-1005-5

Manandhar, R., Bhattarai, S., Thakurati, R., Maharjan, S., & Shrestha, S. (2024). Integrated hydrological and hydraulic modeling for dam breach analysis: A case study of Mahadev Khola, Bhaktapur. *Journal of Engineering and Sciences, 3*(2), 43-60. https://doi.org/10.3126/jes2.v3i2.72190

Moriasi, D. N., Arnold, J. G., Van Liew, M. W., Bingner, R. L., Harmel, R. D., & Veith, T. L. (2007). Model evaluation guidelines for systematic quantification of accuracy in watershed simulations. *Transactions of the ASABE, 50*(3), 885-900. https://doi.org/10.13031/2013.23153

Pandey, B. R., Knoblauch, H., & Zenz, G. (2024). Potential dam breach flood assessment with the 2D diffusion and full dynamic wave equations using a Hydrologic Engineering Center-River Analysis System. *Water, 16*(2), Article 277. https://doi.org/10.3390/w16020277

Sarkar, S., & Maity, R. (2020). Estimation of probable maximum precipitation in the context of climate change. *MethodsX, 7*, Article 100904. https://doi.org/10.1016/j.mex.2020.100904

U.S. Army Corps of Engineers, Hydrologic Engineering Center. (2021). *HEC-RAS 2D modeling user's manual*. https://www.hec.usace.army.mil/confluence/rasdocs/r2dum/6.2

U.S. Army Corps of Engineers, Hydrologic Engineering Center. (2024). *HEC-HMS user's manual* (Version 4.13). https://www.hec.usace.army.mil/confluence/hmsdocs/hmsum/4.13/

World Meteorological Organization. (2009). *Manual on estimation of probable maximum precipitation (PMP)* (3rd ed.; WMO-No. 1045). World Meteorological Organization.

Appendix A

Table A1

PMP depths of the sub-basins for 1-day and 3-day rainfall

Sub-basin	Area (km²)	1-day PMP (mm)	3-day PMP (mm)
Sub-basin 1	199.83	862.8	1,120.2
Sub-basin 2	712.83	390.7	587.8
Sub-basin 3	274.03	379.6	716.7
Sub-basin 4	526.29	254.8	362.7
Sub-basin 5	377.39	441.5	753.1
Sub-basin 6a	126.51	551.5	937.3
Sub-basin 6b	770.65	441.7	665.4
Sub-basin 8	800.01	885.1	1,149.9
Sub-basin 10	485.59	885.1	1,149.9
Sub-basin 12	247.73	329.3	539.5
Sub-basin 20	475.45	370.2	689.3

Note. PMP = probable maximum precipitation, estimated with the Hershfield method. Two sub-basins carry the label 6 in the HEC-GeoHMS output and are distinguished here by the suffixes a and b. Sub-basin areas sum to 4,996.3 km².

A Case Study on Numerical Modelling of a Run-of-River Gated Weir

Smriti Gautam[1], Mukesh Raj Kafle[1], Ram Krishna Regmi[1]

[1]Department of Civil Engineering, Pulchowk Campus, Institute of Engineering, Tribhuvan University
Lalitpur, Nepal
Corresponding author: 080mshpe022.smriti@pcampus.edu.np

Abstract

This study evaluates the hydraulic response of a three-bay, flat-bottom gated weir at a run-of-river hydropower project in Nepal using three-dimensional computational fluid dynamics (CFD). The numerical model was developed in FLOW-3D HYDRO 2025, with the Volume of Fluid (VOF) method for the free surface and the Renormalized Group (RNG) k–ε turbulence model. A uniform mesh size of 0.6 m was adopted, comprising approximately 2.78 million cells. The principal quantitative comparison was conducted for the 10,000-year design flood of 3,779.5 m^3/s, with CFD results compared against available measurements from a 1:50 physical model at 12 matched locations. The comparison yielded a water-surface-elevation bias of +1.77 m, a mean absolute error (MAE) of 2.66 m and a root-mean-square error (RMSE) of 3.64 m. For velocity magnitude, the bias was +2.35 m/s, the MAE was 5.25 m/s and the RMSE was 6.13 m/s. These errors indicate that the model reproduces broad flow patterns but does not reliably resolve all local hydraulic conditions. The simulation identified the right bay and the downstream apron region as areas of comparatively high velocity and lower pressure, although lateral predictions remain uncertain because the upstream river bend was omitted from the computational domain. The results support the use of CFD for comparative scenario assessment and preliminary identification of potentially critical zones, rather than as a standalone basis for local scour or final cavitation-protection design. Further work should address domain extent, downstream tailwater, mesh sensitivity, air entrainment, sediment transport and gate-operation scenarios.

Keywords: Numerical Modelling, Run of River, Gated Weir, Flood, Physical Modelling

Introduction

Himalayan rivers experience substantial seasonal and spatial variation in flow associated with monsoon rainfall, snowmelt and glacial melt (Bookhagen & Burbank, 2010). These conditions provide opportunities for run-of-river hydropower development, in which a diversion weir raises the upstream water level and directs part of the river flow towards an intake (Jha, 2011). At the same time, the weir must safely convey floods and withstand sediment- and debris-laden flows. Inadequate conveyance or energy dissipation can lead to high velocities, pressure fluctuations and downstream scour, potentially threatening the weir and adjacent structures (Chanson, 2004; Novak et al., 2017).

Flow through a gated weir is three-dimensional, rapidly varied and turbulent. Contraction at the gates, vortex shedding around piers and the formation of high-velocity jets can produce complex flow patterns over the apron and in the downstream reach (Ota & Sato, 2015). Local low pressures may also indicate areas requiring further investigation for cavitation risk. Physical hydraulic models are commonly used to examine these processes, but they require laboratory facilities, time and resources, and the number of test conditions may be limited. Computational fluid dynamics (CFD) can complement physical modelling by providing spatially distributed

estimates of water level, velocity and pressure. Its usefulness, however, depends on appropriate model setup and verification against relevant measurements.

CFD accuracy is affected by mesh resolution, turbulence closure, boundary conditions and the representation of the physical geometry. Published comparisons report on differing levels and patterns of agreement. Sadiq et al. (2025) found close agreement between numerical and physical spillway results, whereas Moghadam et al. (2025) reported that the RNG k–ε model underpredicted peak velocities and overpredicted minimum velocities. Research on Nepalese headworks has also demonstrated the potential of CFD while highlighting the structure-specific nature of hydraulic behaviour (Kafle, 2024; Khakurel et al., 2020). Results from one structure should therefore not be transferred directly to another with a different bay arrangement, geometry or design discharge.

The present study examines a three-bay gated weir at a Himalayan run-of-river hydropower project. Its contribution is a case-specific comparison of FLOW-3D predictions with available 1:50 physical-model data, together with an assessment of bay-wise flow patterns and the practical limits of CFD for preliminary hydraulic design. The study aims to: (i) evaluate hydraulic performance of weir under 10,000-year design flood; and (ii) assess suitability of validated CFD model as a complementary tool for hydraulic design.

Literature Review

Gated weirs allow operators to regulate upstream levels during normal conditions and to increase conveyance by opening gates during floods (Chanson, 2004; Novak et al., 2017). Flow acceleration through the openings forms jets that impinge on the apron and generate high shear stress and turbulence (Ota & Sato, 2015). A hydraulic jump may dissipate part of the flow energy downstream, although its position and stability depend on tailwater depth and stilling-basin geometry (Chanson, 2004). If energy dissipation is inadequate, the downstream bed and apron may be exposed to damaging scour (Dey & Sarkar, 2006).

Many CFD studies of weirs and spillways solve the Reynolds-averaged Navier–Stokes equations using a k–ε-family turbulence model and track the free surface with the Volume of Fluid method (Hirt & Nichols, 1981; Versteeg & Malalasekera, 2007). Reported agreement varies with geometry, boundary conditions and validation data. Sadiq et al. (2025) reported low errors for velocity and flow depth in a spillway study. Kim et al. (2022) reported agreement for discharge and velocity in a validated numerical model of downstream hydraulic structures. In contrast, Moghadam et al. (2025) found substantial discrepancies in local velocity predictions using the RNG model. Other studies have selected RNG k–ε for investigations of downstream scour and flow over weirs with openings (Daneshfaraz et al., 2019; Zaffar et al., 2023), but the suitability of a turbulence closure remains case-dependent.

For Nepal, Khakurel et al. (2020) used CFD to investigate the influence of intake orientation and divide-wall geometry on flow division at the Solu Khola Dudhkoshi headworks. Kafle (2024) assessed cavitation-related parameters and extreme-flood conveyance at the Sunkoshi Marin diversion. The present study builds on this applied work by comparing CFD results with physical-model measurements for a three-bay gated weir and by explicitly discussing the implications of observed discrepancies for design use. The scope is case-specific; the results are not intended to establish universal accuracy for CFD modelling of Himalayan headworks.

Materials and Methods

Study Site and Weir Geometry

The study concerns a high-head run-of-river hydropower scheme under construction in Nepal. The weir axis is located approximately 250 m downstream of the confluence with the Bhote Koshi. The catchment area is 4,351 km², and the mean annual discharge is 183 m³/s. The valley is narrow and V-shaped, with an average bed slope of 3.8% and a river width of approximately 30–40 m. Reported monthly mean flow ranges from 38.6 to 557.8 m³/s, while mean monthly sediment concentration ranges from 35 to 1,798 mg/L. The scheme diverts a design discharge of 76 m³/s to an underground powerhouse.

The weir is a flat-bottom gated sluice structure comprising three openings, each 11 m wide, separated by two 3 m piers. The invert is at elevation 1,238 m above sea level (masl), the crest is at 1,259 masl, and the operating water level is 1,255 masl. A 55 m-long apron extends downstream of the gates. The structure is required to pass the 10,000-year design flood of 3,779.5 m³/s without overtopping.

Flood Scenarios

The 10,000-year flood discharge was estimated by fitting a Gumbel distribution to 33 years (1992–2024) of annual instantaneous maximum discharge records at the site. The quantitative CFD-to-physical-model comparison reported in this paper concerns the fully open-gate condition at this discharge.

Table 1

Simulated Flow Conditions

Case	Flow condition	Discharge (m³/s)	Source	Physical-model comparison
1	10,000-year design flood; all gates fully open	3,779.5	Gumbel distribution	Quantitative and qualitative

Physical Model

Reference data were obtained from a 1:50 Froude-scaled laboratory model. The physical model represented approximately 550 m of river upstream and 500 m downstream of the weir axis. Discharge was controlled using an upstream rectangular measuring weir; water levels were measured with level gauges, and velocities were measured with propeller flow meters. For the 10,000-year flood, 12 matched measurement points were available at chainages 88, 100, 125 and 175 m, with left, middle and right positions at each chainage.

Numerical Model

The numerical model was developed in FLOW-3D HYDRO 2025 using gravity, the VOF method to represent the water–air interface, and the RNG k–ε turbulence model. Geometry was prepared using Civil 3D, SketchUp and Blender and imported as an STL file (Figure 1). The model included the three bays, piers, approach, gate sill and apron. Gate trunnions, the fish ladder and the intake were omitted. The upstream river bend was also excluded from the CFD geometry.

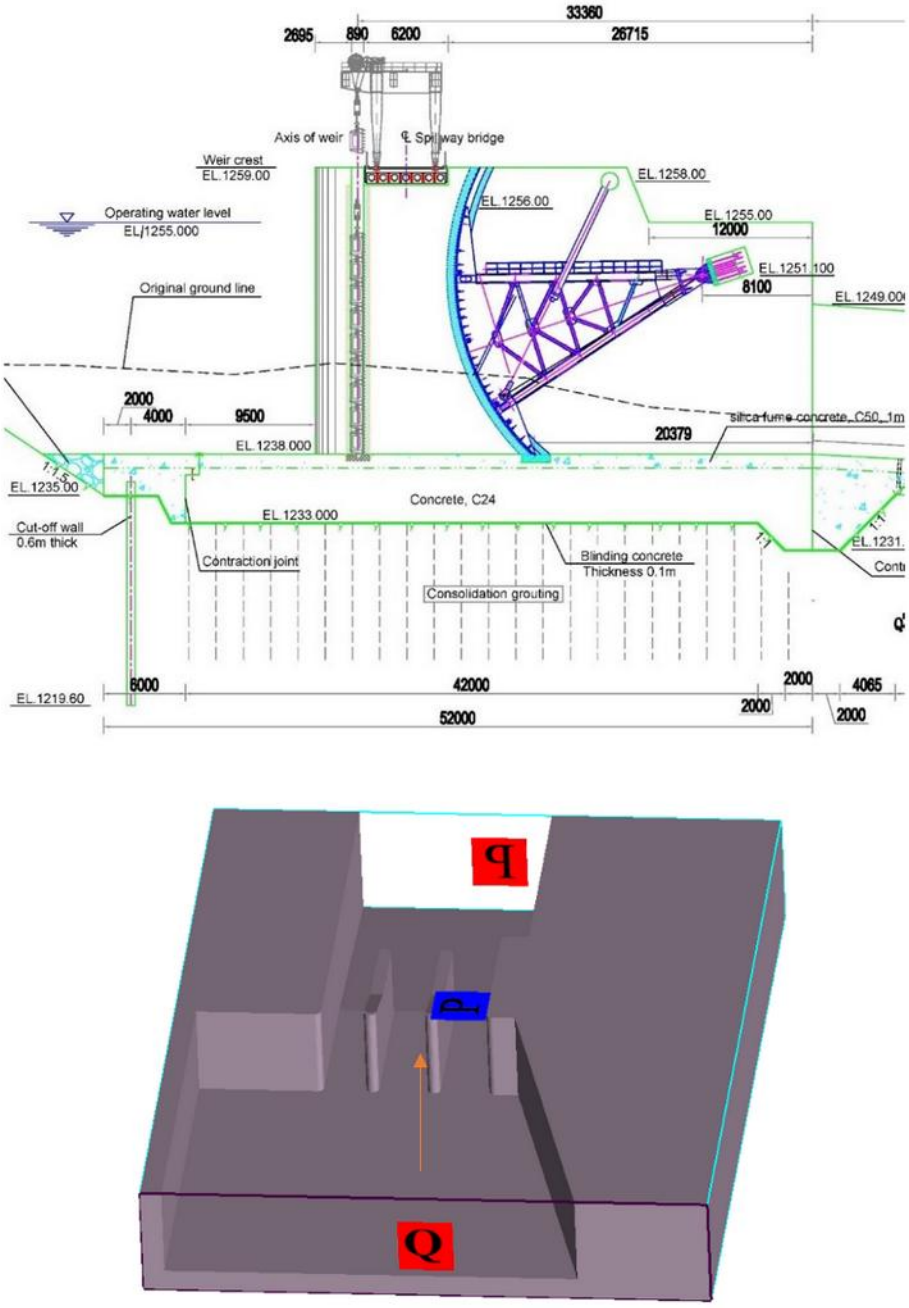
The computational domain extended approximately 70 m upstream and 100 m downstream of the pier centreline and covered the full width of the bays. A uniform volumetric flow rate was specified at the upstream boundary. The downstream boundary was a pressure boundary at

atmospheric pressure, without an imposed tailwater level. Side boundaries were treated as symmetry planes, the top boundary was open to atmospheric pressure, and the bed, piers, gates and apron were modelled as no-slip walls.

A uniform cell size of 0.6 m across the three mesh blocks, comprising 2,776,490 cells, was selected as a compromise between resolution and computational cost. Solution stability was assessed using volumetric flow rate and mean kinetic energy. A 30 s simulation was considered too short; each case was therefore run for 100 s, with both monitored quantities reported as nearly constant after approximately 75 s. Because a formal grid-convergence study was not completed, the selected mesh should be regarded as a practical modelling choice rather than a demonstrated grid-independent solution.

Figure 1

Headworks Section Drawing and FLOW-3D Geometry of the Weir



Note. (a) Headworks section drawing. (b) Three-dimensional geometry used in the model.

Evaluation Metrics

At each matched measurement point, the error was defined as the CFD value minus the physical-model value; positive values therefore indicate overprediction by CFD. Agreement was summarized using bias, mean absolute error (MAE) and root-mean-square error (RMSE), calculated over n matched points:

(2)

(3)

where C_i is the CFD result and P_i is the corresponding physical-model measurement. These metrics describe the magnitude and direction of the discrepancies but do not, by themselves, establish whether the model is adequate for a particular design decision.

Results

Comparison with the Physical Model

For the conditions assessed qualitatively, the CFD model reproduced the broad sequence of flow features visible in the physical model: an upstream pool, drawdown through the three bays, acceleration over the apron and a downstream energy-dissipation region. The transition zone shifted downstream as discharge increased, accompanied by more turbulent flow. However, agreement in the lateral distribution of flow was weaker. The physical model includes an upstream bend that generates an asymmetric approach flow, whereas the CFD domain omits that bend and applies a uniform inflow. At the 100-year flood, for example, the CFD results reportedly reproduced the principal drawdown and downstream flow concentration but did not reproduce the measured cross-channel difference in water level.

For the 10,000-year flood, Table 2 and Figure 2 summarise the 12 matched measurement points. Water-surface elevation was overpredicted on average, with a bias of +1.77 m, an MAE of 2.66 m and an RMSE of 3.64 m. The largest overprediction occurred at the 88 m chainage, while the closest agreement was reported at 125 m. At 175 m, CFD underpredicted the measured water level at all three lateral positions, by as much as 3.92 m on the right.

Velocity magnitude showed larger discrepancies: the bias was +2.35 m/s, the MAE was 5.25 m/s and the RMSE was 6.13 m/s. CFD underpredicted velocity at 88 m, showed the closest agreement at 100 m, and overpredicted velocity at 125 m and 175 m. The largest reported velocity error was +11.22 m/s at the right-side point at 175 m. Whereas the computed velocities increased along the reach, the physical-model measurements were highest at the upstream chainages and lower at 125 m and 175 m (Figure 2b). This difference indicates that the model did not reproduce the measured downstream velocity trend reliably.

Table 2

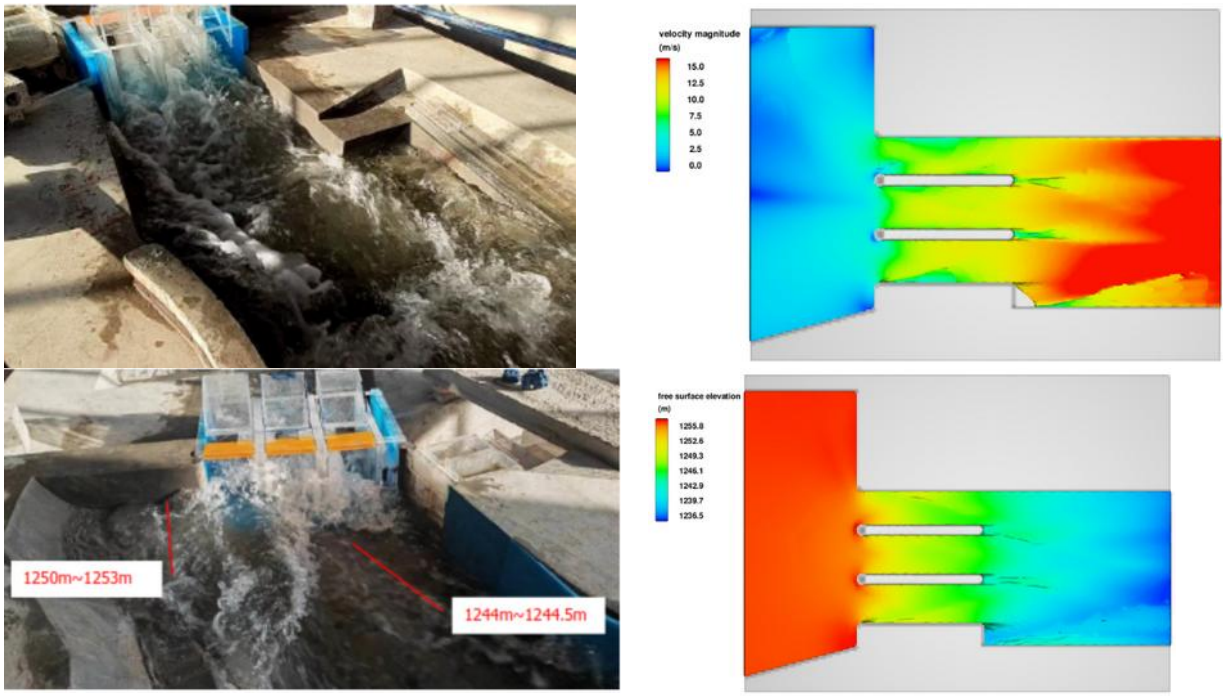
Error Statistics for the 10,000-Year Flood (CFD minus Physical Model)

Variable	n	Bias	MAE	RMSE	Location of largest error
Water-surface elevation (m)	12	+1.77	2.66	3.64	88 m chainage (upstream)
Velocity magnitude (m/s)	12	+2.35	5.25	6.13	175 m chainage, right bay (+11.22 m/s)

Note. MAE = mean absolute error; RMSE = root-mean-square error. Positive bias indicates CFD overprediction.

Figure 2

CFD and Physical-Model Values at the 12 Comparison Points, 10,000-Year Flood



Note. (a) Water-surface elevation (masl). (b) Velocity magnitude (m/s). Points are numbered along the sampled chainages of 88, 100, 125 and 175 m, each at three lateral positions.

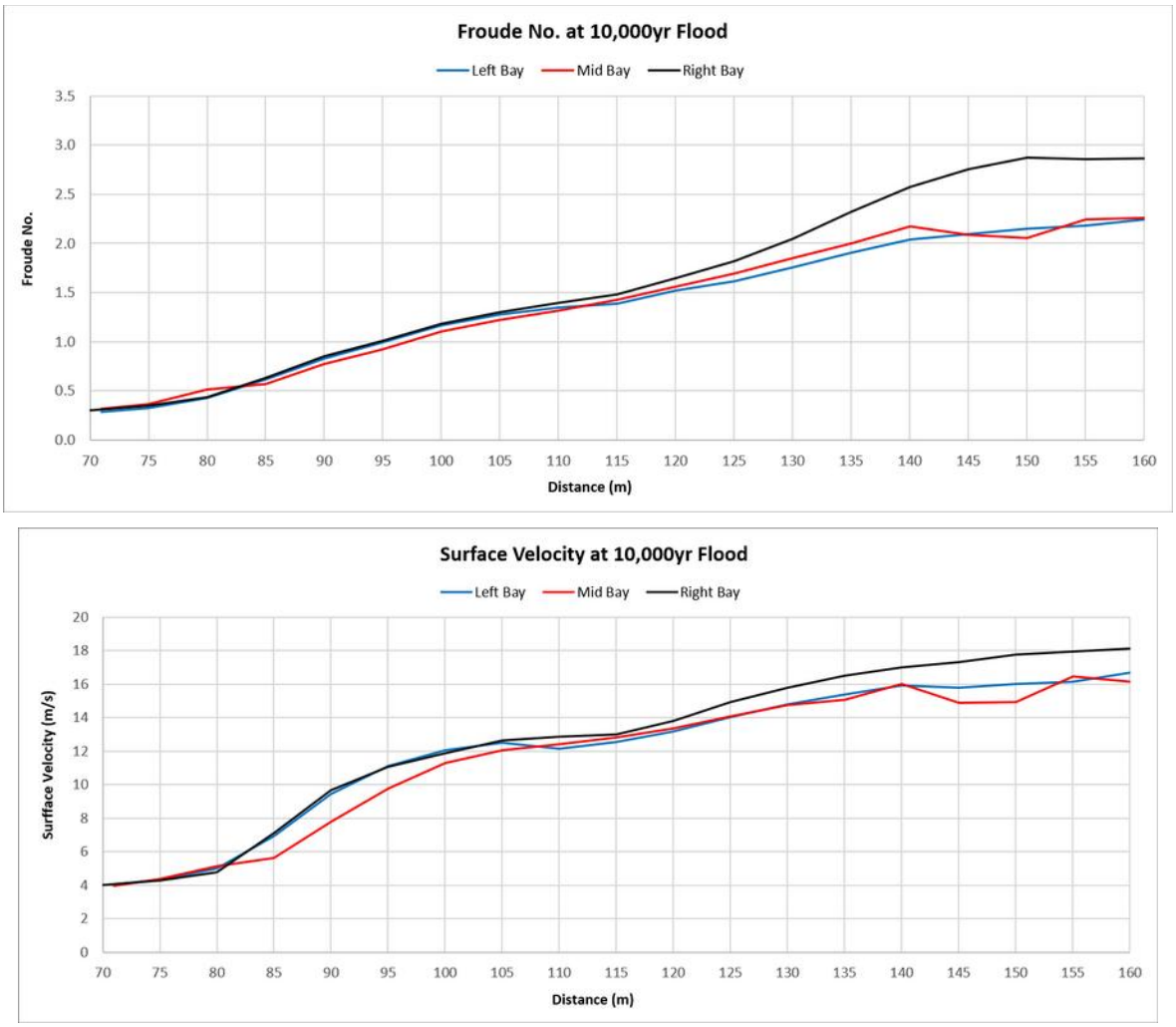
Bay-wise Hydraulic Behavior

The three bays exhibited similar broad flow patterns, but differences became more apparent downstream of approximately 120 m (Figures 3 and 4). In the CFD results, the right bay was shallower and faster than the left and middle bays. Its Froude number reached approximately 2.9, compared with about 2.2 in the other two bays. The reported peak surface velocity in the right bay was approximately 18.2 m/s, and the near-bed velocity was approximately 16.6 m/s. The corresponding pressure was reported to fall to about 40 kPa, compared with approximately 50–60 kPa elsewhere.

These results identify the downstream right-bay region as a candidate for closer investigation in subsequent design assessment. They should not, however, be interpreted as definitive local design values. The omission of the upstream bend, the simplified inflow and the mismatch in downstream velocity trends limit confidence in the predicted lateral distribution.

Figure 3

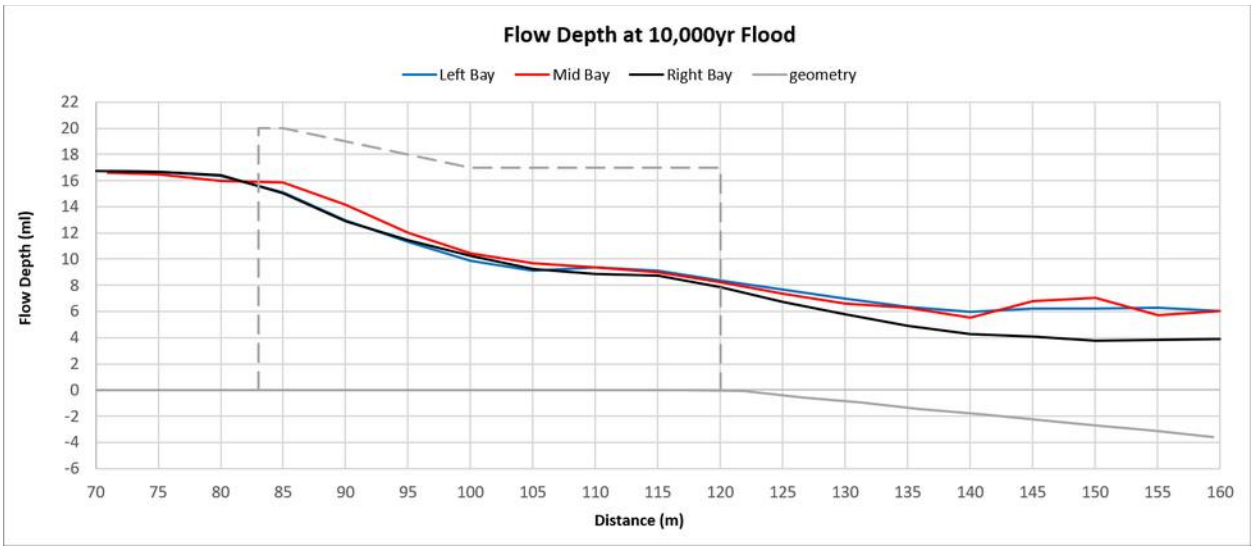
Froude Number and Surface Velocity along the Reach for the 10,000-Year Flood

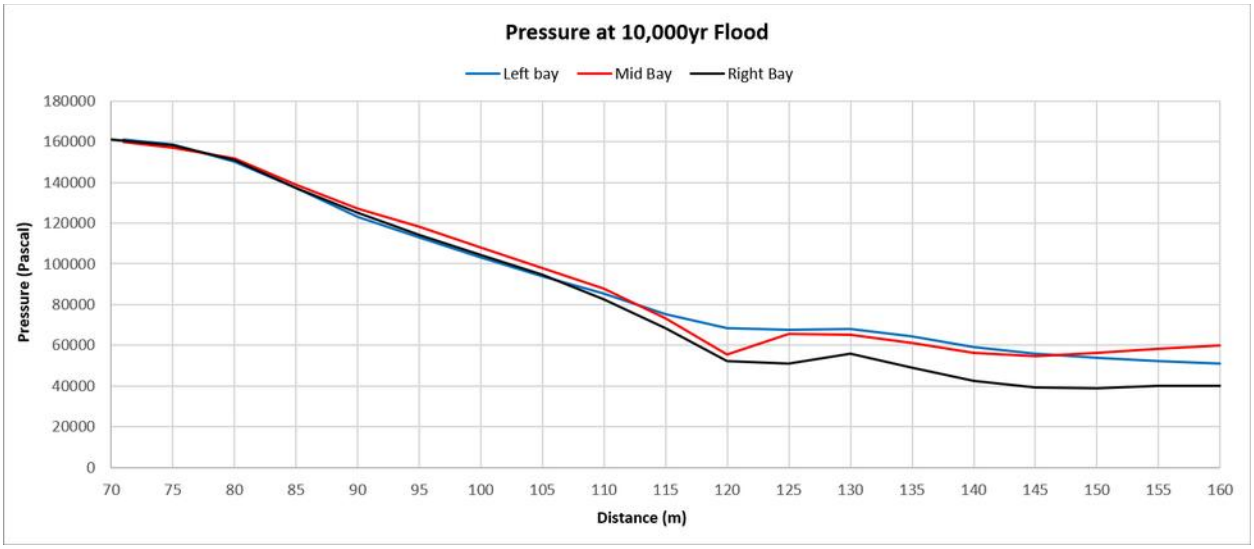


Note. (a) Froude number. (b) Surface velocity (m/s). The horizontal axis is distance along the model reach (m).

Figure 4

Flow Depth and Pressure along the Reach for the 10,000-Year Flood





Note. (c) Flow depth (m) (d) Pressure (Pa). The horizontal axis is distance along the model reach (m)

Discussion

The comparison indicates that the model captures broad hydraulic behaviour but has substantial local discrepancies. For the 10,000-year flood, the water-level RMSE was 3.64 m and the velocity RMSE was 6.13 m/s. These errors are materially larger than the low relative errors reported in some published spillway studies, including Sadiq et al. (2025), although direct comparison across studies is limited by differences in geometry, measurement locations, flow conditions and error definitions. The 12 matched points also show that errors are not uniform: water levels are overpredicted upstream and underpredicted at the farthest downstream chainage, while velocity is underpredicted at 88 m and overpredicted farther downstream. The model therefore should not be described as quantitatively accurate for local velocity or water-level prediction.

Several modelling choices may contribute to the observed discrepancies. The CFD domain covers approximately 170 m of river, compared with roughly 1 km represented by the physical model. Excluding the upstream bend and bank topography, and imposing uniform inflow, may alter the approach-flow distribution. In addition, no tailwater level was imposed at the outlet; this may contribute to the modelled downstream velocity increase and affect the location of energy dissipation. The effects of domain length and outlet treatment were not isolated in the present simulations, so these explanations should be treated as plausible contributors rather than demonstrated causes.

The model used VOF with RNG k–ε, but air entrainment was not explicitly modelled. This is a limitation for highly aerated, high-velocity flows, and a 1:50 Froude-scaled physical model may also exhibit scale effects in turbulence and aeration (Chanson, 2015). Point velocity measurements in aerated, fluctuating flow may have additional uncertainty. The present study cannot quantify the relative contribution of these factors. Although previous studies have used RNG k–ε for related hydraulic problems (Daneshfaraz et al., 2019; Zaffar et al., 2023), alternative turbulence closures were not tested here.

The results support using the present CFD model to compare broad flow patterns and to identify candidate areas for further investigation. They do not, on their own, support detailed sizing of scour protection or final cavitation measures. The reported absence of overtopping in the simulation is a model outcome, not conclusive verification of design safety. Before relying on it for design acceptance, the maximum computed water-surface elevation should be compared with the relevant crest or protection elevations, the available freeboard should be quantified, and uncertainty associated with the model setup should be considered. For the project studied, the right-bay apron and the reported 120–160 m downstream zone merit further assessment, ideally with an extended domain and boundary conditions aligned with the physical model.

Table 3

Suitability of the CFD Model for Design Questions

Design question	Suitability	Recommended use
Overall water-level trend	Indicative; quantitative discrepancies remain substantial	Use cautiously for relative scenario comparison; verify critical levels independently
Identification of high-velocity zones	Useful for preliminary screening, with local uncertainty	Identify candidate areas for detailed investigation
Local downstream velocity	Limited, given the measured-versus-computed trend mismatch	Confirm against physical-model data and improved CFD setup

Design question	Suitability	Recommended use
Hydraulic-jump position	Indicative only under the present outlet condition	Assess using tailwater sensitivity and physical-model observations
Local scour	Not established by the present simulations	Undertake a separate scour assessment
Gate-operation comparison	Not demonstrated by the fully open-gate case alone	Simulate additional gate configurations before making operational comparisons

Note. This assessment is specific to the model setup and the evidence presented in this study.

Limitations and Further Work

The present study has several limitations. The quantitative validation is based on 12 matched points for one flood condition with all gates fully open. The upstream river bend and some site features were omitted from the numerical geometry, and no tailwater level was imposed at the outlet. The selected mesh was not supported by a formal grid-convergence assessment. Sediment transport and air entrainment were not modelled, and partial or asymmetric gate operation was not assessed. In addition, the current manuscript does not provide sufficient information to independently evaluate the cavitation index calculation or its critical threshold.

Further work should extend the computational domain to represent the upstream bend and relevant bank topography, impose a downstream water level consistent with the physical-model condition, and quantify sensitivity to mesh resolution and boundary conditions. Additional simulations should assess partial and asymmetric gate openings, while improved treatment of aeration and sediment processes may be needed for specific design questions. The cavitation-index definition, pressure reference, vapour-pressure assumptions and acceptance criterion should be documented explicitly. Where the result affects safety-critical design, CFD predictions should be assessed alongside physical-model evidence and other appropriate engineering analyses.

Conclusion

A three-dimensional FLOW-3D HYDRO model was developed to assess the hydraulic response of a three-bay gated weir at a Himalayan run-of-river hydropower project. For the 10,000-year design flood of 3,779.5 m³/s, comparison with 12 physical-model measurement points produced a water-surface-elevation bias of +1.77 m, an MAE of 2.66 m and an RMSE of 3.64 m. For velocity magnitude, the bias was +2.35 m/s, the MAE was 5.25 m/s and the RMSE was 6.13 m/s. The results indicate that the model reproduced broad flow patterns but did not reliably resolve local water levels and velocities throughout the comparison reach.

The CFD results identified the right bay and downstream apron region as areas of comparatively high velocity and lower pressure. Given the simplified approach geometry, absence of an imposed tailwater level and lack of formal grid-convergence testing, these local patterns should be treated as screening results rather than final design values. The simulated absence of overtopping should likewise be verified through explicit freeboard assessment and consideration of model uncertainty.

The model is therefore best used as a complementary tool for preliminary scenario assessment and identification of potentially critical zones. It should not be used alone to establish local scour requirements, final cavitation protection or design safety. Future work should improve domain

and boundary-condition representation, quantify mesh and boundary sensitivity, document the cavitation assessment, and examine additional gate-operation scenarios. For safety-critical decisions, numerical predictions should be interpreted together with physical-model evidence and other relevant engineering analyses.

Acknowledgments

The author thanks supervisors, mentors, friends and family for continuous support, guidance and motivation. The author is grateful to the Project for providing data and permission to conduct the study, and to the FLOW-3D Academic Program for the academic license and technical guidance.

Funding

The author received no financial support for the research, authorship, or publication of this paper.

Conflict of Interest

The author declares no conflict of interest.

Author Contributions

S.G.: conceptualization, methodology, software, validation, formal analysis, investigation, visualization, and writing (original draft, review and editing).

Data Availability

The physical-model report and hydrological data belong to the project and are not publicly available. Simulation outputs summarized in this paper may be available from the corresponding author on reasonable request.

References

Bookhagen, B., & Burbank, D. W. (2010). Toward a complete Himalayan hydrological budget: Spatiotemporal distribution of snowmelt and rainfall and their impact on river discharge. Journal of Geophysical Research: Earth Surface, 115(F3), Article F03019. https://doi.org/10.1029/2009JF001426

Chanson, H. (2004). The hydraulics of open channel flow: An introduction (2nd ed.). Butterworth-Heinemann.

Chanson, H. (2015). Hydraulics of aerated flows: Qui pro quo? Journal of Hydraulic Research, 53(2), 223–243. https://doi.org/10.1080/00221686.2014.993269

Daneshfaraz, R., Ghahramanzadeh, A., & Keshavarzi, A. (2019). Three-dimensional numerical simulation of flow over a broad-crested weir with openings. Journal of Hydraulic Research, 57(5), 676–689. https://doi.org/10.1080/00221686.2018.1499057

Dey, S., & Sarkar, A. (2006). Scour downstream of an apron due to submerged horizontal jets. Journal of Hydraulic Engineering, 132(3), 246–257. https://doi.org/10.1061/(ASCE)0733-9429(2006)132:3(246)

Hirt, C. W., & Nichols, B. D. (1981). Volume of fluid (VOF) method for the dynamics of free boundaries. Journal of Computational Physics, 39(1), 201–225. https://doi.org/10.1016/0021-9991(81)90145-5

Jha, R. (2011). Hydropower development in Nepal. Tribhuvan University Press.

Kafle, M. R. (2024). Evaluate hydraulic performance of headworks using FLOW-3D for Sunkoshi Marin Diversion Multipurpose Project [Unpublished technical report]. Institute of Engineering, Tribhuvan University.

Khakurel, S., et al. (2020). Evaluation of hydraulics of headworks using CFD approach for Solu Khola Dudhkoshi HEP. Journal of the Institute of Engineering, 16(1), 157–165.

Kim, B., Han, Y., Lee, J., & Kim, D. (2022). Analysis of flow characteristics of downstream hydraulic structures using a validated numerical model. Journal of Hydraulic Engineering, 148(6), Article 04022025. https://doi.org/10.1061/(ASCE)HY.1943-7900.0001995

Moghadam, A., et al. (2025). Assessment of hydraulic parameters of an open channel spillway through numerical and experimental approaches for Romaine IV Spillway. Journal of Hydraulic Research, 63(1), 45–61.

Novak, P., Moffat, A. I. B., Nalluri, C., & Narayanan, R. (2017). Hydraulic structures (5th ed.). CRC Press.

Ota, K., & Sato, T. (2015). Numerical analysis of high velocity jet flow downstream of sluice gates. Journal of Hydraulic Engineering, 141(4), Article 04014093. https://doi.org/10.1061/(ASCE)HY.1943-7900.0000981

Project (2024). Physical hydraulic model test study report of weir

Sadiq, M., Al Rubaiee, A., & Ali, A. (2025). Numerical and physical modelling of spillway hydraulic performance. Water Science and Engineering, 18(1), 25–38. https://doi.org/10.1016/j.wse.2024.11.003

Versteeg, H. K., & Malalasekera, W. (2007). An introduction to computational fluid dynamics: The finite volume method (2nd ed.). Pearson.

Zaffar, M., Ahmad, Z., & Bakhsh, A. (2023). Downstream scour analysis of diversion barrages using different turbulence models. Journal of Hydraulic Engineering, 149(7), Article 04023034. https://doi.org/10.1061/(ASCE)HY.1943-7900.0002041

Assessment of Delay Factors and Development of a Mitigation Framework for Construction of Lift Irrigation Projects in Nepal

Prabesh Raj Baniya[1], Mahendra Raj Dhital[2]

[1]Department of Civil Engineering,
Pulchowk Campus, IOE, Lalitpur, Nepal
080mscom014.prabesh@pcampus.edu.np
[2]Construction Engineering & Management Program, Department of Civil Engineering,
Pulchowk Campus, IOE.Lalitpur, Nepal
mrdhital@ioe.edu.np

Abstract

Lift Irrigation Projects (LIPs) are important for extending year-round irrigation to Nepal's hill farmlands where gravity-fed systems are unfeasible, yet these projects face schedule overruns. This study evaluates the delay factors in LIP construction, tests the impact of lift-specific parameters on time overruns, and develops a contract-duration model alongside a targeted mitigation framework. Analyzing contract, time-extension, and progress records from 34 National Competitive Bidding LIPs from FY 2076/77 to 2081/82 procured through Integrated River Basin Irrigation and Water Resource Management Program performing under Department of Water Resource and Irrigation. Time-extension documents were analyzed and weighted into ten delay factors which confirmed Schedule failure were systemic: 91.2% of contracts overran their deadlines on an average of 2.40 times their initially contract durations. While the COVID-19 pandemic and material shortages were the most frequently cited delay causes, unresolved site and land access consumed the largest share of time (39.1% of all approved extension days) and persisted well post-pandemic. Furthermore, while contract amount (r=0.762), number of lifts (r=0.631), and command area (r=0.482) were strong predictors of time overruns, initial contract durations showed virtually no relation to project scale (r=-0.029). A duration model explained 63.1% of the variance, indicating that arbitrary standard periods severely under-provision large contracts. Consequently, the proposed mitigation framework prioritizes securing land consent prior to mobilization and scaling contract durations realistically to project size.

Keywords: Lift irrigation; Extension of time; Construction delay; Contract duration estimation

Introduction

Lift Irrigation Project (LIP), in which water is pumped to a command area in a higher elevation, is the appropriate means of irrigation for Hills and mountains (Nepal et al., 2021). The policy basis is set out in the Irrigation Master Plan 2019 (Updated 2024), which targets 74% year-round coverage in the hills and mountains with the help of lift irrigation expansion of 4,97,600 Ha by 2045 (Department of Water Resources and Irrigation, 2024). The Sixteenth Plan carries the same direction into the current planning cycle (National Planning Commission, 2024). Against this policy commitment, delivery performance is the binding constraint. A LIP is not similar to road or building project. It is a composite system combining civil works with an electro-mechanical package of pumps, motors and, for off-grid schemes, a photovoltaic array.

This study addresses that gap on four fronts. Firstly, it quantifies the frequency, magnitude and causes of delay. Secondly, project attributes relation to delay and similarly it develops a

calibrated contract-duration model using regression analysis. And lastly, it translates the findings into a mitigation framework for implementing agencies.

Literature Review

Delay is well documented across Nepal's public construction sector, with payment and budget-release delay, land acquisition and local obstruction, adverse weather and access, and contractor capacity and low bidding repeatedly identified as dominant causes (Acharya et al., 2021; Bhattarai, 2023; Giri et al., 2025; Niroula et al.,2024: Suwal & Shrestha, 2016). Manavazhi and Adhikari (2002) established material and equipment procurement delay as a measurable contributor to overrun in Nepalese highway projects, and the practice of granting extension of time, rather than applying contractual remedies, has been examined in both legal and project settings (Aryal & Dhakal, 2022). These findings sit within a wider international literature on construction delay in developing economies (Assaf & Al-Hejji, 2006; Sambasivan & Soon, 2007).

Lift Irrigation system also follows similar fate and are vulnerable to schedule overrun. Research on lift irrigation in Nepal has so far examined the technical and institutional challenges of solar lift schemes rather than the delivery performance of their contracts (Shrestha et al., 2026), while the Nepali irrigation studies that do report time and cost performance treat single large schemes (Mishra et al., 2021). However, no study was found, in Nepal or elsewhere, that reports the realized schedule performance of a population of lift irrigation contracts. No published duration model exists for lift irrigation.

Materials and Methods

Population and Sample

The population comprises Lift Irrigation Projects implemented under the Integrated River Basin Irrigation and Water Resource Management Program (IRBIWRMP) of the Department of Water Resources and Irrigation (DWRI) and procured through National Competitive Bidding under the Public Procurement Act and Regulations (Government of Nepal, 2007a, 2007b), for which contract, time-extension and project records are available. There are 34 contracts having 22 solar and 12 electric projects across 11 districts conducted from FY 2076/77 to 2081/82. Seventeen used single-envelope and 17 double-envelope procurements. Twenty-eight were complete, five ongoing and one cancelled. Command area ranged from 8.5–200 ha, lifting head from 56–823 m, and contract amount from NPR 54.4–542.7 lakh.

All data are secondary, drawn from official project records. These data included contract agreements documents, bid evaluation records, project design and estimates, time-extension entries and progress records giving the physical and financial progress reported at each extension request.

Methods

The frequency and magnitude of time extensions were analyzed with the help of descriptive statistics. Extension justifications were divided into ten delay factors and ranked by Pareto analysis. Where the time extension documents cited more than one factor, time extensions by each factors are obtained by dividing each application's approved days equally among the factors

it cites. Equal division is adopted because the records give no basis for weighting one cited reason above another within the same application.

Pearson and Spearman correlations were used to relate the magnitude of overrun to available project attributes such as contract amount, contract duration, command area, lifting head, and no. of lifts along with simple and multiple linear regression to quantify the relationships, with variance inflation factors used to diagnose collinearity among the project attributes. Model selection was carried out on leave-one-out cross-validated performance. Analyses were carried out in IBM SPSS Statistics and verified independently in spreadsheet form. A significance threshold of 5% is adopted throughout.

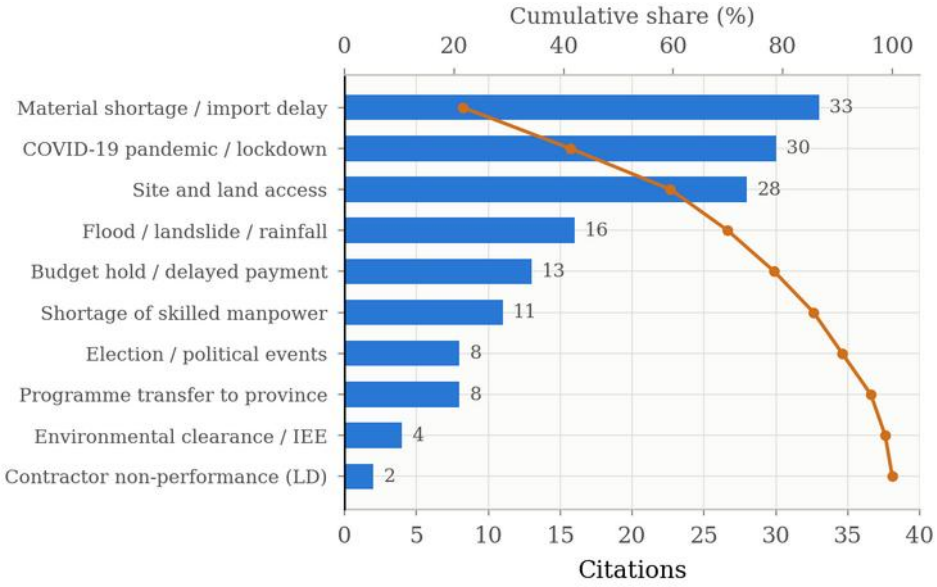
Results

Frequency And Magnitude of Schedule Overrun

Thirty-one of 34 projects (91.2%) exceeded contractual completion date. The projects recorded an average overrun of 142.2%. Mean contract duration was 321.9 days versus 774.2 actual days taken for completion which is 2.40 times the initial period. Mean overrun was about 458 days and the maximum was 1,162 days (393.9%). Median overrun ratio was 106.1%.

The 79 entries contained 153 factor citations. Material shortage/import delay and COVID-19 were most frequent (52.9% and 58.8% of projects). By approved days, site and land access was largest, accounting for 39.1% (6,180 days) of extension time from 18.3% of citations. Environmental clearance accounted for 9.3% of extension days.

Figure 1



Pareto Analysis of the Ten Delay Factors Cited in the 79 Time-Extension Entries

Table 1

Frequency and Severity of the Ten Delay Factors

Delay factor	Citations	% of sub-projects	Citations	% of extension days
Site and land access	28	18.3	6,180	39.1

Delay factor	Citations	% of sub-projects	Citations	% of extension days
Material shortage / import delay	33	21.6	2,563	16.2
COVID-19 pandemic / lockdown	30	19.6	2,541	16.1
Environmental clearance / IEE	4	2.6	1,462	9.3
Flood / landslide / rainfall	16	10.5	994	6.3
Budget hold / delayed payment	13	8.5	929	5.9
Shortage of skilled manpower	11	7.2	388	2.5
Election / political events	8	5.2	268	1.7
Program transfer to province	8	5.2	268	1.7
Contractor non-performance	2	1.3	196	1.2
Total	**153**	100	**15,788**	**100.0**

COVID-19 was a dominant citation not a sufficient explanation, contracts signed after the pandemic still averaged 163% overrun, with site access, land dispute, budget hold and environmental clearance among the cited causes.

Relation of Project Attributes and delay

amount was the strongest predictor of overrun ($r = 0.762$; $r^2 = 0.581$), with about 2.01 additional overrun days per NPR 1 lakh. Number of lifts ($r = 0.631$), command area ($r = 0.482$) and total lifting head ($r = 0.428$) were also significant. Bid discount was negatively related, while the initial allowed contract duration was not related to the time overrun at all. This runs against the Nepali low-bidding literature, which associates deeper discounts with poorer delivery (Bista & Dahal, 2018; Khanal & Dhital, 2025; Niroula & Nepal, 2024). Contracts awarded at a greater discount finished relatively closer to time, while those awarded near the estimate overran badly ($r = –0.640$). Double-envelope packages averaged 233% overrun versus 57% for single-envelope packages and 3.1 versus 1.4 extensions.

Table 2

Correlation of Project Attributes with Time Overrun (n = 34)

Attribute	r	r^2	p
Contract amount	0.762	0.581	< .001
Estimated cost	0.746	0.557	< .001
Number of lifts	0.631	0.399	< .001
Command area	0.482	0.232	.004
Total lifting head	0.428	0.184	.011
Bid discount below estimate	–0.640	0.409	< .001
Contract duration allowed	–0.206	0.043	.242

A Calibrated Contract Duration Model

Allowed duration was unrelated to contract cost ($r = –0.029$), while actual time and cost were strongly related ($r = 0.767$). Twenty-four of 34 contracts (71%) received 303 or 350 days despite wide variation in size which suggested that the contractual duration was set ad-hoc. This finding motivates a calibrated alternative. The dependent variable is total time consumed from agreement to actual completion rather than overrun, because modelling overrun would presuppose the contract period that is itself in question, and because total duration is the figure that can be written into a contract. When contract duration predictors were entered with contract amount, none remained significant at 5%. Cross validation showed cost alone performed best ($Q^2 = 0.553$), so it was selected.

Table 3

Collinearity of Project Attributes with Contract Amount (n = 34)

Attribute	r with contract amount	VIF	p alongside contract amount
Estimated cost	0.995	95.70	.312
Procurement route	0.829	3.20	.051
Number of lifts	0.866	4.01	.617
Bid discount below estimate	–0.774	2.49	.501
Total lifting head	0.635	1.68	.536
Command area	0.610	1.59	.856

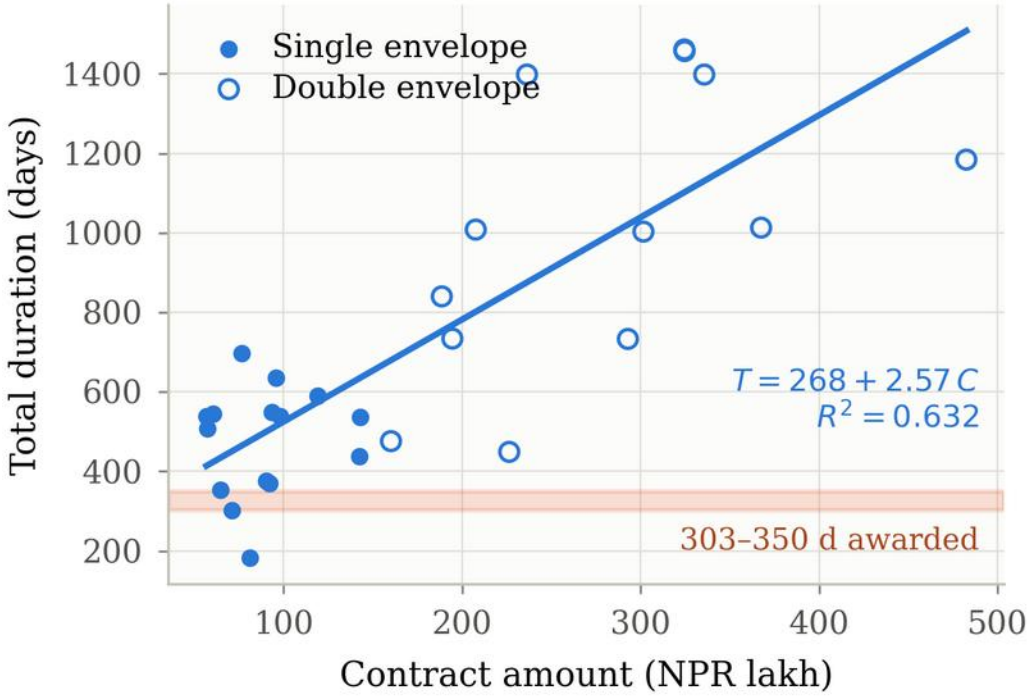
Note. VIF = variance inflation factor.

Estimated on the 28 completed contracts, the selected model relates total duration D in calendar days to contract amount A in NPR lakh:

$$D = 267.6 + 2.568\ A \quad (1)$$

The model explained 63.1% of total-duration variance (adjusted $R^2 = 0.617$, $p < .001$)

Figure 2



Fitted Duration Model Against the Periods Actually Awarded

Table 4

Model-Based Contract Duration by Contract Value

Contract amount (NPR lakh)	Predicted duration (days)	80% prediction interval (days)	Currently awarded (days)
75	460	147–774	303–350
100	525	213–836	303–350
150	653	344–963	303–350
200	782	472–1,091	303–350

Contract amount (NPR lakh)	Predicted duration (days)	80% prediction interval (days)	Currently awarded (days)
250	910	599–1,222	303–350
300	1,039	723–1,354	303–350
400	1,296	967–1,625	303–350

Discussion

Frequency and severity rank causes differently. COVID-19 and material shortages were cited most often, but site and land access consumed 39.1% of extension time. This is structural because distribution pipelines cross private holdings of the farmers served. The post-pandemic overrun and command-area relationship support the finding. The raw bid-discount association weakened after accounting for project size, while larger double-envelope packages were more complex. Most importantly, allowed duration was nearly unrelated to cost, whereas actual time increased strongly with cost.

Proposed Mitigation Framework

The mitigation framework targets the main causes and scale-related risks identified by the analysis.

1. Site and land access- Secure consent for pipeline alignments and tank/panel locations before mobilization; coordinate work with the cropping calendar; and use a time-bound grievance mechanism through water users' associations and local government. This addresses 39.1% of extension time.
2. Import-supply contingency. Include supply-risk provisions and alternative suppliers for photovoltaic modules and pump sets, with a separate lead-time schedule for electro-mechanical works.
3. Procurement risk targeting. Use stronger design review and conservative durations for double-envelope packages, which showed much higher average overrun.
4. Budget, payment and contract administration. Align budget release with the construction season, accelerate certification/payment, and apply contractual remedies alongside extensions.
5. Weather, access and clearance. Incorporate site specific flood/landslide risk assessment into design and schedule and achieve environmental and other regulatory access and clearance before execution.
6. Contract-duration estimation. Set duration from project scale using Equation 1 and Table 5 during tender preparation. Estimated cost can be used before bidding because it closely matches contract amount in the sample ($r = 0.995$).

Limitations

The study uses records from one office, so generalization to other projects should be cautious.

Contractor-attributable causes may be under-represented because contractors prepare extension applications.

The duration model uses 28 completed contracts and should be applied only within the observed cost range of NPR 57–483 lakh. Its MAPE was 33.0%, so it supports planning rather than individual completion prediction.

Conclusion

Delay in LIPs is systemic: 91.2% exceeded deadlines and the mean project required 2.40 times its initial duration. Site and land access was dominant by extension days, accounting for 6,180 of 15,788 days (39.1%), and can largely be addressed before tendering through land consent, right-of-way, siting and cropping-calendar coordination.

Contract periods were mostly standardized and unrelated to cost, whereas actual time rose strongly with cost. $D = 267.6 + 2.568A$ provides a practical basis for scale-based contract periods, confirms that LIP duration is unusually sensitive to project scale.

Future work should validate the documentary cause profile through interviews and test the models across other implementing agencies to determine whether the observed scale sensitivity is technology-specific or Program-specific.

Acknowledgments

The authors thank the Department of Water Resources and Irrigation and the Integrated River Basin Irrigation and Water Resource Management Program for access to the contract, time-extension and progress records on which this study is based, Department of Civil Engineering, Pulchowk Campus, Institute of Engineering, Tribhuvan University, Assistant Professor Mahendra Raj Dhital for supervision and guidance.

Funding

The authors received no financial support for the research, authorship, or publication of this paper.

Conflict of Interest

The authors declare no conflict of interest.

Author Contributions

Conceptualization, methodology, data curation, formal analysis, visualization and writing of the original draft: Prabesh Raj Baniya. Supervision, validation and review and editing of the manuscript: Mahendra Raj Dhital.

Data Availability

The contract, time-extension and progress records analyzed in this study are held by the Department of Water Resources and Irrigation and were accessed with departmental permission. The derived dataset of 34 contracts, the coded extension registers and the analysis workbooks supporting the results reported here are available from the corresponding author on reasonable request, subject to departmental approval.

Ethical Approval / Consent

This study analyzed secondary administrative records of construction contracts and involved approval and consent of the office form where data were taken.

References

Acharya, S., Bhandari, B. R., & Timilsina, N. (2021). Time overrun study in construction projects of rural municipalities in Syangja, Gandaki Province, Nepal. *International Journal of Engineering Research & Technology, 10*(8), 561–570.

Aryal, B., & Dhakal, B. (2022). Analysis of extension of time impact on project's performance: A case study of projects in Hupsekot Rural Municipality. *South Asian Research Journal of Engineering and Technology, 4*(5).

Assaf, S. A., & Al-Hejji, S. (2006). Causes of delay in large construction projects. *International Journal of Project Management, 24*(4), 349–357.

Bhattarai, M. (2023). Causes of delay in construction projects in Nepal. *Saudi Journal of Engineering and Technology, 8*(6), 108–114.

Bista, S. B., & Dahal, K. R. (2018). Assessment of low bidding in bridge construction with special reference to Nepal. *International Journal of Research – GRANTHAALAYAH, 6*(10), 71–80.

Department of Water Resources and Irrigation. (2024). *Irrigation master plan 2019 (updated 2024)*. Ministry of Energy, Water Resources and Irrigation, Government of Nepal.

Government of Nepal. (2007a). *Public Procurement Act, 2063 (2007)*.

Government of Nepal. (2007b). *Public Procurement Regulations, 2064 (2007), and subsequent amendments*.

Manavazhi, M. R., & Adhikari, D. K. (2002). Material and equipment procurement delays in highway projects in Nepal. *International Journal of Project Management, 20*(8), 627–632.

Mishra, A. K., Yadav, P., & Aithal, P. S. (2021). Time and cost performance status of Sikta irrigation contract. *International Journal of Management, Technology, and Social Sciences, 6*(1), 286–305. https://doi.org/10.5281/zenodo.5081379

National Planning Commission. (2024). *The Sixteenth Plan (fiscal year 2081/82–2085/86)*. Government of Nepal.

Nepal, S., Neupane, N., Belbase, D., Pandey, V. P., & Mukherji, A. (2021). Achieving water security in Nepal through unravelling the water–energy–agriculture nexus. *International Journal of Water Resources Development, 37*(1), 67–93. https://doi.org/10.1080/07900627.2019.1694867

Niroula, Y. R., & Nepal, S. (2024). Low bidding in Nepal's construction industry: Prevalence, impacts and mitigation. *PM World Journal, 13*(2).

Sambasivan, M., & Soon, Y. W. (2007). Causes and effects of delays in Malaysian construction industry. *International Journal of Project Management, 25*(5), 517–526.

Shrestha, S., Karki, D., Aryal, M., & Buchy, M. (2026). Unpacking the challenges of solar lift irrigation in Nepal's Mid-Hills: Toward a sustainable energy–water solution. *Energy for Sustainable Development, 93*, 102009.

Suwal, A., & Shrestha, S. K. (2016). Causes of delays of motorable bridge construction under postal highway projects, Department of Roads. *Journal of Advanced College of Engineering and Management, 2*, 85–94.

Impact of Global Geopolitical Conflict-Induced Fuel and Material Price Volatility on Construction Contractors in Nepal

Arun Katuwal[1], Subash Kumar Bhattarai[2]

[1]M.Sc. Construction Management, Department of Civil Engineering, Pulchowk Campus, Institute of Engineering, Tribhuvan University, Lalitpur, Nepal
080mscom005.arun@pcampus.edu.np
[2]Construction Engineering and Management Program.
Department of Civil Engineering, Pulchowk Campus, Institute of Engineering, Tribhuvan University, Lalitpur, Nepal
subashkbhattarai@gmail.com

Abstract

Geopolitical conflict and supply-chain disruption can rapidly raise fuel, material and transport costs, exposing construction contractors to financial and operational risk. This study examines these effects in Nepal and assesses existing contractual, procurement and administrative responses. A questionnaire survey of 24 contractors was triangulated with a contractor-focused in-depth interview (IDI), Nepal Oil Corporation (NOC) fuel-price records, Nepalese literature and regional policy evidence. High or very high exposure was reported by 19 respondents (79.2%) and high or very high overall impact by 18 (75.0%). Contractual/contract-administration effects had the highest mean score (4.38/5), followed by project execution and financial effects (both 4.23) and procurement (4.15). Cash-flow pressure (19/24), reduced profit margin (18/24), delivery delays (15/24) and increased working-capital needs (14/24) were the most frequent consequences. Nineteen respondents (79.2%) rated existing arrangements inadequate or very inadequate, and all supported a predefined trigger for extraordinary price increases. The proposed contractor-oriented framework combines suitable indices, an extraordinary-shock trigger, timely adjustment and payment, procurement flexibility and balanced risk sharing.

Keywords: Geopolitical conflict; Price volatility; Construction contractors; Price adjustment; procurement; Cash flow; Construction materials

Introduction

Fuel affects equipment operation, hauling and delivered-material prices. Geopolitical conflict and supply-chain disruption can therefore influence projects through supplier quotations, transport costs, material availability, working-capital needs and contract rates.

Nepal Oil Corporation (NOC) records illustrate 2026 volatility. In the Kathmandu/Pokhara/Dipayal category, diesel rose from Rs. 136/L on 15 January to Rs. 237/L on 16 April (about 74%), then fell to Rs. 195/L in July and Rs. 200/L by 17 August. Such changes affect equipment costs and the transport component of delivered materials.

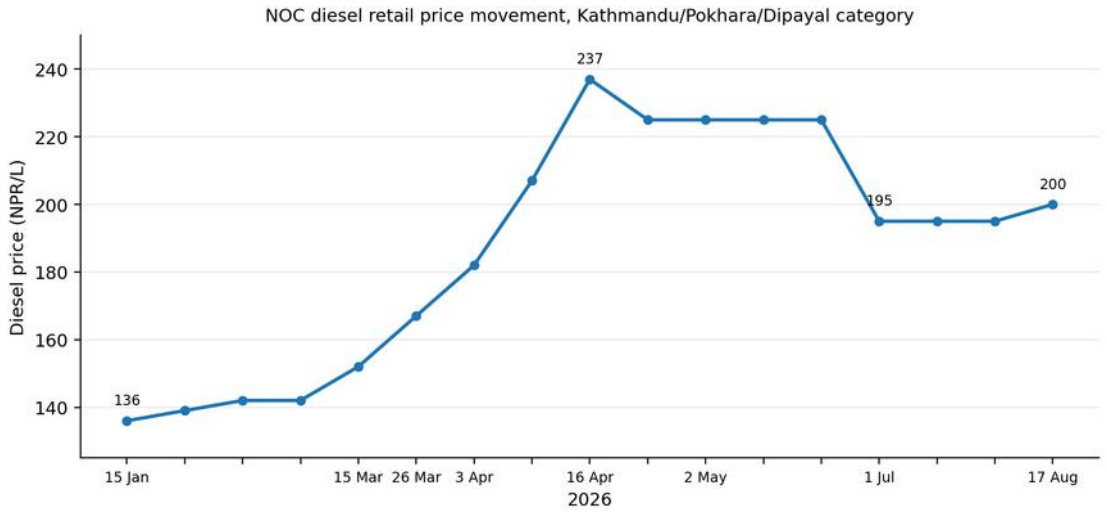


Figure 1

Official diesel price movement in the Kathmandu/Pokhara/Dipayal category, 2026. Source: Nepal Oil Corporation.

Nepalese studies report contractor-profitability risks from input-price fluctuation and incomplete adjustment coverage (Mishra & Regmi, 2017), effects on time, cost, cash flow and continuity (Chaudhary & Sharma, 2023), and claim difficulties involving indices, clauses and certification (Kayastha et al., 2024).

International evidence shows that escalation-risk allocation varies across contract systems (Chammout et al., 2024). India's 2026 highway response illustrates temporary intervention beyond normal adjustment. However, the contractor-side pathway from price shock to financial exposure, procurement disruption and contractual gaps remains underdeveloped for Nepal.

This study asks how conflict-induced fuel and material volatility affects contractors; how adequately existing adjustment, payment and procurement arrangements protect them; and which contractual, procurement and government measures could reduce residual exposure. It contributes contractor-focused evidence and a practical response framework.

Literature Review

Nepalese research links unpredictable input escalation to contractor-profit erosion and limited adjustment coverage (Mishra & Regmi, 2017), and identifies the role of adjustment in maintaining bridge-project continuity (Chaudhary & Sharma, 2023).

Kayastha et al. (2024) identify claim difficulties involving index selection, calculation and certification during time extensions. Outdated indices, uncovered inputs and delayed payment can leave residual exposure even when adjustment clauses exist. ADB (2019) likewise emphasizes appropriate indices, coefficients and covered inputs.

International evidence shows differing approaches to escalation-risk allocation (Chammout et al., 2024); India's 2026 highway measures provide a recent regional example. The literature supports clearer rules, relevant indices and balanced risk allocation, but a Nepal-specific contractor framework linking exposure, procurement, cash flow and extraordinary-shock response remains a gap.

Regional and International Approaches to Price Adjustment

In April 2026, India introduced a temporary cost-escalation compensation mechanism for National Highway projects affected by fuel, material and logistics increases. Measures included monthly payments, shorter reference lags for selected indices, revised bitumen treatment and monthly release of adjustment payments—directly relevant to survey and IDI concerns about index lag and payment delay (Government of India, Ministry of Road Transport and Highways, 2026).

In July 2026, India's Department of Expenditure encouraged Producer Price Indices (PPIs) instead of the Wholesale Price Index (WPI) in future government procurement adjustment clauses, highlighting the importance of indicators that reflect production-side costs (Government of India, Department of Expenditure, 2026).

Bangladesh's 2025 standard works tender document covers price adjustment, compensation events, delayed payment, force majeure, claims and extensions of time. Its illustrative formula includes labor, bitumen, cement, reinforcing steel, stone, bricks and fuel, with adjustable and non-adjustable components. This shows explicit contractual treatment of multiple inputs, although the document alone cannot establish project-level effectiveness (Bangladesh Public Procurement Authority, 2025).

These countries are benchmarks, not templates for direct adoption. Relevant design principles are shorter index lags, timely adjustment payments, coverage of critical inputs, explicit exceptional-event provisions and clearer extraordinary-risk allocation. These principles inform the framework alongside Nepalese literature, survey results and the IDI.

Materials and Methods

Research Design

A mixed-method contractor-focused design combined a structured questionnaire on respondent profile, exposure, affected inputs, impacts, contractual/procurement challenges, preparedness and preferred solutions with a semi-structured contractor in-depth interview (IDI) on project administration, procurement, cash flow and contract management.

Survey Sample and Data Sources

At the conference stage, 24 usable contractor responses were available. Respondents included company owners/directors/MDs, project and construction managers, site engineers, contractors/proprietors, and contract/commercial managers. Experience ranged from under three years to over ten years, with most reporting three to ten years. Respondents represented different organizational forms, contractor classes and projects across Nepal.

Table 1

Profile of the Contractor Survey Sample (n = 24)

Respondent-side role	n	%
Company Owner/Director/MD	6	25.0
Project/Construction Manager	6	25.0
Site Engineer	6	25.0
Contractor/Proprietor	3	12.5
Contract/Commercial Manager	3	12.5

Note. The conference-stage sample is purposive and is intended to provide contractor-side evidence rather than population-level estimates.

Contractor In-Depth Interview (IDI)

A purposive IDI with experienced contractor-side professionals explored price shocks, cash flow and payment, procurement constraints, adjustment claims, risk allocation and desired responses across building, road, bridge, irrigation and water-supply work. Themes were used to explain and triangulate survey findings, not pooled with survey responses.

Data Analysis

Survey data were summarized using frequencies, percentages and means for 1–5 Likert items. Four domains comprised financial (5 items), procurement (6), project execution (6) and contractual/contract-administration effects (6). Multiple-response items were reported as respondent counts. IDI themes covered escalation, project impacts, payment, procurement, claims, risk allocation, preparedness and proposed responses; these were compared with survey patterns.

Secondary Price Evidence and Triangulation

NOC retail-price records from January–August 2026 captured the sharp April movement and subsequent easing; they provide fuel context, not a proxy for all construction-input prices. Nepal Rastra Bank evidence, Nepalese literature and selected India/Bangladesh contractual and policy practices were also reviewed.

Triangulation combined (i) survey frequencies and relative problem severity, (ii) IDI explanations of cash-flow, procurement and contractual mechanisms, (iii) official market and policy records, and (iv) academic and institutional literature. Convergent evidence informed interpretation; differences were retained as limitations.

Results

Contractor Exposure and Affected Inputs

Nineteen respondents (79.2%) rated exposure to fuel/material volatility high or very high; the same number said geopolitical conflict and global supply-chain disruption contributed to instability to a large or very large extent. Supplier-quotation uncertainty averaged 4.33/5 and cost-forecasting difficulty 4.25/5, showing that effects begin before procurement.

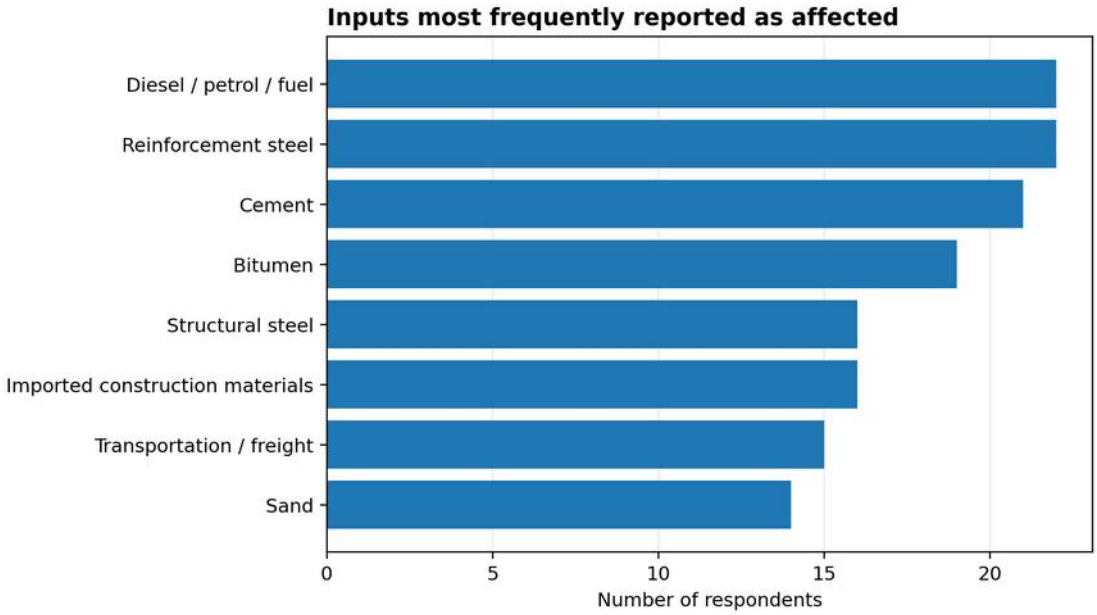


Figure 2

Construction inputs most frequently reported as significantly affected by price volatility (n = 24).

Fuel and reinforcement steel were each identified by 22 respondents, followed by cement (21), bitumen (19), structural steel and imported materials (16 each), and transport/freight (15). Price shocks are both direct and transmitted through freight and imported inputs.

Qualitative Evidence from Contractor IDI

The IDI supported the survey pattern. Sudden fuel, bitumen and steel increases were difficult under fixed unit rates because ordinary adjustment formulas may not cover extraordinary shocks. Payment delays increased reliance on working capital, borrowing and supplier advances, restricting early procurement. Short quotation validity, withdrawals, storage limits, approvals and remote-site logistics added constraints. Responses included staged/early procurement, multiple suppliers, negotiation, cash-flow planning, documentation and early notices. The interview emphasized a predefined extraordinary-shock clause, timely payments, current indices and clearer sharing of exceptional risk.

Financial, Procurement, Project and Contractual Impacts

Contractual/contract-administration effects had the highest domain mean (4.38/5), followed by project execution and financial effects (4.23 each), then procurement (4.15). Strong individual effects included maintaining planned duration and adjustment-certification delays (4.46 each), original contract rates and adjustment claims (4.42 each), and index disagreement (4.38).

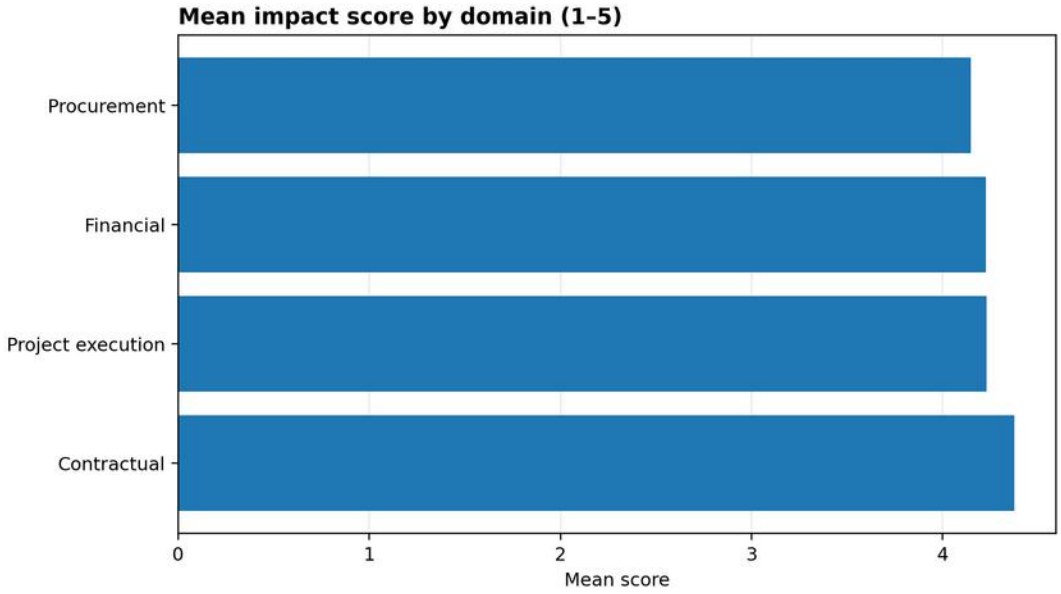


Figure 3

Mean impact score by contractor-impact domain (1 = very low, 5 = very high), n = 24.

Table 2

Mean Impact Score by Contractor-Impact Domain

Impact domain	Mean score	Interpretation
Financial	4.23	High
Procurement	4.15	High
Project execution	4.23	High
Contractual / contract administration	4.38	High

Note. Mean scores are based on 1–5 Likert-scale items, where 5 indicates very high impact.

Most Significant Consequences

Overall impact was high or very high for 18 respondents (75.0%). The most frequent consequences were cash-flow pressure (19/24), reduced profit margin (18/24), material-delivery delays (15/24), increased working-capital needs (14/24) and higher transport costs (13/24).

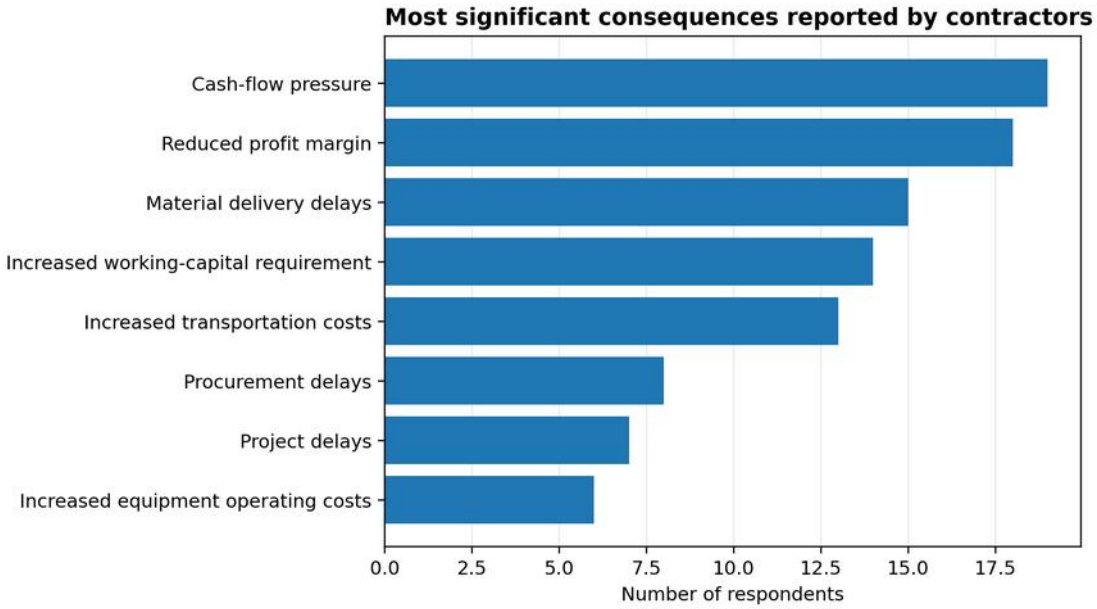


Figure 4

Most significant consequences selected by respondents (multiple responses permitted).

The findings suggest a connected chain: higher prices raise working-capital needs; delayed payments constrain early procurement; supplier uncertainty contributes to delivery delays and schedule pressure. Contractors therefore face cost, liquidity and contract-administration problems at once.

Contractual Price Adjustment and Residual Risk

Nineteen respondents (79.2%) rated existing arrangements inadequate or very inadequate; price-adjustment adequacy averaged 2.33/5. Reported problems included no adjustment provision (18/24), inappropriate/outdated indices and payment delays (16 each), uncovered materials, eligibility disagreements and insufficient coverage of actual increases (15 each).

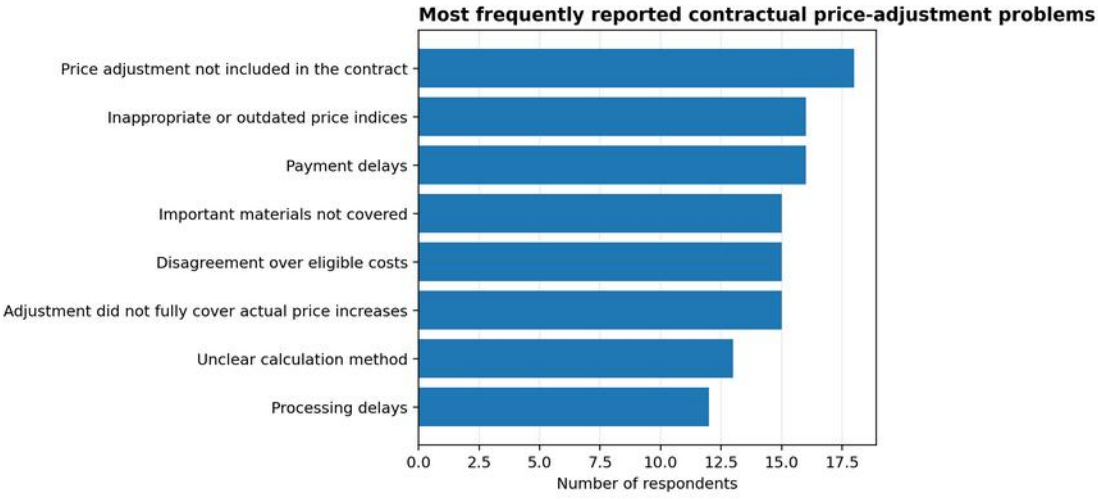


Figure 5

Most frequently reported problems with contractual price adjustment (multiple responses permitted).

Table 3

Overall Adequacy of Existing Contractual and Administrative Arrangements (n = 24)

Assessment	n	%
Very inadequate	13	54.2
Inadequate	6	25.0
Moderately adequate	3	12.5
Adequate	2	8.3

Note. The response distribution is based on the survey item assessing the overall adequacy of Nepal's existing contractual, payment and procurement system.

This indicates residual risk even where a formula exists: clauses may be absent, indices outdated, materials uncovered, eligibility disputed, processing delayed or adjustment amounts below market increases. The IDI similarly viewed formula-based adjustment as useful for gradual inflation but less effective during sudden fuel, bitumen or steel increases.

Procurement Flexibility, Payment and Preparedness

Payment delay was the main barrier to early procurement (20/24), followed by limited working capital (19), transport constraints (15), contract restrictions (13), uncertain requirements and weak market information (11 each). Responses included supplier negotiation (21), additional financing (17), early procurement (16), multiple suppliers and adjustment claims (15 each).

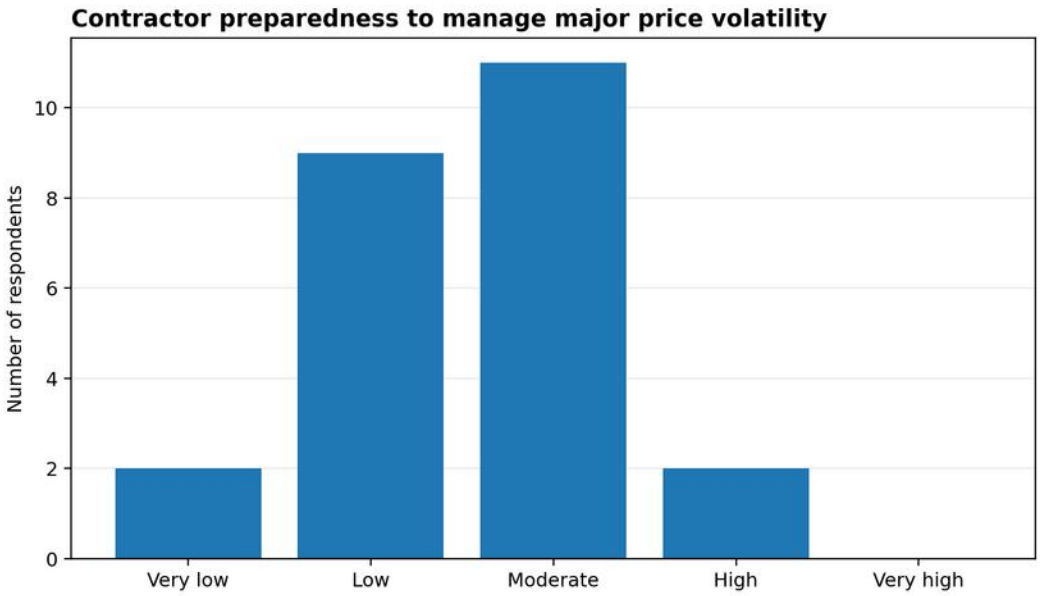


Figure 6

Contractor preparedness to manage major fuel/material price volatility (n = 24).

Twenty respondents (83.3%) rated preparedness moderate or low. Contractors were active but often relied on reactive, liquidity-intensive measures. Borrowing, early procurement and

negotiation may help but increase financing costs and inventory risk when shock timing is uncertain.

Preferred Mechanisms and Government Measures

Nine respondents preferred formula-based adjustment plus extraordinary compensation, eight preferred verified actual-cost adjustment, four preferred predefined compensation and two project-specific mechanisms. All 24 supported a predefined extraordinary-price trigger (15 ‘definitely yes’; 9 ‘probably yes’).

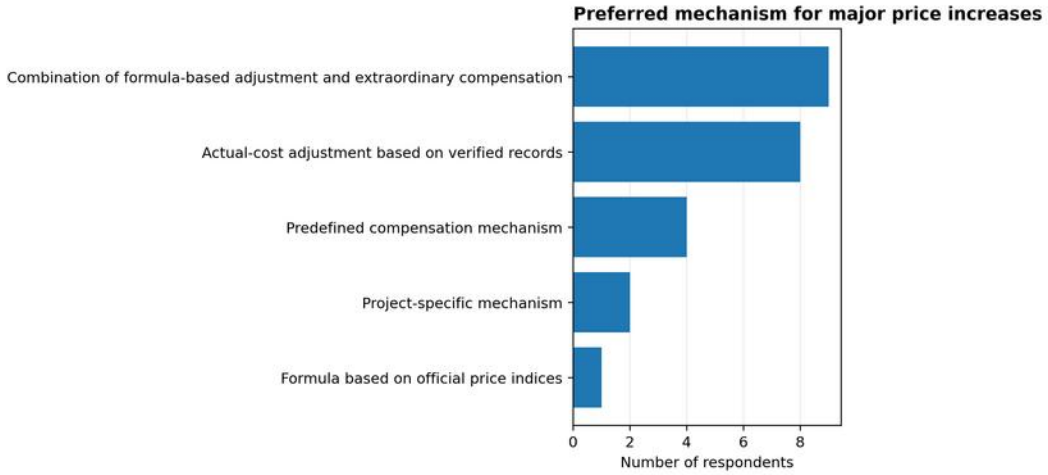


Figure 7

Preferred mechanism for addressing major fuel and material price increases (n = 24).

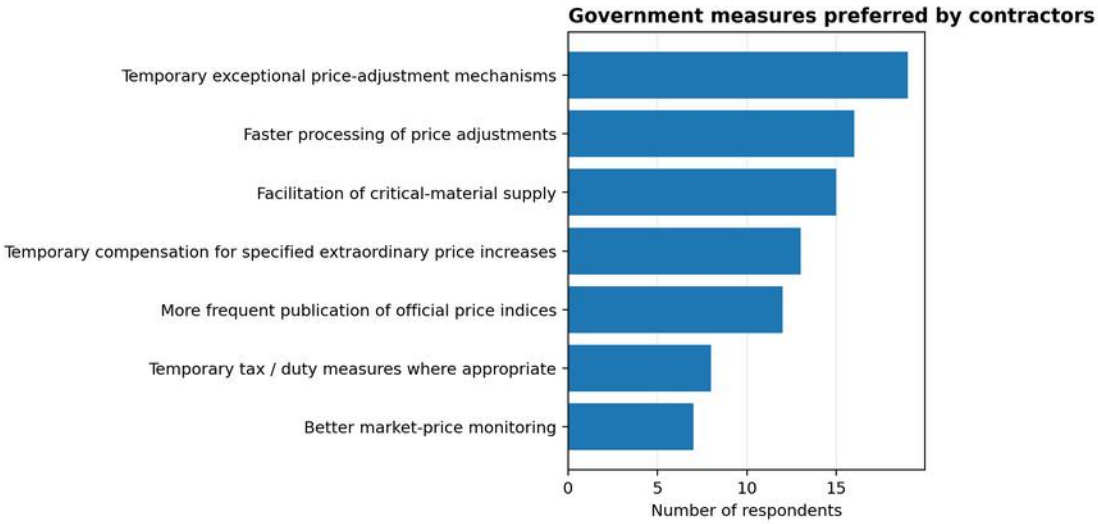


Figure 8

Government measures preferred by contractors (multiple responses permitted).

The leading government preference was temporary exceptional adjustment (19/24), followed by faster processing (16), critical-material supply facilitation (15), temporary compensation for specified extraordinary increases (13) and more frequent official indices (12). This favors a layered response rather than replacing the existing system.

Discussion

The findings indicate a pathway from external shock to quotation uncertainty, procurement/transport pressure, working-capital stress, project difficulty and contract-administration pressure. This is consistent with Nepalese research on price fluctuation and adjustment (Mishra & Regmi, 2017; Chaudhary & Sharma, 2023; Kayastha et al., 2024), while this study integrates contractor evidence across four impact domains.

The high contractual score does not imply a demand for unlimited compensation. Respondents identified specific gaps—missing clauses, outdated indices, uncovered materials, delayed payments, eligibility disputes and incomplete cost coverage—supporting clearer escalation-risk allocation (Chammout et al., 2024).

The IDI explained how sudden increases create liquidity pressure, delayed payments constrain early procurement, quotations become less reliable and ordinary formulas may miss extraordinary shocks. It is explanatory evidence, not a second quantitative sample.

Regional comparisons reinforce the importance of payment timing, index choice and exceptional-event rules. India's 2026 measures shortened selected index lags, linked adjustment to monthly payments and encouraged PPI-based clauses. Bangladesh's 2025 works document addresses adjustment, compensation events, delayed payment, force majeure and claims. These are design benchmarks, not proof of outcomes in Nepal.

Taken together, the survey, IDI, official price evidence and regional practices support a layered response: routine movement through standard adjustment and extraordinary shocks through a predefined additional mechanism. All respondents supported a definite or probable trigger, also recommended in the IDI.

Table 4

Country / source	Relevant mechanism	Relevance to Nepal findings	Implication for framework
Nepal	Formula-based price adjustment; existing contract and procurement provisions	Survey mean adequacy 2.33/5; 19/24 rated the system inadequate/very inadequate; IDI identifies index lag and incomplete shock coverage	Retain normal adjustment but add an extraordinary-shock layer
India (2026)	Temporary cost-escalation response; monthly payment; shorter index reference lag; monthly release of adjustment	Addresses payment delay, index lag and liquidity pressure identified by contractors	Use timely/current indices and faster payment/adjustment processing
India (2026)	PPI adoption encouraged for future government procurement price-adjustment clauses	Supports contractor concern about index appropriateness	Review/update indices periodically and select indices that better reflect input costs
Bangladesh (2025)	Standard works document includes price adjustment, compensation events, delayed payment, force majeure and claims; formula covers multiple	Supports broader contractual treatment of exceptional events and critical inputs	Define eligible inputs, compensation events, payment rules and risk allocation clearly

	inputs		

Proposed Mitigation Framework

The integrated evidence informs a six-element framework for public construction contracts, rather than a general economic-stabilization policy.

Table 5

Proposed Mitigation Framework for Extraordinary Price Volatility

Element	Problem identified	Proposed response
1. Monitor	Market movement can exceed estimating assumptions.	Track official indices and verified market evidence at defined intervals.
2. Trigger	Extraordinary shocks are not clearly separated from normal fluctuation.	Define an agreed threshold for extraordinary price movement.
3. Adjust	Formula may lag or omit critical inputs.	Retain normal formula-based adjustment and add an extraordinary layer above the trigger.
4. Procure	Payment, approval and storage constraints limit early procurement.	Allow justified early/bulk procurement, supplier flexibility and faster approvals.
5. Pay	Payment delays amplify liquidity exposure.	Set clear certification/payment timelines for IPCs and price adjustment.
6. Share risk	Contractor may absorb extraordinary external risk.	Allocate ordinary fluctuation within the contractor band and share extraordinary excess according to cause and magnitude.

Note. The framework triangulates survey and IDI evidence, NOC fuel prices, Nepalese literature and India/Bangladesh policy and contract documents. Regional examples inform design principles, not outcomes in Nepal. No universal trigger percentage is prescribed; contract-specific market evidence and policy review should determine it.

Limitations

The conference-stage survey includes 24 purposive responses and is not statistically representative of all Nepalese contractors. It captures professional perceptions rather than audited project accounts, which may vary by project, contract and location. The limited IDI evidence provides context, not statistical generalization.

NOC fuel prices do not represent all material prices, and the study does not estimate causal effects of specific geopolitical events on contractor outcomes. The thesis will address these limits through more survey responses, interviews and project-level evidence.

Conclusion

In this sample, 79.2% reported high/very high exposure and 75.0% high/very high overall impact. Contractual/contract-administration effects scored highest (4.38/5), and cash-flow pressure was the most frequent consequence.

Existing arrangements were rated inadequate/very inadequate by 79.2%; adjustment adequacy averaged 2.33/5. Main gaps were incomplete coverage, outdated indices, delayed processing/payment and no clear extraordinary-shock mechanism.

The framework combines routine formula-based adjustment with an extraordinary response, current price information, a predefined trigger, coverage of critical inputs, procurement flexibility, faster payment and clearer risk sharing. It integrates survey and IDI findings with Nepalese literature and India/Bangladesh benchmarks.

Acknowledgments

The author acknowledges Pulchowk Campus, Institute of Engineering, Tribhuvan University, Asst. Prof. Subash Kumar Bhattarai, and the construction professionals who contributed their time and professional experience to the study.

Funding

The author received no external financial support for this research, authorship, or publication of this paper.

Conflict of Interest

The author declares no conflict of interest.

Author Contributions

Conceptualization, methodology, data collection, analysis, visualization and writing of the original draft: Arun Katuwal. Supervision, validation and review and editing of the manuscipt: Subash Kumar Bhattarai.

Data Availability

The survey dataset is maintained by the researcher and may be made available in anonymized form subject to respondent confidentiality and institutional requirements.

Ethical Approval / Consent

Participation in the survey and interview was voluntary and based on informed consent. No confidential company or project information was required.

References

Asian Development Bank. (2019). How does ADB define price adjustment? Asian Development Bank.

Bangladesh Public Procurement Authority. (2025). Standard tender document (national) for procurement of works (e-PW3A). Government of the People’s Republic of Bangladesh. https://cptu.gov.bd/upload/standarddocument/2025-10-26-15-55-41-e-PW3A.pdf

Chammout, B., El-Adaway, I. H., Abdul Nabi, M., & Assaad, R. H. (2024). Price escalation in construction projects: Examining national and international contracts. Journal of Construction Engineering and Management, 150(9), 04024109. https://doi.org/10.1061/JCEMD4.COENG-13918

Chaudhary, N., & Sharma, M. (2023). Price adjustment practices and their impacts on bridge construction contracts. Journal of Productive Discourse, 1(1), 65–74. https://doi.org/10.36349/tjllc.2023.v01i01.008

Government of India, Department of Expenditure. (2026, July 13). Adoption of Producer Price Indices (PPIs) in place of Wholesale Price Index (WPI) in price escalation/price adjustment clauses of future Government procurement contracts (Office Memorandum No. 1/5/2026-PPD). https://doe.gov.in/en/orders-circulars/459

Government of India, Ministry of Road Transport and Highways. (2026, April 2). Government announces cost escalation compensation mechanism to mitigate impact of global scenario on National Highway projects. Press Information Bureau. https://www.pib.gov.in/PressReleasePage.aspx?PRID=2248530&lang=1&reg=3

Kayastha, R., Kisi, K., & Chitrakar, Y. (2024). Analysis of price adjustment claim during project time extension. Journal of Legal Affairs and Dispute Resolution in Engineering and Construction, 16(1), 06523003. https://doi.org/10.1061/JLADAH.LADR-1063

Mishra, A. K., & Regmi, U. (2017). Effects of price fluctuation on the financial capacity of Class A contractors. International Journal of Creative Research Thoughts, 5(4).

Monge, M., Romero Rojo, M. F., & Gil-Alana, L. A. (2023). The impact of geopolitical risk on the behavior of oil prices and freight rates. Energy, 269, 126779. https://doi.org/10.1016/j.energy.2023.126779

Nepal Oil Corporation. (2026). Retail selling price and diesel price records. https://noc.org.np/diesel

Nepal Rastra Bank. (2026). Current macroeconomic and financial situation of Nepal based on eight months data of 2025/26. https://www.nrb.org.np/contents/uploads/2026/04/Current-Macroeconomic-and-Financial-Situation-English-Based-on-Eight-Month-data-of-2025.26.pdf

Sharma, D. (2016). Adjustment of price in contracts. Federation of Contractors' Association of Nepal. https://www.nepca.org.np/wp-content/uploads/2021/01/Adjustment-of-Price-in-Contracts.pdf